UNIVERSITY OF Southampton

# Direct Numerical Simulation of turbulent flows with an impedance boundary condition

**Doctoral Thesis**

by

**Simone Olivetti**

Supervisor

Prof. **Richard D. Sandberg**

Academic year 2015/2016

## Abstract

Direct numerical simulations (DNS) of turbulent pipe flows are carried out to investigate the suppression of previously-identified internal noise sources with an acoustic liner using a time-domain acoustic liner model developed by Tam and Auriault (AIAA Journal, 34(5), 917-923, 1996). The liner model is implemented and tested in an in-house DNS code. Validation tests are conducted to show its correct implementation in the DNS solver. In order to study the liner model capability a number of tests are carried out with different liner parameters and flow Mach Numbers. To understand the effect of the liner on the acoustic and turbulent components of the unsteady wall pressure, an azimuthal/axial Fourier transform is applied and the acoustic and turbulent wavenumber regimes are clearly identified. It is found that the spectral component occupying the turbulent wavenumber range is unaffected by the liner, whereas the acoustic wavenumber components are strongly attenuated, with individual radial modes evident as each cuts on with increasing Strouhal number. The acoustic wavenumber analysis shows that the acoustic component of the wall pressure prevails over the hydrodynamic wall pressure. This allows the acoustic liner model to dissipate the acoustic field only, leaving the hydrodynamic component statistically unchanged. Furthermore, a DNS of a pipe/jet configuration is computed to study the effects of the acoustic liner model on the far-field noise. Noise prediction is performed using the Ffowcs Williams–Hawkings

**(FWH) method. The FWH method has also been tested to identify the best configuration of the FWH surface. A conical-shaped surface proved to be a better surface. Furthermore, results show far-field noise reduction when the liner model is present.**

**Acknowledgements**

Firstly, I would like to thank Prof. Richard Sandberg for offering me the opportunity to work in this PhD project and supervising my research work. I also want to thank Dr. Brian Tester for his help on the validation and analysis of the liner model performances under examination in the present work. Thanks to Dr. Gwenael Gabard and all the stuff from Aerodynamic and Flight Mechanics research group. Thanks to the University of Southampton for the financial support. I also want to thank all of my office mates for the support they have been giving me during these years of hard work.

# Contents

# List of Figures

# Nomenclature

| | |
|---|---|
| $c$ | Speed of Sound |
| $D$ | Damping Rate |
| $d$ | Specific Damping Rate |
| $E$ | Total Energy |
| $f$ | Generic Flow Variable |
| $J_m^{'}$ | Bessel Function |
| $K_m$ | Spring Rate |
| $k_m$ | Specific Spring Rate |
| $k_{x_{mn}}$ | Axial wavenumber |
| $L$ | Length |
| $M$ | Mach Number |
| $M_d$ | Fluid Mass |
| $m_d$ | Specific Fluid Mass |
| $n$ | Wall Normal |
| $P$ | Fourier transformed of pressure |
| $p$ | Pressure |
| $Pr$ | Prandtl Number |

| | |
|---|---|
| $R$ | Acoustic Resistance |
| $r$ | Radial Coordinate |
| $r_{ob}$ | Observer Distance |
| $R_{Pipe}$ | Pipe Radius |
| $Re$ | Reynolds Number |
| $S$ | Area of Surface Elements |
| $S_0$ | Cavity Neck Section |
| $St$ | Strouhal Number |
| $T$ | Temperature |
| $t$ | Time |
| $u$ | Axial Velocity Component |
| $U_0$ | Co-flow Velocity |
| $V$ | Cavity Volume |
| $v$ | Radial Velocity Component |
| $w$ | Azimuthal Velocity Component |
| $X$ | Acoustic Reactance |
| $X_1$ | Equivalent of Mass |
| $X_2$ | Equivalent Spring Constant |
| $x_i$ | Cartesian Coordinate |
| $Y^+$ | Wall Coordinate |
| $z$ | Axial Coordinate |
| $Z_a$ | Acoustic Impedance |

**Greek Symbols**

| | |
|---|---|
| $\beta_{mn}$ | Cut Off Ratio |

$\omega$ Frequency

$\rho$ Density

$\tau$ Dummy Variable

$\theta$ Azimuthal Coordinate

$\xi$ Particle Displacement

**Mathematical Symbols**

$\bar{r}$ Radial Unit Vector

$\hat{\rho}$ Fourier Transformed Density

$\hat{p}$ Fourier Transformed Pressure

$\hat{T}$ Fourier Transformed Temperature

$\hat{u}$ Fourier Transformed Axial Velocity Component

$\hat{v}$ Fourier Transformed Radial Velocity Component

$\hat{w}$ Fourier Transformed Azimuthal Velocity Component

ı Imaginary Unit $\sqrt{-1}$

$\mathbf{u}$ Velocity Field Vector

$\mathbf{x}$ Cartesian coordinates (x, y, z)

$\mathbf{y}$ Cartesian coordinates (x, y, z)

# Chapter 1

# Introduction

The noise generated by internal flows has recently received attention in the aeronautical field as well as in the industrial field. Noise generated by turbulent pipe flows represents a significant problem for industrial applications such as ventilation and piping systems. Furthermore, in the aeronautical field an aircraft's engine is an important source of noise. More specifically turbofan engines are characterized by internal turbulent flows such as by-pass duct flow and nozzle flow, through which noise internally generated by the fan, turbine or combustion propagates out to the external observer. Aircraft landing and take off are the chief sources of aviation noise. Individual aircraft have become quieter over the past 30 years, but flight frequencies have increased. As a result, aircraft noise is giving rise to increasing community concern. In particular, landing noise is increasing in importance, and has become the dominant reason for complaints in areas close to airports. In addition, those living close to very large airports may experience ground noise from sources on the airport such as taxiing aircraft, aircraft engine tests, generators or air-side vehicular traffic. Transport links to an airport, particularly

private vehicles and trains, can also make a significant contribution to noise around airports [1]. Aircraft noise can be defined as one of the most objectionable impacts of airport development. Aircraft noise can affect concentration or sleep and result in feelings of anger, frustration and powerlessness to control the noise. These factors can thus adversely affect people's quality of life. However, while many express concerns over aircraft noise, considerable uncertainties remain over the precise nature of its impacts.

Aircraft noise arises from engines and from the movement of turbulent air over the physical structure (airframe) of an aircraft. To date, noise reduction has focused mainly on reducing engine noise. In an aeronautical engine the significant noise sources originate in the fan or compressor, the turbine, and the exhaust jet [2]. In Figure 1.1 we can see that jet exhaust noise is important, especially during take-off.

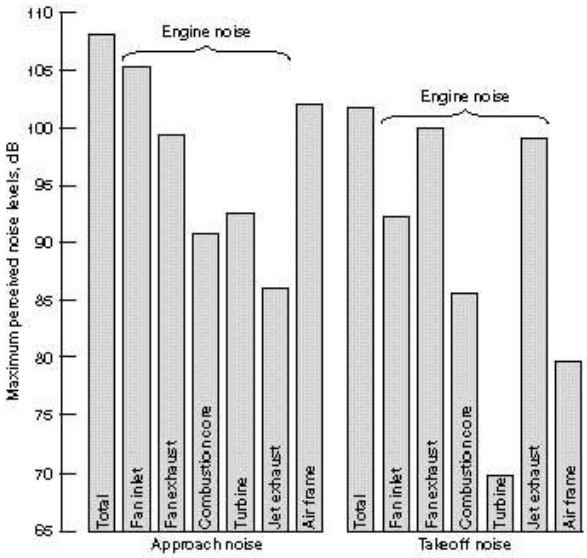


Figure 1.1: *Noise source distribution [3].*

The primary sources of jet noise for a high-speed subsonic air jet (meaning when the exhaust velocity exceeds about 100 m/s) are jet mixing noise and, for supersonic flow, shock associated noise. Also, acoustic sources within the jet pipe also contribute to the noise, mainly at lower speeds, which include combustion noise and sound produced by interactions of a turbulent stream with fans, compressors, and turbine systems [3]. Stricter noise requirements are being implemented by international noise regulatory authorities and governments.

Forty years ago, the engines were of the turbojet type where jet noise dominated. Recently, turbofans, having large bypass ratios, are commonly used in modern aircraft. Figure 1.2 shows the sources of noise and the share of each source in the total radiated noise. The engine is wrapped in a nacelle and fan noise has two paths to propagate, namely the inlet and bypass ducts. The ducts have acoustic treatment to damp and absorb noise generated by the fan. Sound that is not absorbed propagates out of the front and back of the nacelle and can be heard on the ground. In addition, liners are used inside the exhaust duct to minimize turbine and combustor noise. These tools play a fundamental role to develop a technology for jet noise reduction. Aircraft manufacturers are interested in using porous ceramic materials or metallic foams in liners to obtain better performance. This will be the main trend for future liner research [4].

Acoustic liners are a common solution to reduce the noise propagating through internal flows. Acoustic liners are passive control devices that convert sound energy into heat through viscous and thermal diffusion processes. In a turbo fan engine they are typically installed in the inlet and duct fan walls, see Figure 1.3. Liners are typically designed as porous surfaces and installed on pipe walls and internal engine ducting

walls.

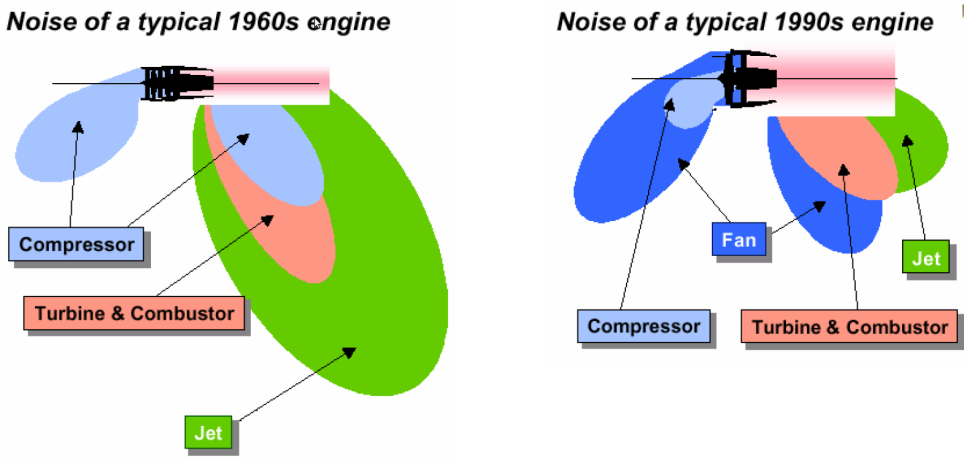


(a) Turbojet (low bypass ratio engine).

(b) Turbofan (high bypass ratio engine).

Figure 1.2: *The percentage of each noise source in different type of engines [4].*

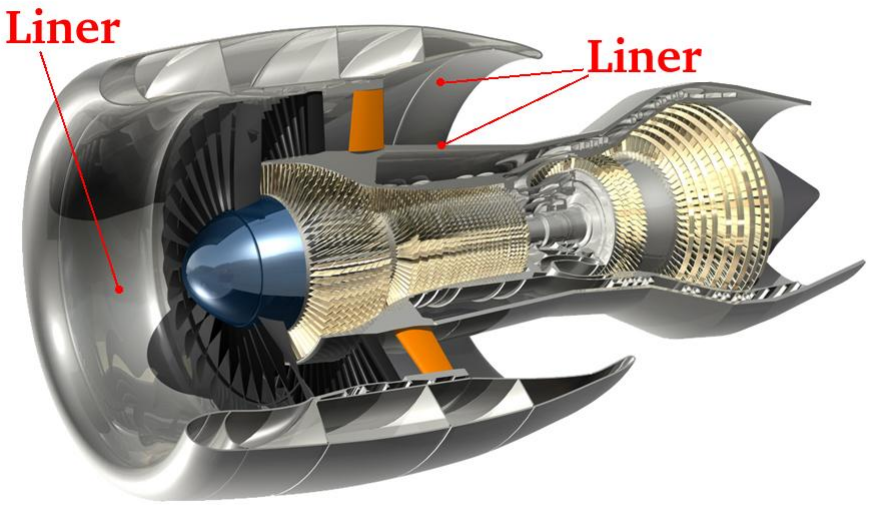


Figure 1.3: *Liners are typically installed in the inlet and duct fan walls, see red pointers.*

Acoustic liners are usually modelled as a mass-spring-damper system and are therefore characterized by a resonance frequency. Previously, researchers had developed mathematical models in order to simulate the performance of acoustic liners, see Lansing and Zorumski [6]. In classical acoustics, where typically no flow is present in the acoustic domain, liner modelling is quite simple in terms of development and numerical implementation. In contrast, when a viscous flow grazes the acoustic liner surfaces, the mathematical modelling and numerical implementation becomes far more complex, see Myers [7]. A grazing flow over an acoustic liner represents a more realistic situation in applications such as ventilation, piping and aero-engines. A number of models have been developed to approximate the steady fluid flow as being uniform, for example, Koch and Mohring [11]; Brazier-Smith and Scott [12]; or Crighton and Oswell [13]; Peake [14]; Abrahams and Wickham [15]; Lucey, Sen and Carpenter [16]. In this case, the boundary condition applied at the fluid-solid interface has to match the fluid and solid displacements. This was justified by Eversman and Beckemeyer [17] and Tester [18] by considering the limit of a vanishingly thin inviscid boundary layer at the fluid-solid interface. In this kind of modelling the boundary layer of a grazing flow over an acoustic liner is treated as an infinitely thin shear layer on the impedance surface, which is now almost universally applied under the name of the Myers boundary condition (so named because of the work of Myers [7]).

There has been considerable debate over the mathematical and numerical stability of the Myers boundary condition when applied to acoustics over reacting surfaces with slipping flow (*e.g.*, Tam and Auriault [19]; Rienstra [20]; Richter and Thiele [21]). Recently there has been growing interest in modelling a finite thickness shear layer such that a no-slip boundary condition can be applied (*e.g.* Aurgan, Starobinski and

Pagneux [22]; Vilenski and Rienstra [23]; Brambley [24]). The difficulty in developing a liner model including a viscous grazing flow might be due to lack of knowledge regarding the physical interaction between the flow field and liner cavities. In order to provide such insight, Tam et al. [25], performed a computational and experimental investigation of the acoustic properties of a three-dimensional acoustic liner with rectangular apertures. It was observed that shed vortices appear on the apertures of the cavities and tend to evolve into rings and align themselves into two regularly spaced vortex trains moving away from the resonator opening in opposite directions. More recently, Zhang and Bodony [26], demonstrated that direct numerical simulation has the potential to provide validated numerical results for acoustic liners with complex geometries. They simulated a locally-reacting honeycomb liner with circular apertures at a variety of sound pressure levels and frequencies. Although computational resources are available to accurately simulate the flow interaction with a single resonating cavity, it is still not possible to extend this analysis to a fully lined wall. Therefore, in order to investigate the effect of acoustic liners on turbulent flows, a CFD solver combined with a time-dependent impedance condition is a possible alternative. Thus, one of the main objectives of the current work is to implement the Tam & Auriault [19] liner model into an in-house viscous flow solver.

The Tam & Auriault [19] liner model incorporates a frequency independent acoustic resistance and a cavity reactance inversely proportional to frequency. Acoustic impedance conditions have previously been applied to CFD solvers, see for example Zheng & Zhuang [38] and Baelmans & Desmet [41]. However, they used artificial profiles for the boundary layer generating an artificially thickened boundary layer. As a consequence, the modelling error due to the large boundary layer thickness leads to an

incorrect prediction of the NASA flow tube experiment (Watson, Parrot & Jones [40]). Realistic boundary layers from a CFD simulation were used by Eriksson & Baralon [42]. They showed that a correct prediction of the NASA grazing flow tube experiment could be obtained by using a high-order accurate CFD code.

The aim of this study is to investigate the internal noise reduction potential of the liner model and to assess its effect on the turbulent flow. In the literature, other researchers such as Scalo *et al.* [67] have performed computational simulations for compressible turbulent channel flows with an impedance boundary condition model. They tuned the resonant frequency to the characteristic time scale of the outer layer eddies. Their studies were focused mostly on the turbulent structure alteration induced by the presence of the acoustic liner. In the present study the analysis focuses on the noise-attenuation potential of the acoustic liner model. Furthermore, in contrast to Scalo et al. [67] the present study also aims at identifying the liner parameters (*e.g.* resistance, reactance) such that the turbulent flow statistics remains unaltered.

In the present work one of the main objectives is to use an in-house DNS code to carry out an investigation on internally generated noise and its attenuation. The DNS solver has already been used by Sandberg, Sandham & Suponitsky [27] for simulations on jet noise where internally generated noise was identified. In order to study the liner model capability a number of tests are carried out with different liner parameters and flow Mach Numbers. To investigate the effect of the liner on the acoustic and turbulent components of the unsteady wall pressure, an azimuthal/axial Fourier transform is used and the acoustic and turbulent wavenumber regimes clearly identified. It was found that the Tam & Auriault formulation provide a well-posed boundary condition for the Navier-Stokes equations. The acoustic components are strongly attenuated while

the turbulent component remains statistically unchanged. These results encourage a further far field noise analysis based on jet flow simulations to evaluate the effect of the acoustic liner model on the far field noise. The relevant results related to the acoustic liner model study have been published in *Journal of Sound and Vibration*, Olivetti, Sandberg & Tester [5].

Another aim of the present work is to compute jet noise predictions with and without the presence of the acoustic liner model. The acoustic field is then analysed to identify the possible effect of the acoustic liner model. Jet flow simulations are computed using the above mentioned DNS code. The Ffowcs Williams-Hawkings (FWH) method [69] is implemented and tested to compute the jet noise prediction. The FWH method has been chosen because it allows us to reduce the computational costs for noise prediction, since it is based on a hybrid approach [82]. The FWH method has also been chosen for its capability to decompose the noise sources in terms of monopoles, dipoles and quadrupole. This could in principle provide a better understanding of the noise generation mechanisms in turbulent jet flows. However, this assumption has been proved to be wrong as the noise source decomposition in the FWH method has a physical meaning only in airframe noise analysis (*e.g.* rotor noise, gear noise). One of the objectives is to investigate the FWH noise prediction accuracy. The position and design of the FWH data surface extracted from the flow field can affect the results dramatically [82]. A number of tests are carried out to better understand the effect of FWH surface design on the noise prediction accuracy. Another objective is to compute the power spectral density (PSD) of acoustic signals in the far field using the FWH method to quantify the liner attenuation capability. Results show broadband noise reduction for certain azimuthal modes.

The summary of the main objectives is given by the followings:

- Implement the Tam & Auriault model in an in-house DNS code.
- Investigate the internally generated noise and its attenuation using an in-house DNS code.
- Use Fourier analysis to quantify the attenuation performance of acoustic liner varying crucial parameters such as Mach Number, liner resistance and reactance.
- Verify whether the presence of the liner affects the turbulent structures or not.
- Discriminate acoustic components from turbulent components of pressure in the pipe flow.
- Implement and test the Ffowcs Williams-Hawkings (FWH) method.
- Run jet flow simulations using an in-house DNS code to identify the possible effect of the acoustic liner on the far field.
- Use the Ffowcs Williams-Hawkings (FWH) method to analyse the acoustic far field.

In Chapter 2 fundamental aspects on duct acoustics and liner modelling are presented. In Chapter 3 numerical implementation and verification of the Tam & Auriault [19] are shown for different test cases. In Chapter 4 the noise reduction capability of the liner model is studied for fully turbulent pipe flow test cases. Furthermore, in Chapter 5 the FWH method is implemented and tested for jet noise prediction with and without the presence of the acoustic liner model.

# Chapter 2

# Computational aeroacoustics: noise reduction

In this chapter an introduction to computational fluid dynamics will be presented. Furthermore, the classical sound propagation formulations in cylindrical ducts will be outlined. In particular, acoustic wave propagation theory will be outlined for hard-wall and lined-wall ducts since it provides fundamental tools to validate the liner model implementation in the DNS solver. Furthermore, acoustic liner modelling will be introduced with particular emphasis on the Tam and Auriault model [19] which has been implemented in the DNS solver as shown in Chapter 3.

## 2.1 An overview

Computational fluid dynamics (CFD) has made impressive progress during the last 20 years. An obvious question may be why not use CFD methods to solve aeroacous-

tic problems?, unfortunately, aeroacoustic problems are, by nature, very different from standard aerodynamics and fluid mechanics problems. Firstly, most numerical schemes have dispersion and dissipation errors that depend on the spatial and temporal resolution and these errors are usually too large for computational aeroacoustics. Secondly, a much larger computational domain is needed for an acoustic problem than for an aerodynamic problem. This increased domain size increases computational resource requirements dramatically. For these reasons, there is a need for an independent development of computational aeroacoustics (CAA) [76][79]. The principal characteristics of aeroacoustic problems should be highlighted before developing a method; they are:

- Aeroacoustic problems typically involve a frequency range that spreads over a wide bandwidth. Numerical resolution of the high frequency waves becomes a formidable obstacle to accurate numerical simulation.

- Acoustic waves usually have small amplitudes. They are very small compared to the mean flow. To compute sound waves accurately, a numerical scheme must have extremely low numerical noise.

- In most aeroacoustic problems, interest is in the sound waves radiating to the far field. This requires a solution that is uniformly valid from the source region all the way to the measurement point many acoustic wavelengths away. Because of the long propagation distance, computational aeroacoustic schemes must have minimal numerical dispersion and dissipation. Also, it should propagate the waves at the correct wave speeds and be isotropic irrespective of the orientation of the computation mesh.

- In general, flow disturbances in aerodynamics or fluid mechanics problems tend to decay exponentially fast away from a body or their source of generation. Acoustic waves, on the other hand, decay very slowly and actually reach the boundaries of a finite computation domain. To avoid the reflection of outgoing sound waves back into the computation domain, radiation boundary conditions must be imposed at the artificial exterior boundaries to assist the waves to exit smoothly [81]. For standard computation fluid dynamics (CFD) problems, such boundary conditions are usually not required.

- Aeroacoustic problems are examples of multiple-scale problems. The length scale of the acoustic source is usually very different from the acoustic wavelength. That is, the length scale of the source region and that of the acoustic far field region can be vastly different. Computational aeroacoustics methods must be designed to deal with problems with greatly different length scales in different parts of the computational domain.

To simulate an aeroacoustic phenomenon or problem numerically, the computational algorithm must consist of three basic elements such as

- A time marching computation scheme.

- An artificial selective damping algorithm or filtering procedure.

- A set of radiation/outflow numerical treatments for use at the boundaries of the computational domain.

- A high-order discretization schemes for space and especially time due to the low acoustic amplitudes compared to the fluid flow.

A good quality time marching scheme is essential to any computation effort. Artificial selective damping or a filtering procedure is essential to eliminating spurious numerical waves that could contaminate the computed solution. Also such damping terms can often help to suppress numerical instabilities at the boundaries of the computational domain or at surfaces with discontinuities such as mesh-size-change interfaces. Numerical boundary treatments serve two basic purposes. First, they allow outgoing waves to leave the computation domain with little reflection. Second, they reproduce all the effects of the outside world on the computation domain [78][72]. For instance, if there are incoming acoustic and vorticity waves or there is an inflow, they are to be generated by the numerical boundary conditions.

## 2.2 Sound propagation in an infinite hard-wall duct

In this section an outline of the fundamental formulation for sound propagation in an infinite hard-wall duct is presented. For convenience only the most relevant equations are explained, for more details references are given through the text. Reference parameters such as density $\rho_0$, speed of sound $c_0$ and duct radius $R_{duct}$ are used to make the equations non-dimensional. Considering a uniform duct with axial uniform mean flow, the internal acoustic field can be defined with a convective non-dimensional wave equation in terms of pressure $p$,

$$\left(\frac{\partial}{\partial t} + M\frac{\partial}{\partial z}\right)^2 p - \bigtriangledown^2 p = 0, \tag{2.1}$$

where $M = U/c_0$, $U$ is the flow speed. The present formulation is defined for a uniform circular duct, therefore cylindrical coordinates are used $(z, r, \theta)$, see Figure 2.1. Since

the wall normal velocity component of the acoustic field is zero for a rigid wall [9] the boundary condition of Eq. 2.1 at $r = 1$ is

$$\frac{\partial p}{\partial r} = 0.$$

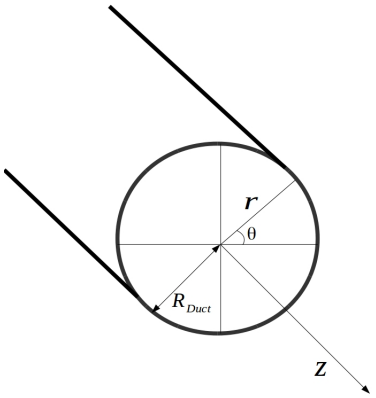


Figure 2.1: *Circlurar duct.*

Assuming that an unspecified acoustic source introduces harmonic pressure disturbances with time dependence $exp(i\omega t)$, where $\omega$ is the excitation frequency. Thus, the pressure field in the duct can be written as

$$p(z, r, \theta, t) = P(z, r, \theta) \exp(i\omega t),$$

where $P(z, r, \theta)$ satisfies the Helmholtz equation

$$(1 - M^2)\frac{\partial^2 P}{\partial z^2} + \bigtriangledown_c^2 P - 2i\omega M \frac{\partial P}{\partial z} + \omega^2 P = 0, \tag{2.2}$$

with boundary condition at $r = 1$ of

$$\frac{\partial P}{\partial r} = 0.$$

$\bigtriangledown_c$ is the gradient operator in cylindrical coordinates. Solution to Eq. 2.2 can be defined in terms of travelling waves

$$P_{mn}(z, r, \theta) = P(r) \exp(\pm im\theta) \exp(-ik_{x_{mn}} z),$$

where

$$\frac{k_{x_{mn}}}{\omega} = \frac{1}{1 - M^2} \left[ -M \pm \sqrt{1 - (1 - M^2) \left( \frac{\alpha_{mn}}{\omega} \right)^2} \right]. \tag{2.3}$$

The term $P(r)$ is then governed by the Bessel equation [9]

$$\frac{d^2P}{dt^2} + \frac{1}{r}\frac{dP}{dr} + \left( \alpha_{mn}^2 - \frac{m^2}{r^2} \right) P, \tag{2.4}$$

with boundary condition at $r = 1$ of

$$\frac{dP}{dr} = 0.$$

The solutions to Eq. 2.2 are the Bessel functions [9] of the first kind of order $m$. The eigenvalues $\alpha_{mn}$ are defined by

$$J_m^{'}(\alpha_{mn}) = 0. \tag{2.5}$$

Thus, a solution to Eq. 2.2 is

$$p_{mn}(z, r, \theta, t) = P_{mn} J_m(\alpha_{mn} r) \exp[i(\omega t \pm m\theta - k_{x_{mn}} z)]. \tag{2.6}$$

Corresponding to values of $m$ and $\alpha_{mn}$ an infinite number of solutions exist. The values of $\alpha_{mn}$ are defined by the eigenvalue equation, Eq. 2.5. Two type of modes are identified in this formulation: modes which are attenuated with distance and carry no energy defined as "cut off " while modes which propagate are defined as "cut on" [10]. A useful parameter named "cut off ratio" determines whether a mode is cut on or cut off

$$\beta_{mn} = \frac{\omega}{\alpha_{mn} \sqrt{(1 - M^2)/(\pi M)}}.$$

When $\beta_{mn} > 1$ the frequency is high enough that the mode corresponding to $\alpha_{mn}$ is cut on. In contrast, when $\beta_{mn} < 1$ modes are cut off. Since no dissipative source is present the attenuation of the cut off modes is due to the reactive nature of the acoustic field when the cut off ratio is less than unity [10].

## 2.3 Sound propagation on lined-wall ducts

The acoustic impedance of a surface is originally defined as the complex ratio of acoustic pressure and acoustic velocity at the surface for acoustic waves impinging perpendicular to the surface. This definition is extended to arbitrary angles of incidence by replacing the acoustic velocity with its component $v$ normal to the surface. In the current work, locally reacting surfaces are considered. By using the complex amplitudes of pressure $\hat{p}$ and wall-normal velocity perturbation $\hat{v}$, the complex impedance of the surface is defined as

$$Z_a(i\omega) = \frac{\hat{p}}{\hat{v}}, \tag{2.7}$$

where $\hat{v} = \hat{\mathbf{u}} \cdot \bar{r}$ is the normal component of the complex amplitude of the velocity perturbation. $Z_a$ is a complex function of the angular frequency.

When a duct is lined with sound absorbing material, the boundary condition and the corresponding eigenvalues change from those given for a hard-walled duct. It will be assumed that the lining is locally reacting and the behaviour of the material is completely determined by its normal impedance. In order to define specialized boundary condition for a lined-wall it is assumed that the particle displacement $\xi$ on

the reacting wall is directed into the wall in the inward normal direction $\bar{r}$

$$\hat{\mathbf{u}} \cdot \eta = \left( i\omega + M \frac{\partial}{\partial z} \right) \xi. \tag{2.8}$$

Considering the wall normal velocity can be defined in relation to the particle displacement $\hat{v} = i\omega\xi$ and the acoustic impedance definition 2.7 Eq. 2.8 becomes [9]

$$\frac{\partial \hat{p}}{\partial r} = -\frac{i\omega}{Z_a} \left( 1 - i \frac{M}{\omega} \frac{\partial}{\partial z} \right)^2 \hat{p}, \tag{2.9}$$

which is the boundary condition for a lined-wall case at $r = 1$. Eq. 2.9 explicitly includes the acoustic impedance $Z_a$ that characterizes the reacting surface. Solution to Eq. 2.2 together with its boundary conditions consist of an eigenvalue problem which is well known in the literature [9] [10].

### 2.3.1 Sound absorbing materials

The attenuation of sound propagating in fluids contained in ducts can be due to a variety of causes. The most significant, normally, is the volume absorption due to irreversible conversion of acoustic energy into heat in the fluid itself, through viscous and thermal diffusion processes. More prominent is the absorption at the wall. This can be due either to motion of the wall and the resulting transmission of sound through it, or to viscous and thermal diffusion processes at the wall. For relatively rigid walls of fairly high thermal conductivity, diffusion processes are more effective at the wall in producing acoustic attenuation than in the fluid itself. In general, the attenuation is dependent on frequency and on the degree of complexity of the individual amplitude patterns of

the duct modes by which the sound is being transmitted. The presence of a mean flow modifies the attenuation by convection effects and by shear layer effects. It can also change the acoustic properties of the wall. A sound absorbing material is placed along a flow passage to attenuate noise generated by some upstream device, *i.e.* a method for passive noise control. It is usually attached to a hard surface to attenuate noise by converting sound energy into heat through viscous and thermal diffusion processes. Such a device is called liner. Liner effectiveness is a function of several parameters; some have to do with the configuration of the liner itself and others with the environment in which it has to operate. The key design parameter is the acoustic impedance of acoustic liners. The efficiency of typical sound absorbing materials varies for different frequencies. For example one inch of glass fibre is quite effective at absorbing sound at high frequencies (above 2,000 Hz) but very inefficient at absorbing low frequency sound. The issue is that the absorbing material takes up a large amount of space. In many noise control applications, the noise occurs only in a narrow range of frequencies or even a single frequency. Noise generated by industrial machines/equipment mostly fall in this category. For such situations, it is possible to design a sound absorption system that is "tuned" to those targeted frequencies. By employing such a system, one can avoid the overuse of sound absorbing material and reduce the space needed to accommodate it. A typical liner structure consists of a perforated facing-sheet covering a honeycomb or porous material and has a solid back-plate. Acoustic liners are of two types, namely locally and non-locally reacting. Locally reacting liners do not allow sound propagation inside the liner, parallel to the liner surface. The facing-sheet is backed by a regular partitioned single-layer cellular structure such as metal honeycomb, as shown in Figure 2.2, with solid walls perpendicular to the face-sheet

plate. Such a design is called a single degree-of-freedom liner (SDOF). The locally reacting liner can be considered as an array of Helmholtz resonators, whose theory of operation is analogous to that of the mechanical mass-spring system. The mass of the gas oscillating in the aperture corresponds to a mechanical mass sliding over a resistive surface and the compressibility of the gas in the resonator cavity acts as the spring in the mechanical system [9].

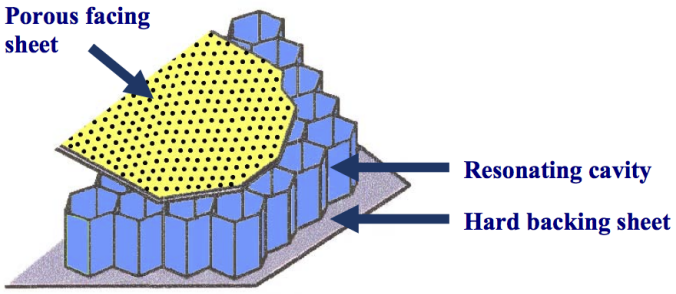


Figure 2.2: *Metal honeycomb.*

Non-locally reacting liners allow the sound waves to propagate within the liner material. They are often called bulk absorbers, with an example shown in Figure 2.3. They usually have a single-layer construction in which fibrous material fills the panel between the porous face-sheet and the back-plate. A typical example of this material is glass wool that is used, for instance, inside anechoic rooms. The SDOF liner is effective over the narrowest range of frequencies (one octave) and must be tuned to the frequency band containing the single tone of greatest concern [39]. A multiple degree-of-freedom (MDOF) liner has a wider bandwidth that can cover the main tone and its next two harmonics (about two octaves), using various internal depths and several layers with different resistance, but it is more difficult to manufacture [39].

Figure 2.3: *Bulk absorber.*

Bulk absorbers have the widest bandwidth, extending over three octaves if the panel is made sufficiently deep to be effective at the lowest frequency. However bulk absorber are less efficient at absorbing a single tone compared to MDOF or SDOF liners. The present work focuses on SDOF liners since they are commonly used in aeronautical applications such as engine noise reduction.

## 2.4 The Helmholtz resonator in frequency domain

There are many methods to realize a locally reacting surface. In the following sections, the example by a perforated face over closed cavities is considered in more detail. This concept is frequently used as basic element of the acoustic lining in duct flows. When the acoustic wave length is much longer than the size of each resonator element, a lined surface can be approximated as locally reacting. A low-frequency limit of such a resonator is found in the single degree of freedom mass-spring-damper system and is used to describe a locally-reacting surface at each wall point, see Figure 2.4. The mass-spring-damper element shown in Figure 2.4 is forced by the acoustic pressure on

its surface. The equation of motion reads

$$M_d\ddot{x} = Sp' - K_m x - D\dot{x}, \tag{2.10}$$

where $S$ denotes the area of the surface element. To obtain the impedance, the velocity of the mass element is identified with the acoustic velocity component normal to the surface. Let us multiply Eq. 2.10 by $S-1$; the mass $M_d$, spring rate $K_m$ and damping rate $D$ are replaced by the corresponding specific values $m_d$, $k_m$ and $d$, which are related to the unit area.

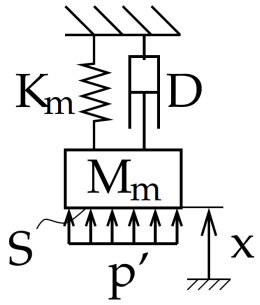


Figure 2.4: *Mass-spring-damper system.*

A complex formulation is introduced for $\hat{u}_n = u_n e^{-i\omega t}$ and $\hat{p} = pe^{-i\omega t}$ . Finally the impedance of the mass-spring-damper element shown in Figure 2.4 yields

$$Z_a(i\omega) = \frac{\hat{p}}{\hat{u}_n} = i\omega m_d + d + \frac{k_m}{i\omega} \tag{2.11}$$

The Helmholtz resonator shown in Figure 2.5 is used as a template to identify the mechanical model parameters with the constructive details of the resonator. These are the cavity volume $V$, the neck length $L$ and the open area of the neck $S_0$, as shown in Figure 2.5.

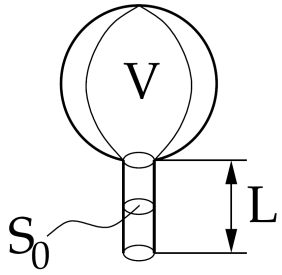


Figure 2.5: *Helmholtz resonator.*

The damping rate per unit area $d$ is only imprecisely described by theoretical predictions and needs exact measurements. Thus, the undamped Helmholtz resonator is considered first. A one-dimensional theory of the Helmholtz resonator identifies the model parameters of the mechanical system as follows

$$m_d = \rho L \text{ and } k_m = \frac{S_0 \rho c^2}{V}, \tag{2.12}$$

where $m_d$ follows from an identification of the mass element as the air in the neck of the resonator and $k_m$ is obtained by considering a quasi-static, adiabatic compression of the fluid in the cavity, due to the air pressed in from the neck. A detailed derivation can be found in Hubbard [9]. By inserting the expressions Eq. 2.12 into Eq. 2.11, one obtains the impedance of the Helmholtz resonator for low frequencies via the mechanical analogue

$$Z_{HR} = i\omega\rho L + d + \frac{S_0 \rho c^2}{V}. \tag{2.13}$$

The resonance angular frequency of the undamped Helmholtz resonator is obtained by the mechanical analogue. It reads

$$\omega = \sqrt{\frac{k_m}{m_d}} = \sqrt{\frac{S_0 c^2}{VL}}. \tag{2.14}$$

At the resonance frequency the imaginary part of the impedance, the reactance, becomes zero. By fitting the damping parameter of the mechanical analogue, the resistance can be tuned. The imaginary part of the impedance outside the resonance does not contribute to the dissipation of acoustic waves. Rather it introduces a phase shift which leads to reflections at the transition between a hard wall and the liner.

## 2.5 The Ingard/Myers boundary condition

The impedance definition of Eq. 2.7 can only find application if a layer of fluid adjacent to the impedance surface is present, which on average is not moving relative to the surface. In reality, the grazing flow along the surface is connected to this thin layer at rest by a boundary layer of finite thickness. Theoretical considerations of the duct acoustics in hard-walled ducts commonly neglect this shear layer. Assuming the continuity of the particle displacement over the infinite thin shear layer, Myers [7] formulated a new impedance boundary condition as

$$\hat{u}_n = \frac{\hat{p}(i\omega)}{Z_a(\omega)} + \underbrace{U_0 \cdot \bigtriangledown \frac{\hat{p}(i\omega)}{i\omega Z_a(i\omega)}}_{\text{convective term}} + \underbrace{\frac{\hat{p}(i\omega)}{i\omega Z_a(i\omega)} n \cdot (n \cdot \bigtriangledown U_0)}_{\text{curvature term}} . \tag{2.15}$$

The surface quantities at rest, $\hat{p}$ and $\hat{u}_n$, are related to the perturbations on the lined surface. The wall normal $n$ is defined positive when pointing into the impedance surface. The additional terms in Eq. 2.15 in comparison to Eq. 2.7 describe the convection with the mean flow and the curvature of the impedance surface. Ingard [8] formulated a similar boundary condition, which applies to plane impedance surfaces. The boundary condition of Myers [7] adds the curvature effects with respect to this

boundary condition. The two additional terms in Eq. 2.15 become zero without a mean flow ($U_0 = 0$). In this case Eq. 2.15 returns to Eq. 2.7 as the assumed thin shear layer vanishes and the field variables on both sides are equal. The boundary condition is valid only if the boundary layer thickness of the mean flow and the acoustic boundary layers are small compared to the acoustic wavelength [7].

## 2.6 Impedance boundary condition in the presence of a subsonic mean flow

In the presence of a non-zero mean-flow velocity, the impedance surface is separated from the fluid in motion by a boundary layer attached to the impedance surface. The acoustic waves pass this boundary layer twice as incoming and reflected waves. Due to the boundary layer, the angle of incidence to the impedance surface is changed. For analytical models of hard walled ducts, the boundary layer is usually neglected and the base flow is abstracted as uniform flow. However, with a finite impedance of the surface, the boundary layer becomes important, due to the modification of the angle of incidence on the impedance surface. The effective impedance of a surface under these so called grazing flow conditions is defined as the modified impedance under flow conditions $Z' = \hat{p}/\hat{u}_n$, where $\hat{p}$ and $\hat{u}_n$ are the complex amplitudes of pressure and velocity perturbations in the moving medium directly at the surface. In contrast, the impedance has been defined with the corresponding perturbation quantities in a fluid layer at rest with respect to the surface.

The practical application of the effective impedance is rejected due to this lack of

generality. Ingard [8] formulated an impedance boundary condition for grazing flow conditions, which makes use of the impedance, which can be measured without flow. The model for the infinitely thin shear layer on the impedance surface is obtained by considering a fluid particle, which moves from the moving fluid into the resting impedance surface. The displacement of such a physical particle should be continuous over the boundary layer, while the particle velocity may jump due to the infinitely thin shear layer. This consideration finally leads to a model which makes use of the standard impedance definition without flow, and includes a convective term to model the flow effects. Myers [7] extended the consideration of Ingard by including the effect of wall curvature under flow conditions in a generalized derivation of the impedance boundary condition with flow. With the availability of sufficient computer resources it has become possible to consider a resolved boundary layer at the impedance surface using a no-slip condition for the base flow. Due to the zero flow speed at the impedance surface, the original impedance definition without flow is recovered. The Myers boundary condition becomes obsolete. It is replaced by the numerical simulation of the wave propagation through the boundary layer.

## 2.7 Boundary layer at the impedance wall

The obvious method to include the flow effect on the impedance, is a resolved boundary layer with no slip condition at the impedance surface. This method has been applied for instance by Zheng and Zhuang [38] and Reymen *et al.* [41]. Both use artificial profiles for the boundary layer. While Zheng and Zhuang [38] observe a convergence of the solution towards the solution using the Ingard/Myers boundary condition with a

decreasing boundary layer thickness at the wall, Reymen *et al.* [41] use a finite-element approach with only two elements of quadratic order in the channel height to model the base flow. This leads to an artificially thickened boundary layer. As a consequence, the modelling error due to the large boundary layer thickness probably leads to an incorrect prediction of the NASA flow tube experiment [40].

However, both groups [41, 38] use artificial boundary layer profiles. Realistic boundary layers from a CFD simulation are considered by Burak *et al.* [42]. They show that a correct prediction of the NASA grazing-flow-tube experiment can be obtained by a high-order CFD code. Burak *et al.* [42] consider different CFD methods in combination with impedance boundary conditions. The results of Burak *et al.* [42], obtained by using a linearized Navier-Stokes solver together with a RANS model of the boundary-layer profile are the most promising. The publications of Zheng and Zhuang [38] and Reymen *et al.* [41] emphasize the importance of the correct boundary layer thickness for the acoustic solution with lined walls. The attenuation of acoustic waves by the liner as well as the presence of flow instabilities depends on it. However, the length scales of the boundary layer are much smaller than the acoustic scales. The resolved modelling requires an adequate grid resolution for both the acoustic scales and the boundary layer.

## 2.8 On the instability

The implementation of an impedance boundary condition which makes use of the Ingard/Myers boundary condition, seems to face a serious instability problem. Several authors, who compute an impedance boundary condition under non-zero mean flow

conditions, observe an instability in their simulations. The instability is found in both the time-domain [43, 44] and in frequency-domain [45] formulations. Other authors, including Tester [45] who first reported the problem, suggest it to be a model-inherent instability of a Kelvin–Helmholtz type. The free shear layer, which is necessary to support the Kelvin–Helmholtz instability, is found in the modelled shear layer of the Ingard/Myers boundary condition, which was described in the preceding section. The shear layer model describes a dissipative effect, which adds rotation and non-isentropic phenomena to the base flow. This is the energy source for the instability, which may grow spatially or temporally without bounds in the linear model. To further isolate the problem, it is necessary to look at the conditions under which the instability was observed:

- A non-zero mean flow is necessary for the instability to be present [20].
- Resolving the shear layer removes the instability in most cases [20, 15].
- Some of the authors report the instability only for refined meshes [22].
- If the discretization of the convective term is dissipative or implicit or a filter is applied, the instability is likely to be removed [63].

Rienstra [20] first classified the solutions in a cylindrical duct with impedance walls. Among the modes he found solutions with a large imaginary part of the radial wavenumber. These modes are described as surface waves, as there is a large decay of the mode amplitude with increasing distance from the wall. The decay is associated with the large imaginary part of the radial wavenumber found by Rienstra [20]. One of these

modes is found to be potentially unstable, depending on the impedance and flow velocity at the surface, according to Brambley and Peake [24, 14]. Without a base flow, there are only two surface waves which are considered to be of acoustic nature. The other two surface waves are classified as hydrodynamic surface waves. These waves only appear in the presence of a non-zero base flow; they vanish when the base flow velocity in the near wall region approaches to zero. One of these waves can describe a spatially growing convective instability or even a temporally growing absolute instability of Kelvin–Helmholtz type. The analysis of Rienstra [20] considers the limit for large angular frequencies in combination with an infinitely thin shear layer at the surface. For this limit, the instability is always present, independent of the actual impedance and flow conditions [20]. A refined analysis of the surface waves and the connected instability is provided in the work of Brambley [24]. They found that some of these surface waves may not be present for higher azimuthal modes $m$ and a Helmholtz number built with the outer radius of the duct in the range of $m$. Rienstra and Vilenski [23] recently also provide an extended analysis which uses a tanh-profile as template for the boundary layer. They show that the instability may be removed in the presence of a boundary layer of finite thickness.

The presence of the instability is found to depend on the momentum thickness of the boundary layer, the flow Mach number, the impedance and the excitation frequency according to the analysis of Rienstra and Vilenski [23]. The result provides an insight under which conditions for the instability become present. However, it does not remove the instability of the Myers boundary condition. Brambley [24] suggests a method to remove the instability, which is based on the idea of a finite membrane stiffness. This clearly contradicts the idea of a locally reacting surface. This leads to

an additional term, scaling with a fourth power of the wavenumber k, in the impedance model. However, this term becomes important for large k for which a finite difference approximation of the fourth derivative becomes most inaccurate. Altogether, the latest analysis shows that the instability is present under realistic flow conditions for specific choices of impedance and flow parameters.

There are only a few experiments in which an instability is found to dominate the observed sound field [46, 47]. The instability mechanism is obtained by a feedback loop through the cavity or the trailing edge of the cavity with the Kelvin–Helmholtz instability. The results of the NASA flow tube experiment indicate a strong near field around the trailing edge of the liner for 1 kHz. The Kelvin–Helmholtz instability can be regarded as a rare observation as also found by Rienstra and Vilenski [23], which has to be avoided for any production aircraft liner according to Bauer and Chapkis [57]. One possible explanation for the missing wide experimental evidence of this phenomenon is the connection of the instability to the shear layer thickness [23].

## 2.9 Acoustic impedance in the time domain

In general, a time-domain representation for a wall-impedance model in the frequency domain is obtained by an inverse Fourier transform. The inverse Fourier transform of the impedance definition in Eq. 2.7 leads to a convolution as

$$p(t) = \int_{-\infty}^{+\infty} Z(\tau)_a u_n(t-\tau)\mathrm{d}\tau = Z_a(t) * u_n(t). \tag{2.16}$$

To obtain the pressure perturbation at the wall, an integration over the time history of the normal velocity is required. A numerical integration of Eq. 2.16 is possible

according to the following formulation

$$p(t) = Z_a(t) * u_n(t) \cong \Delta t \sum_{m=0}^{n} u_n[m\Delta t] Z_a[(m-n)\Delta t]. \tag{2.17}$$

This equation requires significant computational resources, especially for aeroacoustic problems where a long time period is needed. Therefore, this method seems to be very limited due to the storage demands and the computational time needed [63]. In order to overcome this inconvenience, a time-domain impedance boundary condition based on a mass-spring-damper analogy was first considered by Özyörük and Long [44]. In this section only an outline of the Özyörük and Long formulation for a 2D case is presented. The reader is encouraged to consult the paper by Özyörük and Long [44] for more details. Özyörük and Long [44] propose to avoid the computation of the convolution integral in Eq. 2.16 involving the $z$-transform by expressing the $Z_a$ impedance as a fraction of two finite polynomials in the complex variable $z$,

$$Z_a(z) = \frac{a_0 \sum_{l=1}^{M} a_l z^{-l}}{1 - \sum_{l=1}^{M} b_k z^{-k}}. \tag{2.18}$$

The acoustic impedance $Z_a$ is assumed to be independent of the location on the surface. After the inverse $z$-transform the resulting formulation is

$$\frac{p^{i+1} - p^i}{\Delta t} + u_\infty \frac{\partial p^{i+1}}{\partial x} = -a_0 \frac{u_n^{i+1} - u_n^i}{\Delta t} + R^i, \tag{2.19}$$

where

$$R^i = -\frac{1}{\Delta t}\sum_{l=1}^{M} a_l(u_n^{i+1-l} - u_n^{i-l}) + \frac{1}{\Delta t}\sum_{k=1}^{N} b_k(u_n^{i+1-k} - u_n^{i-k}) + u_\infty \sum_{k=1}^{N} b_k \frac{\partial u_n^{i+1-k}}{\partial x}.$$

$u_\infty$ is the mean flow and the coefficients $a_l, b_k$ are available in the literature according to the liner model used. The normal momentum equation is used to estimate the normal component $u_n$. The discretized form is

$$\frac{u_n^{i+1} - u_n^i}{\Delta t} + u_\infty \frac{\partial u_n^i}{\partial x} + \frac{1}{\rho_\infty}\frac{\partial p^i}{\partial y} = 0.$$

As Özyörük and Long [44] reported, Eq. 2.19 provides an accurate prediction of liner performance also with the presence of a uniform mean flow. However the numerical implementation of this formulation appears to be laborious. A simpler impedance model in the time domain is provided by Tam and Auriault [19]. Tam and Auriault define the acoustic impedance with a formula containing three parameters

$$Z_a(\omega) = R + iX(\omega), \tag{2.20}$$

where the acoustic reactance $X$ is defined as

$$X(\omega) = X_1\omega + X_2/\omega. \tag{2.21}$$

$X_1$ and $X_2$ have arbitrary values where $X_1 > 0$ and $X_2 < 0$ and $R$ is the acoustic resistance. Typically, both the resistance and reactance of an acoustic treatment panel of

the Helmholtz resonator type are frequency dependent. However, over a low frequency range, say $1kHz - 3kHz$, the variation of the resistance is small [64]. Therefore in the Tam and Auriault formulation the acoustic resistance is frequency independent. Figure 2.6 shows an example of resistance and reactance defined in the Tam and Auriault impedance model.

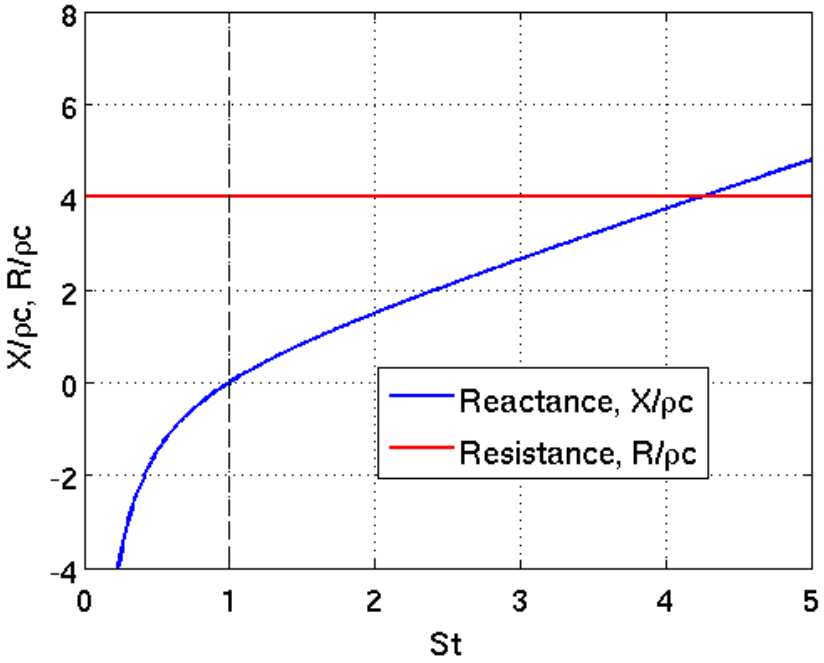


Figure 2.6: *Example of resistance and reactance in the Tam and Auriault model. Resistance is frequency independent; reactance is frequency dependent and characterized by one resonance frequency.*

The reactance is obviously frequency dependent and characterized by a resonance frequency. The resonance condition is

$$X(\omega_R) = X_1\omega_R + X_2/\omega_R = 0, \tag{2.22}$$

where $\omega_R = 2\pi St_{resonance}$. Therefore the resonance frequency is

$$St_{resonance} = \frac{1}{2\pi}\sqrt{\frac{-X_2}{X_1}}. \tag{2.23}$$

It is clear that a single $St_{resonance}$ can be given by an undefined number of $X_1$ and $X_2$ as long as they satisfy Eq. 2.22 and the conditions $X_1 > 0$, $X_2 < 0$. Now let us reformulate the impedance definition in Eq. 2.7 using Eq. 2.21

$$X(\omega) = X_1\omega + X_2/\omega = \frac{\hat{p}}{\hat{v}}. \tag{2.24}$$

Applying the inverse Fourier transform to Eq. 2.24 it is possible to obtain the time-domain impedance boundary condition proposed by Tam and Auriault

$$\frac{\partial \hat{p}}{\partial t} = R\frac{\partial \hat{v}}{\partial t} - X_2\hat{v} + X_1\frac{\partial^2 \hat{v}}{\partial t^2}. \tag{2.25}$$

It is clear that Eq. 2.25 is equivalent to a simple mass-spring-damper system, where $R$ represents the resistance, $X_2$ the spring constant and $X_1$ is the mass. Tam and Auriault [19] prove that the boundary condition 2.25 provides a well posed mathematical problem since the solution is stable and dependent continuously on the initial and boundary data. It is convenient to obtain Eq. 2.25 in terms of the wall-normal velocity component, $\hat{v}$. In order to do so the linearized energy equation in cylindrical coordinates at the wall is involved assuming no-flow in the background, hence

$$\frac{\partial \hat{p}}{\partial t} = -\left(\frac{\partial \hat{v}}{\partial r}\right)_w, \tag{2.26}$$

where $r$ is the radial coordinate. Substituting Eq. 2.26 into 2.25 we find

$$\frac{\partial^2 \hat{v}}{\partial t^2} = \frac{1}{X_1}\left[-\left(\frac{\partial \hat{v}}{\partial r}\right)_w - R\frac{\partial \hat{v}}{\partial t} + X_2 \hat{v}\right]. \tag{2.27}$$

Eq. 2.27 consists of a second order derivative of wall-normal velocity $\hat{v}$ with respect to time on the left-hand side which represents the inertial term. The first term on the right-hand side is the wall-normal derivative $(\partial \hat{v}/\partial r)_w$ which is related to the pressure time derivative according to Eq. 2.26. The second and third terms represent the damping and elastic term respectively. With $\hat{v}$ being explicit makes Eq. 2.27 particularly suitable for computational fluid dynamics solvers since the boundary conditions on the pipe wall are usually defined in terms of velocity components.

It is worth noting that Eq. 2.27 was originally defined for inviscid 1D models while in the present work Eq. 2.27 will be applied to a fully viscous 3D flow. In the original formulation by Tam and Auriault [19] the pressure time derivative was replaced by the normal gradient of the normal velocity component using the linearized energy equation. This is also possible in the current case because in viscous flow simulations a no-slip condition on the wall is applied. Therefore, only the wall-normal component, $v$, is allowed to vary, unlike the other components $u$ and $w$ which are set to zero. More details about the implementation of Tam and Auriault in a DNS code will be given in Chapter 3.

# Chapter 3

# Acoustic Liner model implementation in a direct numerical simulation code

In this chapter an outline of the DNS solver will be shown. The implementation of the Tam and Auriault model [19] in the DNS solver will be explained. A validation of the liner implementation will be conducted for a basic 1D test case, a 2D test case with and without mean flow and subsequently a 3D fully turbulent pipe test case. Furthermore, a study on the liner attenuation capability will be presented.

## 3.1 Governing Equations

The flow under consideration is governed by the full compressible Navier-Stokes equations. The fluid is assumed to be an ideal gas with constant specific heat coefficients.

All quantities are made dimensionless using the nozzle radius and the bulk velocity within the nozzle. For simplicity, all equations in this section are presented in tensor notation. The non-dimensional continuity, momentum and the energy equations are:

$$\frac{\partial \rho}{\partial t} + \frac{\partial}{\partial x_k}\left(\rho u_k\right) = 0 \ , \tag{3.1}$$

$$\frac{\partial}{\partial t}\left(\rho u_i\right) + \frac{\partial}{\partial x_k}\left[\rho u_i u_k + p\delta_{ik} - \tau_{ik}\right] = 0 \ , \tag{3.2}$$

$$\frac{\partial}{\partial t}\left(\rho E\right) + \frac{\partial}{\partial x_k}\left[\rho u_k \left(E + \frac{p}{\rho}\right) + q_k - u_i \tau_{ik}\right] = 0 \ , \tag{3.3}$$

where the total energy is defined as $E = T/\left[\gamma(\gamma-1)M^2\right] + 0.5 u_i u_i$. The stress tensor and the heat-flux vector are computed as respectively,

$$\tau_{ik} = \frac{\mu}{Re}\left(\frac{\partial u_i}{\partial x_k} + \frac{\partial u_k}{\partial x_i} - \frac{2}{3}\frac{\partial u_j}{\partial x_j}\delta_{ik}\right) \quad , \quad q_k = \frac{-\mu}{(\gamma-1)M^2 PrRe}\frac{\partial T}{\partial x_k} \ , \tag{3.4}$$

where the Prandtl number is assumed to be constant at $Pr = 0.72$, and $\gamma = 1.4$. The molecular viscosity $\mu$ is computed using Sutherland's law [28] setting the ratio of the Sutherland constant over freestream temperature to 0.36867, implying a reference temperature of 300K. To close the system of equations, the pressure is obtained from the non-dimensional equation of state $p = (\rho T)/(\gamma M^2)$.

It is important to note that the DNS solver is made non-dimensional defining the speed of sound as $c = U/M$, where $U$ is the bulk velocity at the pipe outlet and $M$ the Mach number. Furthermore, length and time is made non-dimensional using $R_{pipe}$

and $R_{pipe}/U$, respectively. This ensures the non-dimensional consistency of the DNS solver with the acoustic equations presented in Paragraph 3.3.

## 3.2 Numerical method

The compressible Navier-Stokes equations for the conservative variables are solved in cylindrical coordinates using a finite-difference/spectral DNS code. For the simulations presented here, a $4^{th}$-order standard-difference scheme with Carpenter boundary stencils [52] is applied for the spatial discretization in the radial and streamwise directions. A structured multiblock formulation is implemented in the code since the flow domain for the jet cases is divided in five blocks connected through interfaces. More details regarding the numerical set up for the jet cases will be given in Chapter 5. The pipe test cases can be considered as a subdomain case of the jet flow domain where only the pipe block is used. Details on the pipe case are given in Paragraph 3.4. The Carpenter boundary stencils [52] define the discrete spatial derivative operators with the following properties:

**First derivative properties:** Defining $f$ as a generic flow variable (*e.g.* density, velocity or temperature). The first derivative operator defining the numerical derivative $f_x = \left[(\frac{\partial f}{\partial x})_0, ..., (\frac{\partial f}{\partial x})_N\right]$ is

$$Pf_x - Qf = 0$$

$$Pfe_x - Qfe = PT_{er}, \tag{3.5}$$

where $f = [f_0(t), f_1(t), ..., f_N(t)]^T$, $fe = [fe_(x_0, t), ..., fe_(x_N, t)]^T$ and $fe_x = \left[(\frac{\partial fe}{\partial x})_0, ..., (\frac{\partial fe}{\partial x})_N\right]$. The quantity $fe$ is the exact solution. The truncation

error $T_{er}$ satisfies $|T_{er}| = O(\Delta x)$, where $\Delta x$ is the maximum distance between any two neighbouring grid points. The appropriate elements of the matrices $P$ and $Q$ for a multiblock stable formulation are provided by Carpenter [52]. The second derivative is calculated by taking the first derivative of the first derivative.

Since the test cases treated in the present work are axisymmetric flows such as pipe flows and round jets, the use of cylindrical coordinates system $(z, r, \theta)$ is particularly convenient. A cylindrical coordinates system allows an easy implementation of the Fourier spectral method for spatial discretization in the azimuthal direction. A spectral method using the FFTW3 library [49] is used in the azimuthal direction enabling an axis treatment that exploits parity conditions of individual Fourier modes [54]. The $(z, r, \theta)$ coordinate system can be mapped to curvilinear cylindrical coordinates, where only four two-dimensional metric terms are necessary rather than nine three-dimensional metric terms when performing a mapping in all coordinate directions [53]. This obviously reduces the computational costs dramatically. Spectral methods approximate the flow variables as linear combinations of global basis functions [48]. Defining $f = f(z, r, \theta, t)$ as a generic flow variable and using a Fourier-series representation as global basis functions each flow variable can be defined as

$$f(z, r, \theta, t) = \sum_{n=-N/2}^{+N/2} \hat{f}_n(z, r, t) \exp(ik_n\theta), \tag{3.6}$$

where $\hat{f}_n(z, r, t)$ are the $N_c$ expansion coefficients, $k_n = 2\pi n/\Theta$, with $\Theta$ the azimuthal resolution over which $f(z, r, \theta, t)$ is assumed to vary periodically. The most attractive advantage of the spectral methods is the high accuracy while one of the main disadvantages is the capability to handle simple geometry only [51]. However, since the current test case geometry is axisymmetric Fourier-series representation is suitable.

Time marching is achieved by an ultra low-storage five-step fourth-order Runge-Kutta scheme [55]. The compressible Navier-Stokes equations constitute a coupled set of partial differential equations that may be spatially discretized into a set of coupled ODEs with finite-difference techniques, including Carpenter boundary stencils [52]. This set of coupled ODEs can be written in the following form

$$\frac{dG}{dt} = F(t, G(t)), \qquad G(t_0) = G_0, \qquad t \in [t_0, t_N],$$

where $G = G(\rho, \rho\mathbf{u}, \rho E)$ is a function of the fluid density $\rho$, velocity vector $\mathbf{u}$ and the total energy $E$. $F$ contains the convective, inviscid, viscous and reactive terms of the compressible Navier-Stokes equations. Using the Van der Houwen and Wray scheme [55] it is possible to define two registers in order to write the following system

$$\textit{First Register} \qquad G^{j+1} = X_{rg}^{j} + (a_{j+1,j})\Delta t F^{j}, \tag{3.7}$$

$$\textit{Second Register} \qquad X_{rg}^{j+1} = G^{j+1} + (b_j - a_{j+1,j})\Delta t F^{j}, \tag{3.8}$$

$$\textit{Second Register} \qquad G^{j+2} = X_{rg}^{j+1} + (a_{j+2,j+1})\Delta t F^{j+1}, \tag{3.9}$$

$$\textit{First Register} \qquad X_{rg}^{j+2} = G^{j+2} + (b_{j+1} - a_{j+2,j+1})\Delta t F^{j+1}. \tag{3.10}$$

By overwriting, the $G, F$, and $X_{rg}$ vectors never fully coexist. The symbols $a_{ij}$ and $b_j$ are the ordinary Butcher coefficients of the scheme [50]. The vector $X_{rg}$ may be thought of as a vehicle to bring information from previous stages into the current stage. The stability of the code is enhanced by a skew-symmetric splitting of the nonlinear terms [58]. A sixth-order accurate high-wavenumber cut-off filter [59] with a weighting of 0.2 is employed after every full Runge–Kutta cycle.

## 3.3 Tam and Auriault model implementation

In this section an outline on the Tam and Auriault model [19] implementation will be presented. The Tam and Auriault model [19] is represented by a second order partial differential equation in terms of the wall normal velocity component $\hat{v}_w = \hat{v}_w(z, r, t)$. The hat symbol "ˆ" implies that the wall normal velocity component is related to the $N^{th}$ azimuthal mode. Therefore, the Tam and Auriault model [19] reads as

$$\frac{\partial^2 \hat{v}_w}{\partial t^2} = \frac{1}{X_1}\left[-\left(\frac{\partial \hat{v}_w}{\partial r}\right)_w - R\frac{\partial \hat{v}_w}{\partial t} + X_2 \hat{v}_w\right], \tag{3.11}$$

where the subscript "$w$" refers to the wall position ($r = 1$). It should be emphasized that Eq. 3.11 is applied to the pipe wall only. In other words Eq. 3.11 replaces the hard-wall condition ($v_w = 0, \forall t$) when the liner is applied. The time integration is computed by a fourth-order Runge-Kutta scheme [55] in the same way as for the Navier-Stokes equations, see Paragraph 3.2. Therefore, Eq. 3.11 needs to be reduced to a $1st$ order differential system to be compatible with the existing Ruge-Kutta scheme. In order to do so let us define the following system

$$\phi_w = \frac{\partial \hat{v}_w}{\partial t},$$

where $\phi_w$ is a dummy function, thus

$$\frac{\partial}{\partial t}\begin{bmatrix} \hat{v}_w \\ \phi_w \end{bmatrix} = \begin{bmatrix} \phi_w \\ \frac{1}{X_1}\left[-\left(\frac{\partial \hat{v}_w}{\partial r}\right)_{Wall} - R\phi_w + X_2 \hat{v}_w\right] \end{bmatrix}. \tag{3.12}$$

The wall normal derivative is computed by the Carpenter boundary stencils method [52]. Furthermore, if we define

$$\bar{\zeta} = \begin{bmatrix} \hat{v}_w \\ \phi_w \end{bmatrix}. \tag{3.13}$$

We can reduce the system to the form

$$\frac{\partial}{\partial t}\zeta = f(t,\zeta), \qquad \zeta(t_0) = 0, \qquad t \in [t_0, t_N],$$

which allows us to use the Ruge-Kutta scheme for time integration in the same way as for Navier-Stokes equations, see Paragraph 3.2. Therefore, using Van der Houwen and Wray scheme [55] it is possible to define the following numerical scheme

$$\textit{First Register} \qquad \zeta^{j+1} = \eta^j + (a_{j+1,j})\Delta t f_{RK}^j, \tag{3.14}$$

$$\textit{Second Register} \qquad \eta^{j+1} = \zeta^{j+1} + (b_j - a_{j+1,j})\Delta t f_{RK}^j, \tag{3.15}$$

$$\textit{Second Register} \qquad \zeta^{j+2} = \eta^{j+1} + (a_{j+2,j+1})\Delta t f_{RK}^{j+1}, \tag{3.16}$$

$$\textit{First Register} \qquad \eta^{j+2} = \zeta^{j+2} + (b_{j+1} - a_{j+2,j+1})\Delta t f_{RK}^{j+1}. \tag{3.17}$$

In this case $f_{RK}^j$ contains the wall normal derivative and the liner parameters $R, X_1, X_2$, $j$ is the time step index and $\Delta t$ is the time step. The vector $\eta$ is an auxiliary vector that brings information from previous stages into the current stage. The Tam and Auriault model integrated in a DNS solver can be interpreted as a coupling of two dynamic systems linked by $\left(\frac{\partial \hat{v}}{\partial r}\right)_w$ which is the time derivative of pressure distribution on the pipe wall, see Eq. 2.26. A schematic explanation of the Tam and Auriault model implementation is shown in the Figure 3.1. The DNS solver generates the flow

field parameters such as $\hat{\rho}$, $\hat{u}$, $\hat{v}$, $\hat{w}$ and temperature $\hat{T}$ at the generic time step $t_j$. Furthermore, the DNS solver produces the coupling term $\left(\frac{\partial \hat{v}}{\partial r}\right)_w$ using the Carpenter boundary stencils method [52]. The coupling term is then elaborated by the Tam and Auriault model to provide the wall normal component $\hat{v}_w$ which is fed back to the DNS solver as a boundary condition on the pipe wall. The same process is then repeated at the time step $t_{j+1}$. The pressure field is computed using the state equation of an ideal gas, $\hat{p} = \frac{\hat{\rho}\hat{T}}{\gamma M}$.

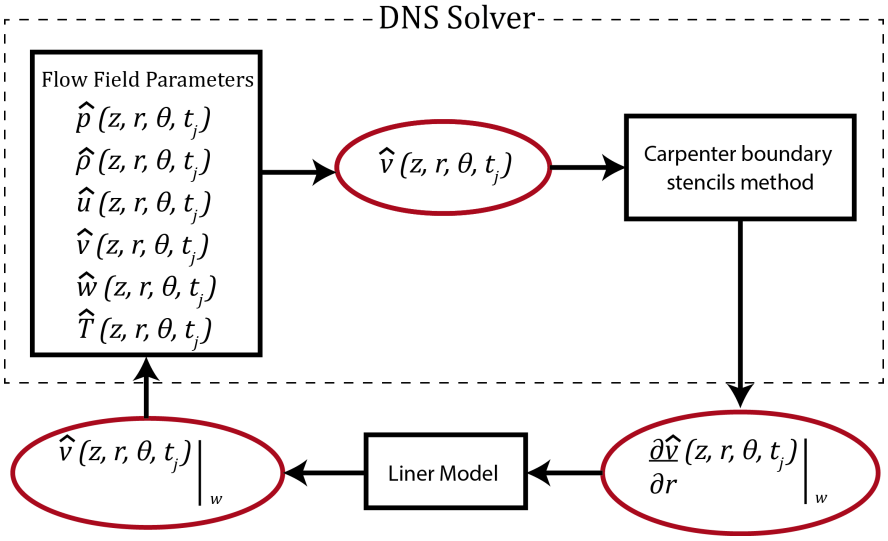


Figure 3.1: *Schematic flow chart of the Tam and Auriault model implementation; at each time step the DNS solver produces the wall normal derivative* $\left(\frac{\partial \hat{v}}{\partial r}\right)_w$ *to Tam and Auriault model which provides the DNS solver with* $\hat{v}_w$.

The other velocity components $\hat{u}$ and $\hat{w}$ are set to zero for every time step since the no-slip condition is applied as explained in Chapter 2. The Tam and Auriault model works as an acoustic energy dissipater which converts acoustic energy into heat

causing a temperature increment. However, since the acoustic energy is just a very small part of the total energy contained in the flow field the temperature increment due to the acoustic energy dissipation is negligible. Therefore, the wall temperature is set to be constant at every time step. It is important to notice that the Tam and Auriault model dissipates the acoustic energy only, leaving the turbulent kinetic energy practically untouched. This will be proved in the next sections.

## 3.4 Liner model verification

In this section results are presented for three different cases together with verification results obtained from eigenvalue solutions from the linear wave equation introduced in Paragraph 2.2. The three cases are: a) A one-dimensional (1D) model: a propagating Gaussian pulse is incident to a lined wall. The lined wall response is analysed in the time and frequency domain. b) A two-dimensional (2D) pipe model, with and without mean flow, azimuthal mode m=0, no turbulence. One or more sinusoidal signals at discrete frequencies are introduced at the in-flow, which propagate along the pipe and are attenuated by the liner. The attenuation rates are compared with the eigenvalue solutions. Note that for the verification of the liner model the acoustic pressure and the wall-normal component $v$ are made non-dimensional by $\rho_0 c_0^2$ and $c_0$, respectively.

## 3.5 Numerical set up and grid design

The computational domain comprises one block. For all cases conducted the pipe with length $L_{pipe} = 50R_{pipe}$ is discretized using 624 and 68 points in the axial and radial

directions, respectively. The grid spacing in the streamwise direction was equidistant with $\Delta z = 0.084 R_{pipe}$ up to $z = 41.5 R_{pipe}$ (3.5 radii upstream of the pipe exit) and then was refined using polynomial stretching towards the exit where $\Delta z = 0.009$. In the radial direction a polynomial stretching was used with maximum and minimum grid spacings $\Delta r = 0.026 R_{pipe}$ and $\Delta r = 0.0026 R_{pipe}$ at the axis ($r = 0$) and wall ($r = R_{pipe}$), respectively. Grid points are concentrated near the wall in an attempt to solve the turbulent structures in the vicinity of the wall. The wall-normal spacing is less than 0.6 wall units, with 14 radial points within the first $(1 - r)^+ = 10$. In the axial direction the grid was stretched, so that in the fully developed pipe region upstream of the nozzle exit, $\Delta z^+ \approx 16$, while at the nozzle exit $\Delta z^+ \approx 9$. For the three-dimensional simulations, 64 Fourier modes were used in the azimuthal direction with 100% de-aliasing, resulting in 130 collocation points in physical space. In the azimuthal direction, $r\Delta\theta \approx 10$ at upstream positions with $r\Delta\theta \approx 9$ at the pipe exit. The design of the pipe grid is based on Wu and Moin (2008) [66] where high Reynolds number turbulent pipe flows have been solved and validated using a finite different numerical scheme. In Paragraph 3.6.4 it will be shown that the resolution of this grid is fine enough to reproduce the reference data of Wu and Moin (2008) [66], therefore the pipe grid design can be considered satisfactory. Turbulent fluctuations, calculated using a digital filter technique [60] with parameters specified from periodic pipe simulations, were superposed onto the mean flow values. For the current simulations the time step is set at $\Delta t = 0.01$. Details concerning the length of the pipe needed to achieve fully developed flow and the variation of pressure, density and temperature within the pipe for various nozzle Mach numbers can be found in Sandberg *et al.* [27], where it was shown that this approach produces a fully developed turbulent pipe flow from

approximately 25-30 radii downstream of the inflow boundary. At the pipe outlet a zonal non-reflecting characteristic boundary condition is applied in order to avoid spurious acoustic reflections (Sandberg & Sandham, 2006). All the test cases have been computed using the UK National Supercomputing Service ARCHER. Table 3.1 shows the details of the parallelization of the flow domain for all the test cases.

| Direction | N. processors | N. grid points |
|---|---|---|
| $Axial, z$ | 24 | 624 |
| $Radial, r$ | 4 | 68 |
| $Azimuthal, \theta$ | 1 | 130 |

Table 3.1: *Parallelization of the 3D test cases.*

### 3.5.1 One-dimensional case

The source of sound is a Gaussian pulse normally incident on a lined wall, as shown in Figure 3.2a. The Gaussian pulse has been chosen because of its broadband frequency contents and is defined as initial condition in the DNS solver, $G(z) = A\exp(-z^2/2\sigma)$, where $A = 3.7 \times 10^{-3}$ and $\sigma = 10^{-3}$. The liner impedance is shown in Figure 3.2b, where the liner parameters, Eq. 2.22, resistance $R = 1$, $X_1 = 0.0475$ and $X_2 = -30$ have been chosen such that the liner resonates at $St = 4$. In Figure 3.3a the time-history of the lined wall response is displayed. The hard-wall reflects the Gaussian pulse perfectly, while the lined-wall reflects a wave with a different amplitude and different shape. As expected the normal velocity at the wall is no longer zero when a

liner is present. Furthermore, according to Eq. 3.12 the liner behaves as a mass-spring-damp system since the velocity returns to zero after a transient as shown in Figure 3.3a. In order to verify the liner response, the resistance and reactance of the liner are calculated using Eq. 2.7 where $\hat{p}$ and $\hat{v}$ are computed by the DNS solver. Figure 3.3b shows good agreement between the resistance and reactance from the DNS solution and the expected values. The Gaussian pulse chosen provides a frequency resolution $\Delta St = 2$. Figure 3.3b shows the same verification for a different value of $R$ and also a reactance $X$ such that the liner resonates at $St = 6$ ($X1 = 0.035$, $X2 = -30$). In these cases the agreement between the results from DNS solution and expected values of resistance and reactance is also reasonably good.

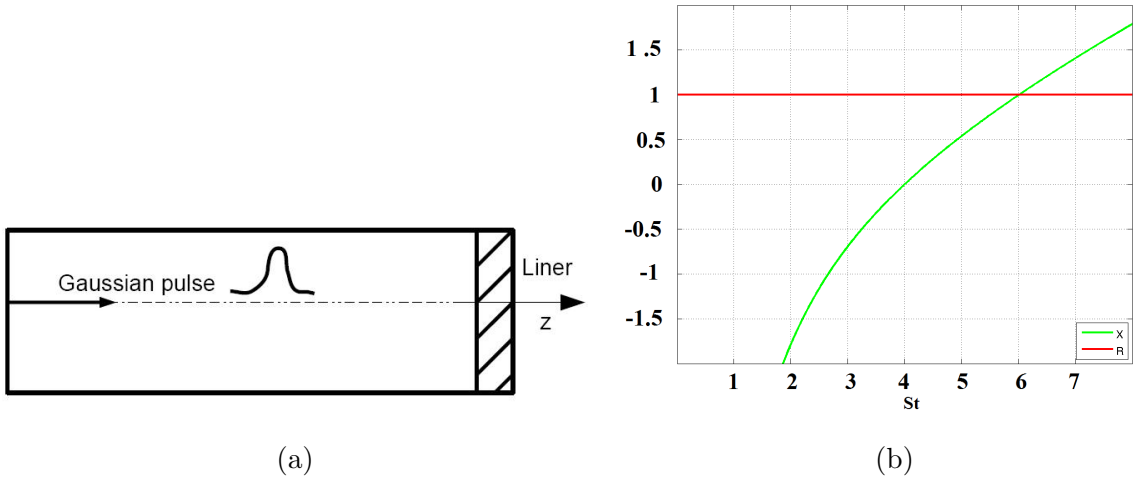


(a) (b)

Figure 3.2: *a) 1D model; the Gaussian pulse is normally incident on a lined wall. b) Resistance $R$ and reactance $X$, $St_{resonance} = 4$.*

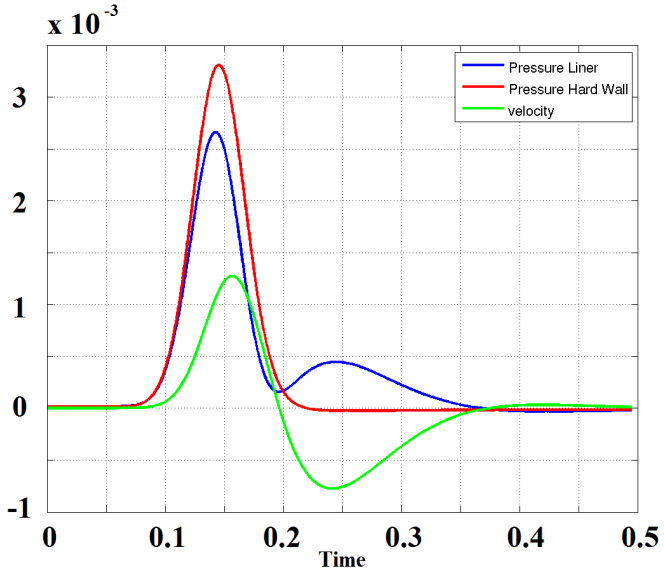


(a)

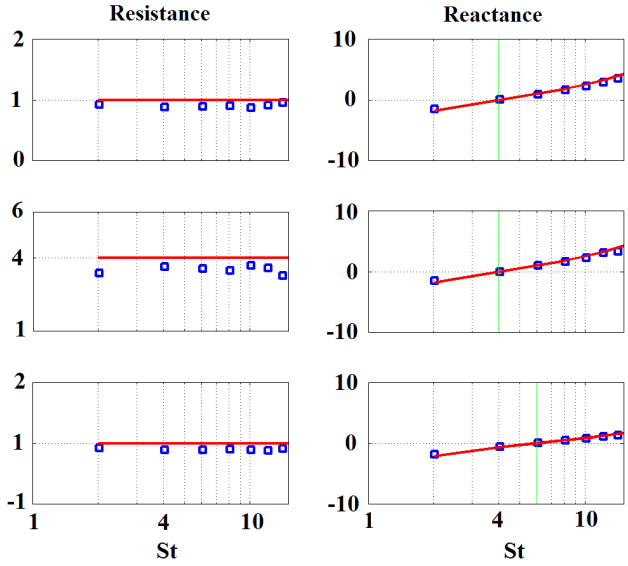


(b)

Figure 3.3: *a) Signal time-history obtained from simulations. b) Left- hand side resistance* $R = 1$ *and* 4. *Right-hand side reactance* $St_{resonance} = 4, 4$ *and* 6. *Red lines: expected value, blue squares: DNS results.*

### 3.5.2 Two-dimensional cases

In this section two-dimensional cases are validated using the model shown in Figure 3.4. The first case to be considered is a pipe with no flow ($M = 0$). The geometric computational setup is defined in Paragraph 3.2. The liner parameters are defined such that the resonance frequency is $St = 0.5$, using $X1 = 1.013$ and $X2 = -10$. Three different values for the resistance are considered, $R = 0.25$, 1 and 4.

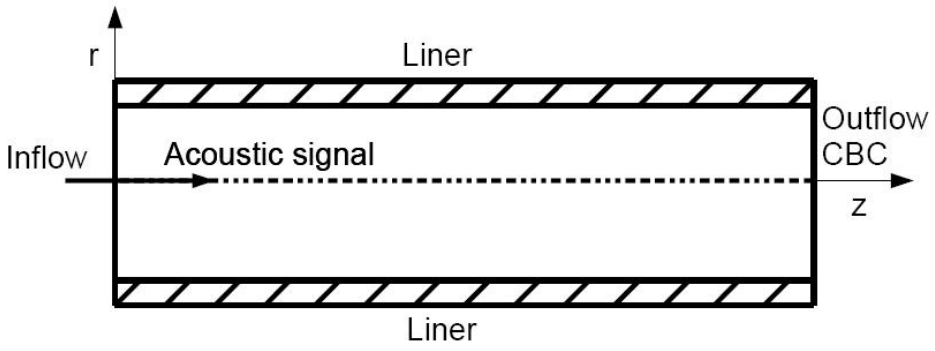


Figure 3.4: *2D model. CBC denotes a characteristic boundary condition at the outflow.*

In order to evaluate the wall attenuation along the pipe, a multi frequency sinusoidal signal is introduced at the inflow boundary of the pipe. The tone frequencies are $St = 0.5$, 1. The non-dimensional amplitude of the signal is $10^{-1}$. In Figure 3.5a the pressure spectrum is displayed at two different axial locations, $z = 2$ and $z = 15$ along the pipe wall. As expected the attenuation of the tone at $St = 0.5$ is greater than the attenuation of the tone at $St = 1$. In Figure 3.5a the multi-frequency sinusoidal tones are clearly visible. In Figure 3.5b the wall attenuation at $St = 1$ is shown and compared with the least attenuated mode predicted from a standard eigenvalue solver showing an excellent agreement for every resistance value considered.

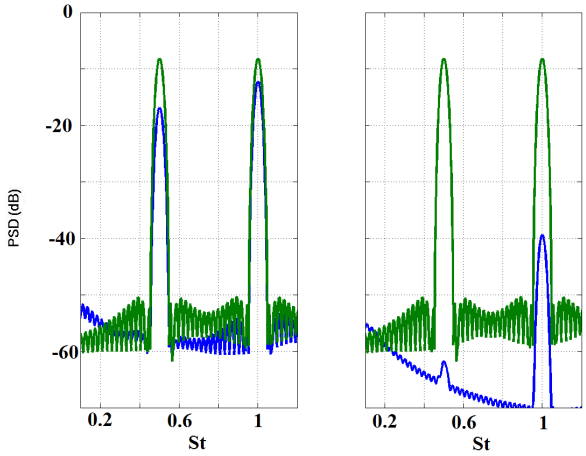


(a)

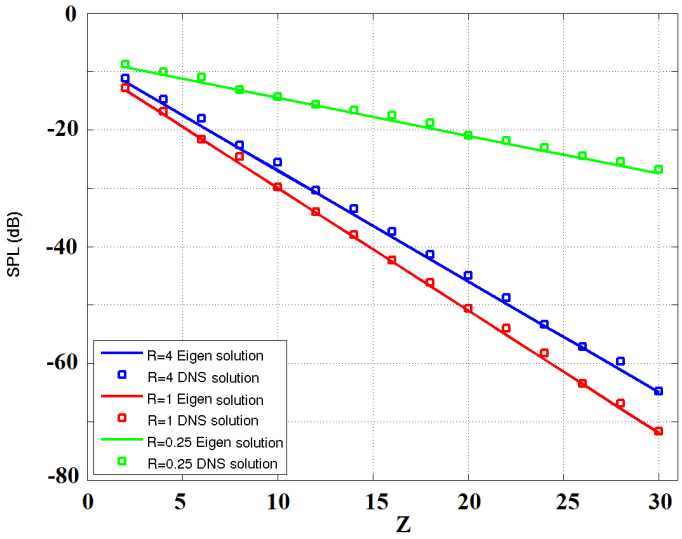


(b)

Figure 3.5: *a) Left-hand side: DNS pressure spectrum at* $z = 2$*. Right-hand side: DNS pressure spectrum at* $z = 15$*. Pressure spectrum for hard-wall case (green), pressure spectrum for lined wall case (blue),* $R = 1$*, frequency resolution* $\Delta St = 0.01$*. b) Wall attenuations in DNS compared to eigenvalue solutions.*

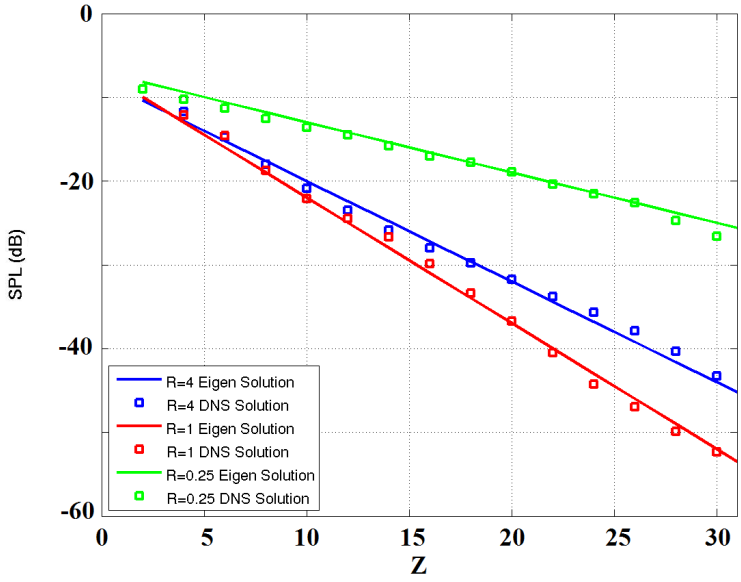


Figure 3.6: *Wall attenuations in DNS compared to eigenvalue solutions. Background flow,* $M = 0.5$.

The second 2D case is the same pipe but with a subsonic flow, $M = 0.5$. The same multi-frequency sinusoidal signal is injected into the pipe as for the zero flow case and the resistance values are also the same. The Figure 3.6 shows the DNS wall attenuation along the pipe and again these are in good agreement with the results obtained from a classic eigenvalue solution. The impedance values are predicted for three different positions along the wall, $z = 25, z = 30, z = 40$. Figure 3.7a shows the impedance prediction for $R = 1$ and $St_{resonance} = 0.5$. Figure 3.7b shows the impedance prediction for $R = 4$ and $St_{resonance} = 0.5$. Both cases are in agreement with the expected values. The case for $R = 0.25$ is not shown here, but it still gives a good agreement with the same accuracy.

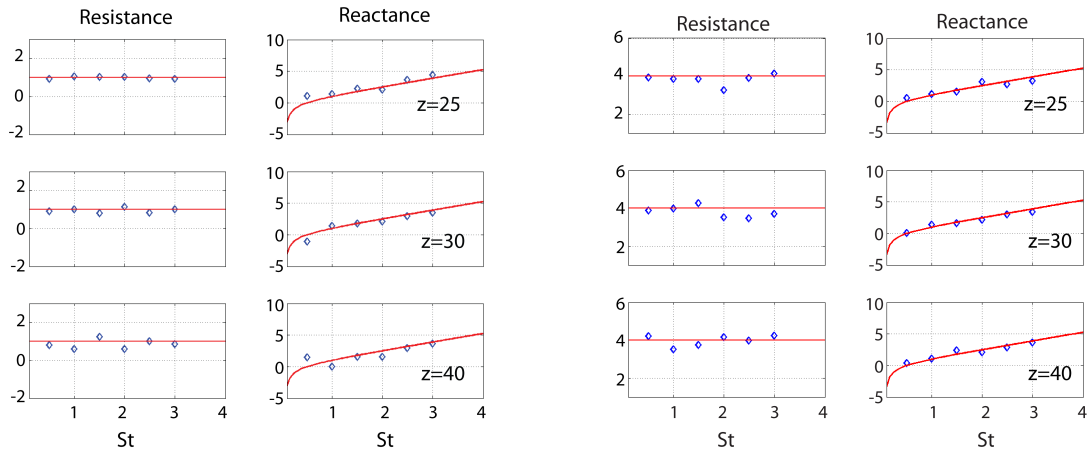


Figure 3.7: *Impedance parameter prediction for three different wall positions,* $Z = 25, Z = 30, Z = 40$. *a)* $R = 1$ *and* $St_{resonance} = 0.5$. *b)* $R = 4$ *and* $St_{resonance} = 0.5$.

### 3.5.3 Liner model testing; Turbulent pipe flow

In the 3D cases a fully turbulent pipe flow is computed using the DNS solver including a liner along the pipe wall with $M = 0.5$ and $Re = 3500$, $Re$ based on diameter. One or more sinusoidal signals at discrete frequencies are excited at the in-flow, which propagate along the pipe and are attenuated by the liner. The attenuation rates are compared with the eigenvalue solutions. Figure 3.8 shows a snapshot of the axial velocity component while Figure 3.9 shows a snapshot of the normal velocity component on the wall. As expected, with the liner present the normal velocity component is no longer zero. Figure 3.9 also shows a plane wave pattern along the pipe. This is interpreted as a plane waves generated at the inlet by a source of sound. More details about these plane waves and the effect of the liner on them will be provided later on

in this section.

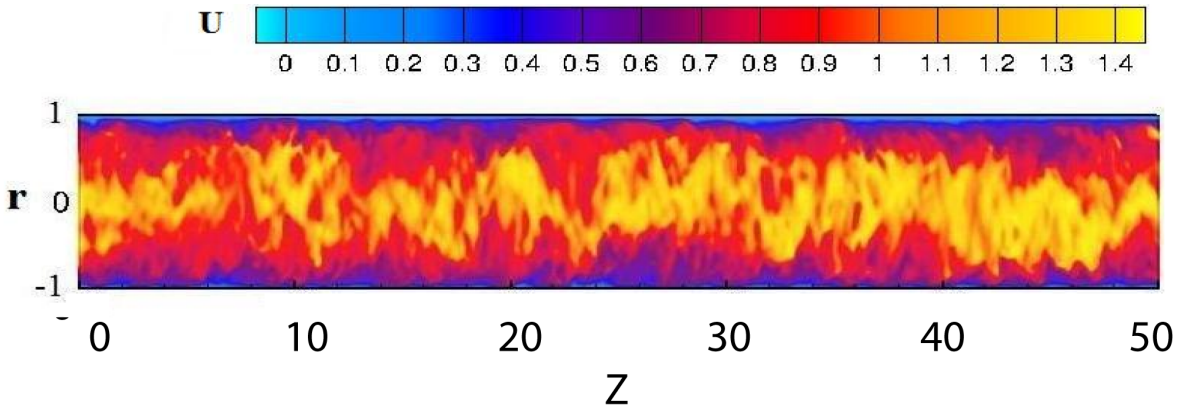


Figure 3.8: *Total axial velocity; a cut through the pipe, plane* $\theta = 0°, 180°$ *is shown.*

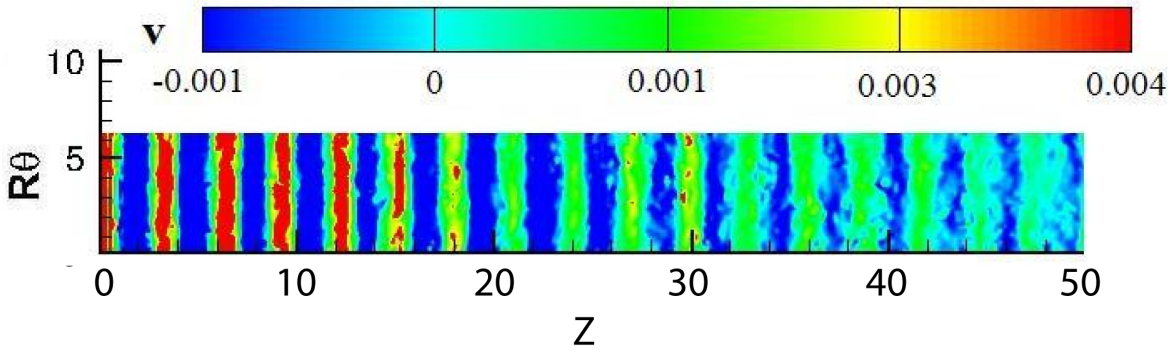


Figure 3.9: *Wall-normal velocity; v component on the wall surface.*

For the liner attenuation studies, the reactance parameters are set so that $St_{resonance} = 1$ and a sinusoidal input with a frequency of $St = 1$ is injected into the pipe.

Figure 3.10 shows the pressure spectrum at two different locations along the pipe wall. As expected the peak at $St = 1$ is significantly attenuated. Another tone appears at $St = 2$, which is a higher harmonic of the forcing frequency. The amplitude

of this tone is also considerably decreased. A reduction of the broad band signal of the turbulent flow is also observed around $St = 1$, and the bandwidth attenuation increases downstream. It should be noted that in the post-processing the mean value of the pressure has been removed from the pressure field. As in the previous cases the wall attenuation along the pipe is computed for different resistance values. The DNS acoustic resistance also shows a good agreement with the expected resistance values, see Figure 3.11b. Figure 3.11a shows a good agreement between the DNS results and the eigenvalue solution predictions.

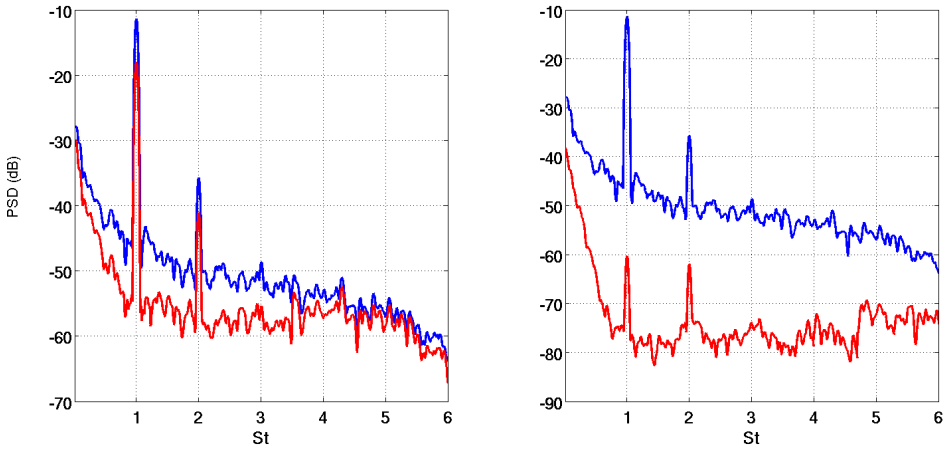


Figure 3.10: *Left-hand side: DNS pressure spectrum at* $z = 2$. *Right-hand side: DNS pressure spectrum at* $z = 12$, *hard-wall case (blue), lined wall case (red),* $R = 1$.

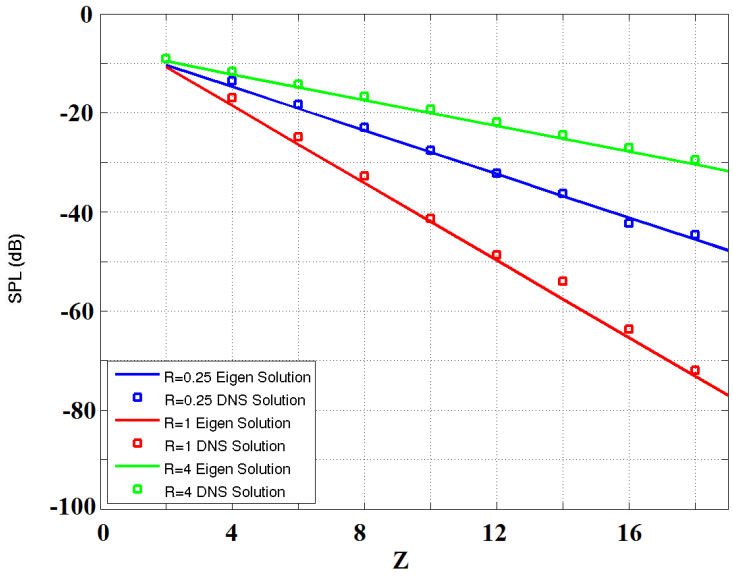


(a)

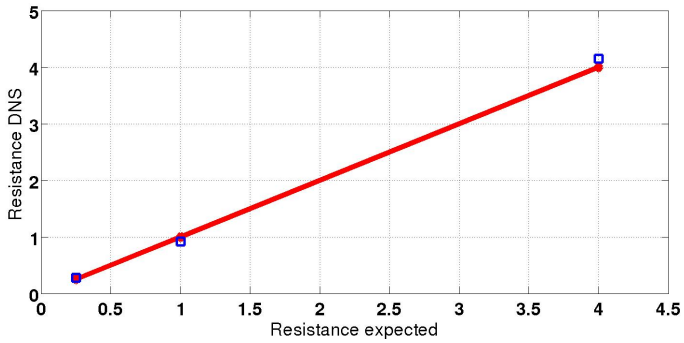


(b)

Figure 3.11: *a) Wall attenuations in DNS compared to eigenvalue solutions. Background flow, $M = 0.5$, $Re = 3500$. b) Resistance prediction; red expected values, squares DNS results.*

In order to assess the effect of a liner on the acoustic pressure field generated by the turbulence within the pipe, contours of the pressure magnitude on the pipe wall

are shown for three different Strouhal numbers, $St = 0.5$, 1 and 1.5, in Figures 3.12-3.14. In this case no sinusoidal signal is injected into the pipe and the liner is set to resonate at $St = 1$. Figure 3.12 (top) shows the contours of the pressure magnitude of wall pressure at $St = 0.5$, which is interpreted as a plane wave caused by a reflection from the end of the pipe, which is generated by the characteristic boundary condition at the pipe outlet. Figure 3.12 (bottom) displays the same contours of the pressure magnitude of wall pressure when a liner with resistance $R = 1$ is present. Figures 3.13 and 3.14 show a comparison between the hard wall case and the lined case at $St = 1$ and $St = 1.5$ respectively. As expected the attenuation at $St = 1$ is more remarkable than for the other conditions since the liner resonates at $St_{Resonance} = 1$. It is worth noticing that the attenuation at $St = 1.5$ is greater than the attenuation at $St = 0.5$. This is due to the fact that the reactance is not symmetric around the resonance frequency causing a non-symmetric attenuation.

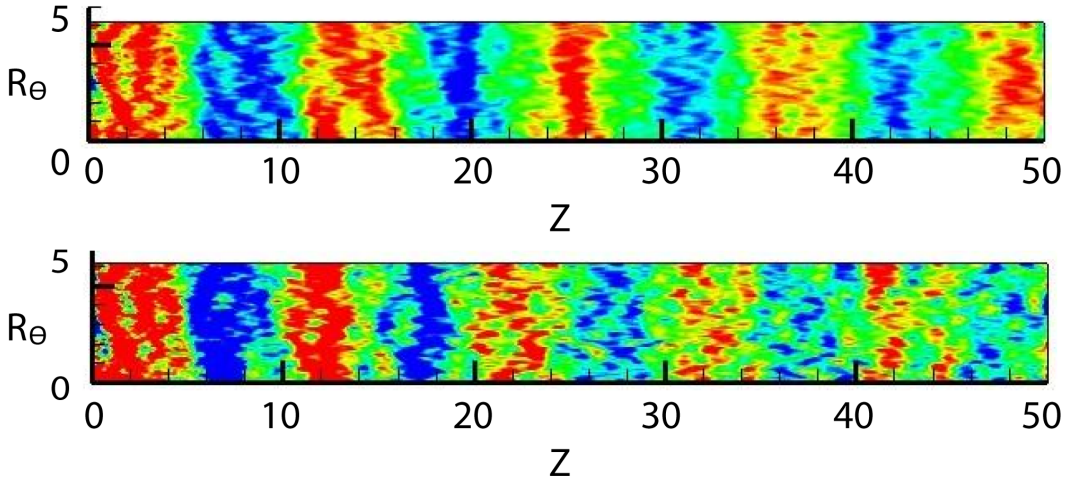


Figure 3.12: *Top: Contours of pressure magnitude for hard-wall case. Bottom: Contours of pressure magnitude for lined-wall case, $R = 1$, $St = 0.5$.*

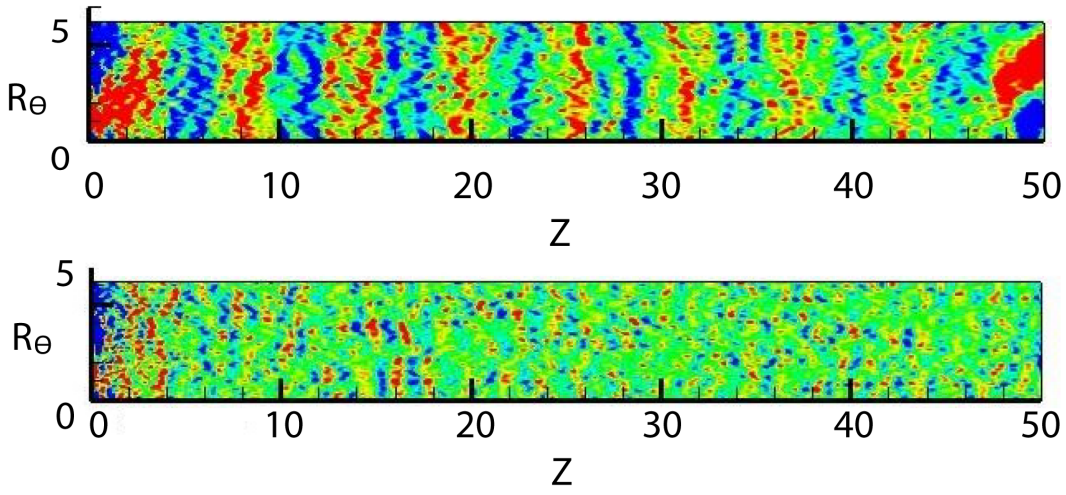


Figure 3.13: *Top: Contours of pressure magnitude for hard-wall case. Bottom: Contours of the pressure magnitude for lined-wall case,* $R = 1$, $St = 1$.

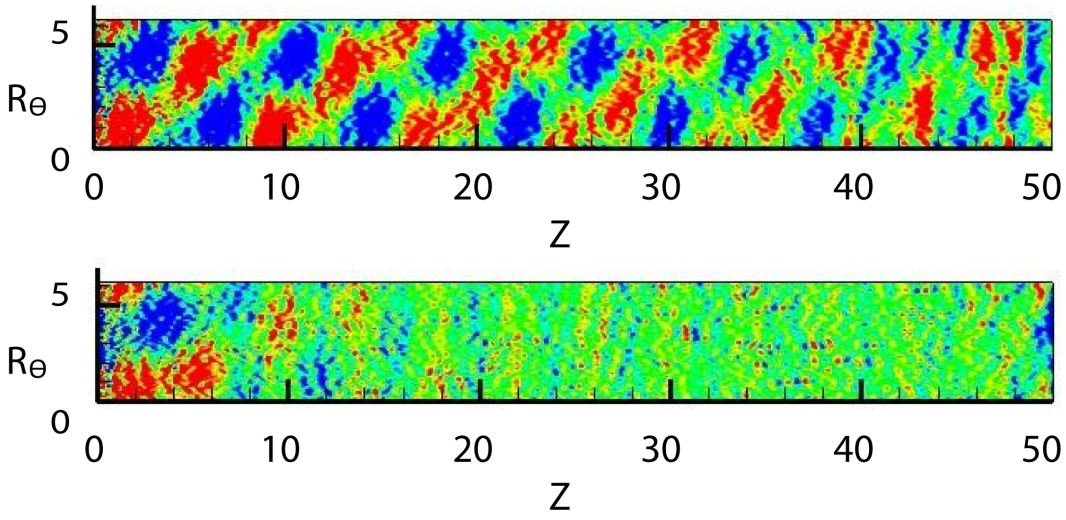


Figure 3.14: *Top: Contours of pressure magnitude for hard-wall case. Bottom: Contours of the pressure magnitude for lined-wall case,* $R = 1$, $St = 1.5$. *At this frequency the spiral mode is clearly visible.*

## 3.6 Liner testing

### 3.6.1 Axisymmetric mode

In this section a number of liners will be tested, and a PSD pressure analysis will be carried out for the 3D turbulent pipe case. Only PSD related to azimuthal mode zero will be shown in this section, higher azimuthal mode analysis will be carried out later in this chapter. Figure 3.15 shows two different liners with the same resistance $R = 4$ and different resonance frequency, $St_{res} = 0.41$ and $St_{res} = 0.7$. Figure 3.16 shows the PSD of the pressure for four different locations on the wall along the pipe, $z = 2, 12, 28, 45$. The black line represents the hard-wall case, the blue and red lines are the lined cases with $St_{res} = 0.41$ and $St_{res} = 0.7$ respectively. In the lined cases the PSD has the maximum attenuation at the resonance frequency, as expected. Furthermore, the attenuation broadens around the resonance frequency as we move downstream, see as in Figure 3.16. It is interesting to study the wall attenuation at the resonance frequencies along the pipe for the liners considered, see Figure 3.17. Both liners create a strong attenuation in the first part of the pipe reducing the internal noise by $10-12dB$. Furthermore, the attenuation tends to be linear up to $z = 15 \sim 20$ after which no further attenuation is achieved.

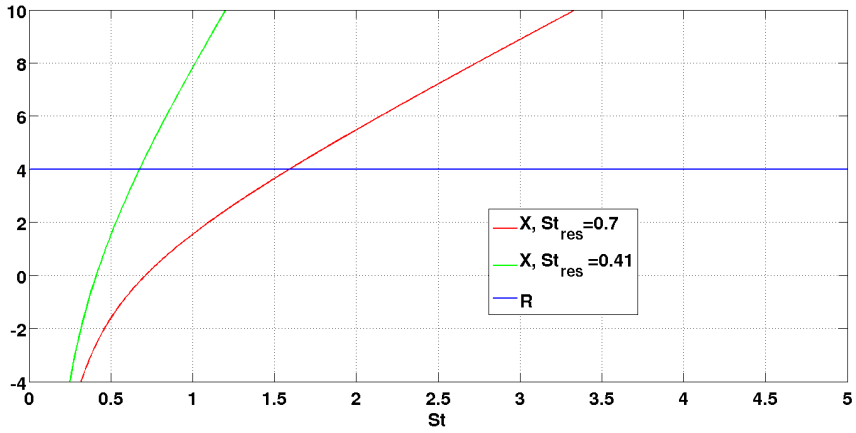


Figure 3.15: *Impedance parameters; two liners with different resonance frequency.*

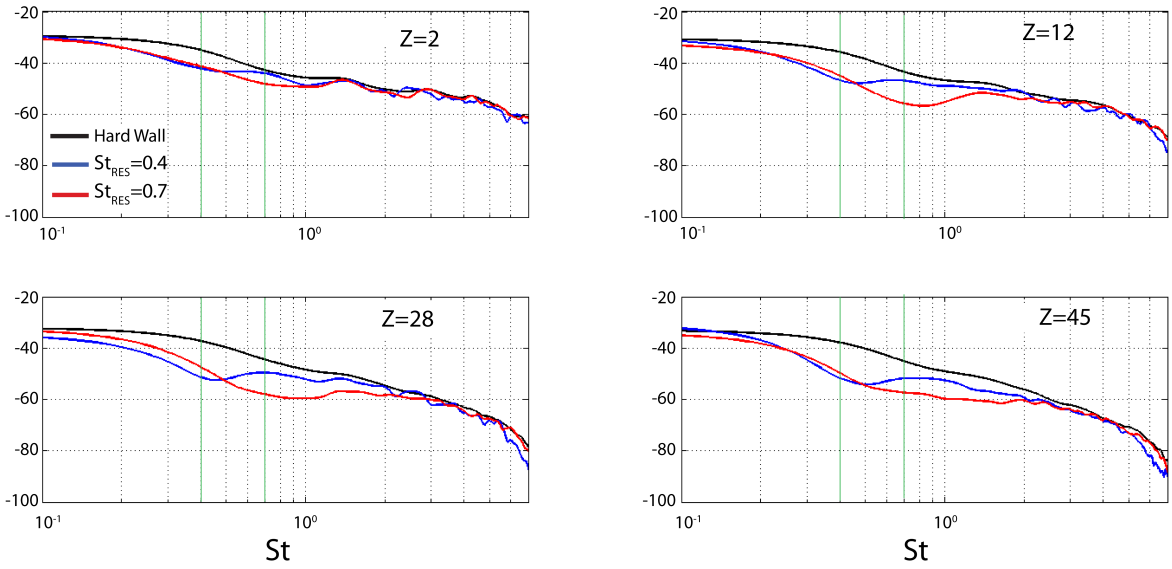


Figure 3.16: *PSD (dB) of pressure from four different location on the wall. The attenuation peak occurs at the resonance frequency. Black line hard wall case; blue line lined case with* $St_{res} = 0.41$*; red line lined case with* $St_{res} = 0.7$*.*

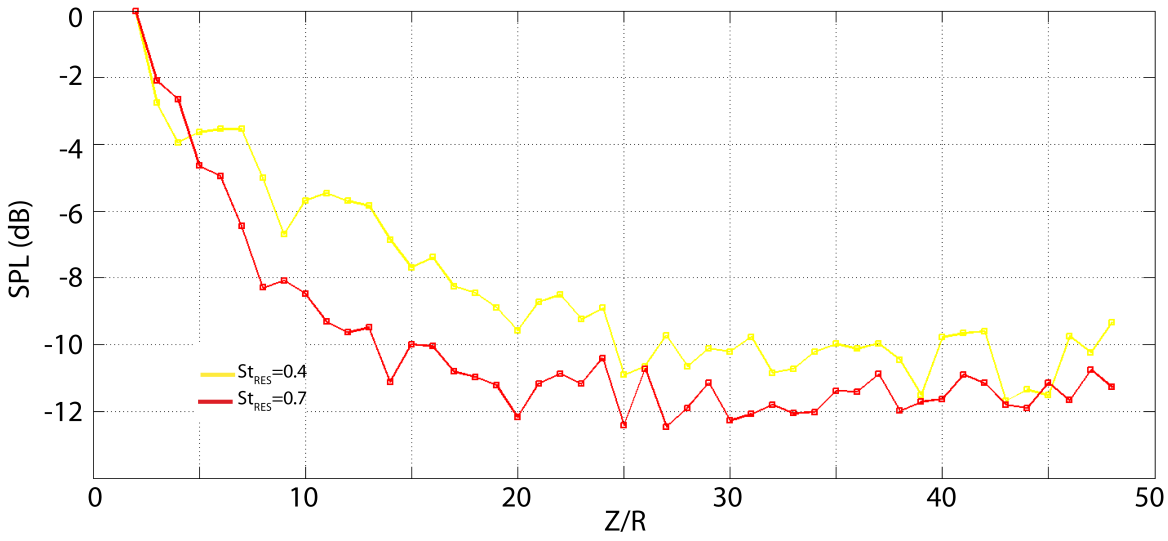


Figure 3.17: *Wall attenuation (dB) at the resonance frequencies. The attenuation saturates after* $20 \sim 25R$.

In Figure 3.18 the attenuation over the frequency domain for the same monitor points is shown. In this picture it is clear how the liner that resonates at $St_{res} = 0.7$ offers a broader attenuation at each axial position. This is due to the fact that the liner with $St_{res} = 0.7$ has a reactance with a lower slope over the frequency domain, see Figure 3.15. This aspect is even more evident if we consider two liners with the same resonance frequency as in the following case. In Figure 3.19 the impedance parameters for two different liners are shown. They both resonate at $St_{res} = 1$, but the second liner (red line; $X_2 = -22.6080, X_1 = 0.5732$) has a reactance with a smaller slope compared with the first liner (green line; $X_2 = -15.072, X_1 = 0.3822$).

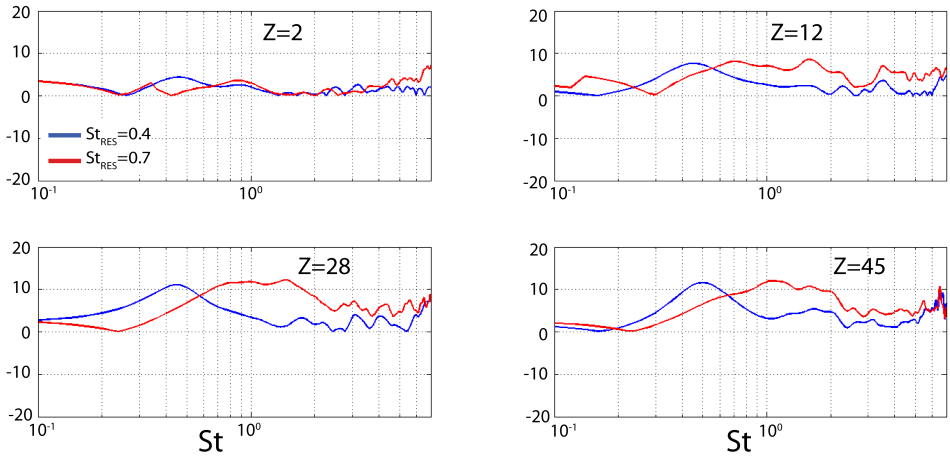


Figure 3.18: *Attenuation over the frequency domain from four locations on the wall. The amplitude is comparable for both cases, but the second liner offers a broader attenuation.*

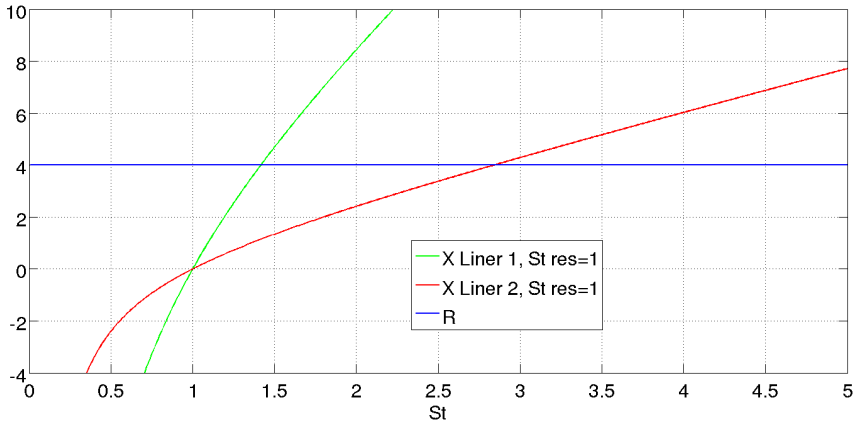


Figure 3.19: *Impedance parameters; Two liners with different reactance slope.*

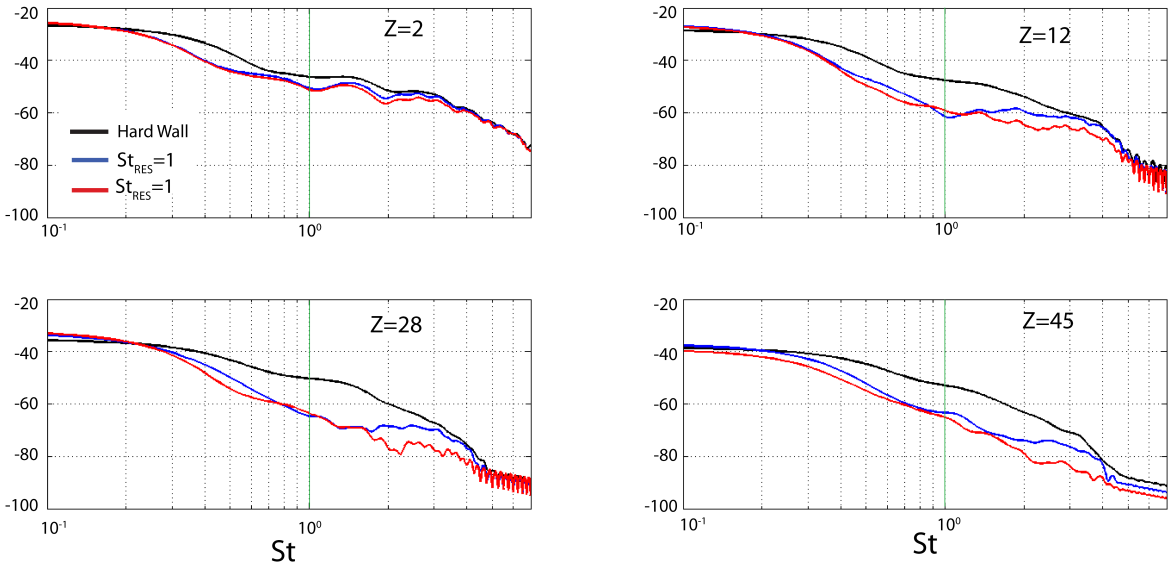


Figure 3.20: *PSD (dB) of pressure from four different locations on the wall. Black line hard wall case; blue line lined case with liner 1; red line lined case with liner 2.*

The PSD of the wall pressure for four axial positions is shown in Figure 3.20. As expected both liners resonate at the resonance frequency but the liner with a lower slope (red line) offers a broader attenuation. Figure 3.21 shows the attenuation over the frequency domain, the second liner creates a broader attenuation. In Figure 3.22 wall attenuation at the resonance frequency is shown. Both liners give the same attenuation which saturates at $z = 20$. Therefore, the slope of the reactance does not affect the attenuation at the resonance frequency.

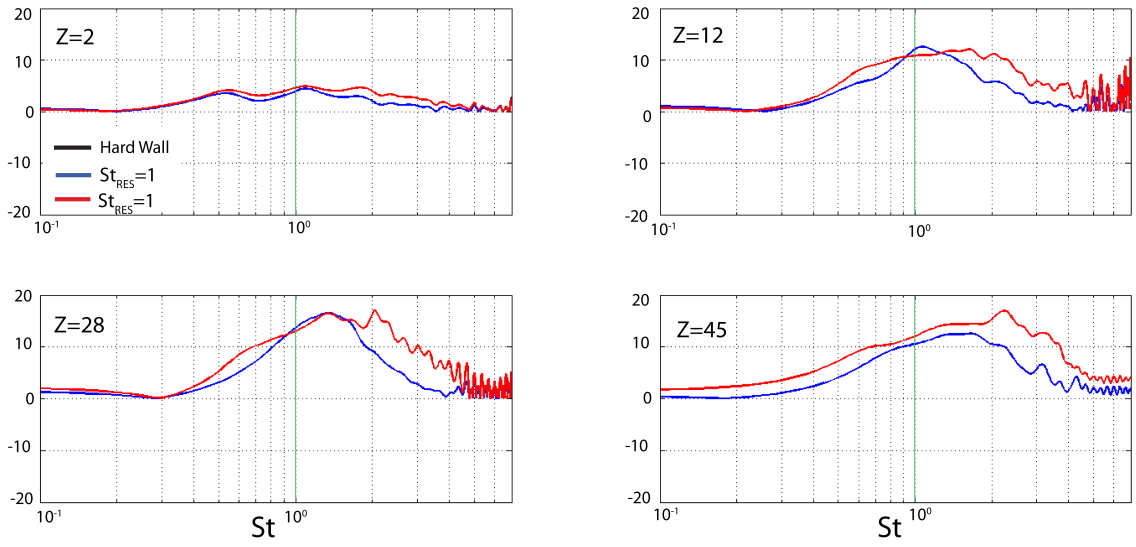


Figure 3.21: *Attenuation over the frequency domain from four locations on the wall. Both liners resonate at the same frequency, but the second liner offers a broader attenuation.*

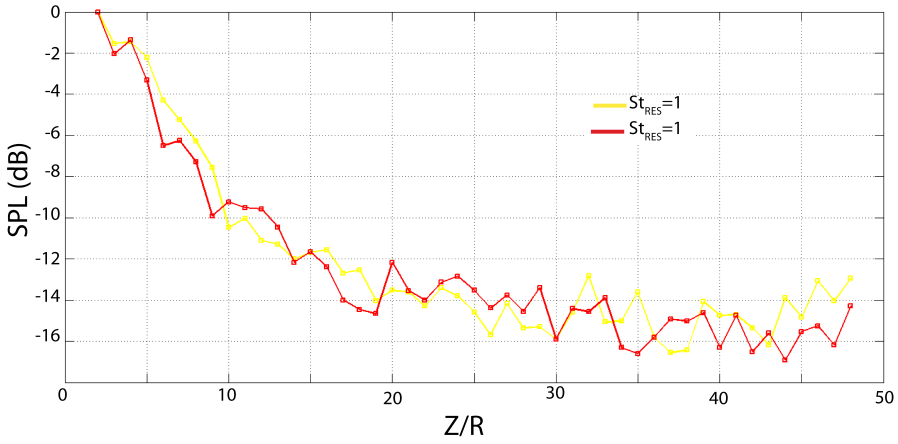


Figure 3.22: *Wall attenuation (dB) at the resonance frequency. The attenuation saturates after* $20 \sim 25R$.

### 3.6.2 Higher azimuthal modes

So far only the axisymmetric mode in the pipe was investigated. In the following the wall attenuation for higher modes, $m > 0$, will be analysed. In this case the attenuation is studied for a liner with $St_{Res} = 0.7$. Figure 3.23a shows the wall attenuation for mode zero along the pipe. As expected the attenuation starts peaking at $St_{Res} = 0.7$. In the first part of the pipe, say from $z = 0$ upto $z = 20$ the attenuation has a linear-like trend as already shown previously in the Figures 3.17 and 3.22. Furthermore, the attenuation tends to broaden in the downstream direction. At the pipe outlet, say $z = 45 \sim 50$ the attenuation seems to disappear. This is due to the interaction with the Characteristic Boundary Condition (CBC) set at the outlet. Therefore, no physical consideration is made in this region. As for the higher modes, shown in Figures 3.23b, 3.23c and 3.23d, the attenuation occurs above the cut on frequencies as expected. In this case the cut on frequencies are defined as $St_{cuton} = \alpha_{mn}\sqrt{(1 - M^2)/(\pi M)}$, where $\alpha_{mn}$ are the zeros of the Bessel function. The magnitude of the attenuation reaches $10dB$ for mode zero while in the higher modes the attenuation reaches $15dB$. The attenuation of higher modes, m= 1, 2, 3, reaches a maximum and then reduces at a fixed $St$. The liner attenuation is increasingly more effective with distance downstream, although for higher modes $m = 1, 2, 3$ at a fixed St the attenuation reaches a maximum and then reduces. This may be due to additional noise being generated by the turbulent pipe flow.

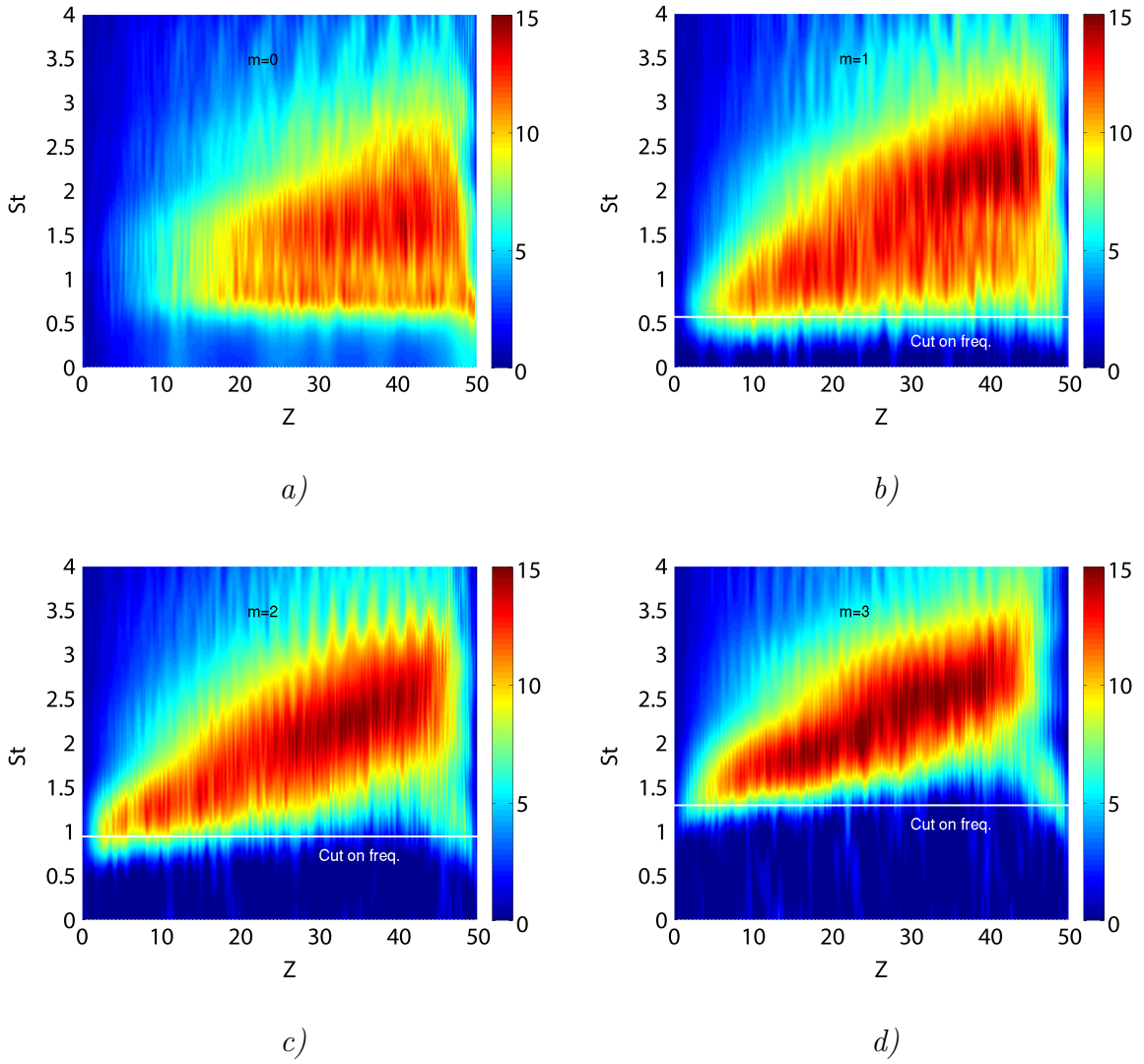


Figure 3.23: *Attenuation for modes 0,1,2,3. Horizontal axis: axial coordinate Z, vertical axis: frequency St. Horizontal white line: cut on frequency.*

### 3.6.3 Parametric study of the liner attenuation.

A more general parametric study can be carried out to evaluate the effect of reactance characteristics on the attenuation. Figure 3.24 shows a number of liners with different slopes at the same resonance frequency, $(dX/dSt)_{St_{res}}$. The resonance frequency is $St = 0.7$ for all the liners. Figure 3.25 shows the attenuation over $(dX/dSt)_{St_{res}}$ calculated close to the pipe outlet , $z = 45$. As $(dX/dSt)_{St_{res}}$ increases the attenuation decreases converging towards a certain value, say, 4.5 in this case. Therefore, the smaller $(dX/dSt)_{St_{res}}$, the higher the attenuation. From a computational point of view, $(dX/dSt)_{St_{res}}$ can not be smaller than a certain value as otherwise the DNS simulation might face numerical instabilities. This becomes evident if we consider the coefficient $X_1$ in the Eq. 3.11, As $(dX/dSt)_{St_{res}}$ decreases $X_1$ decreases as well as causing a division by zero.

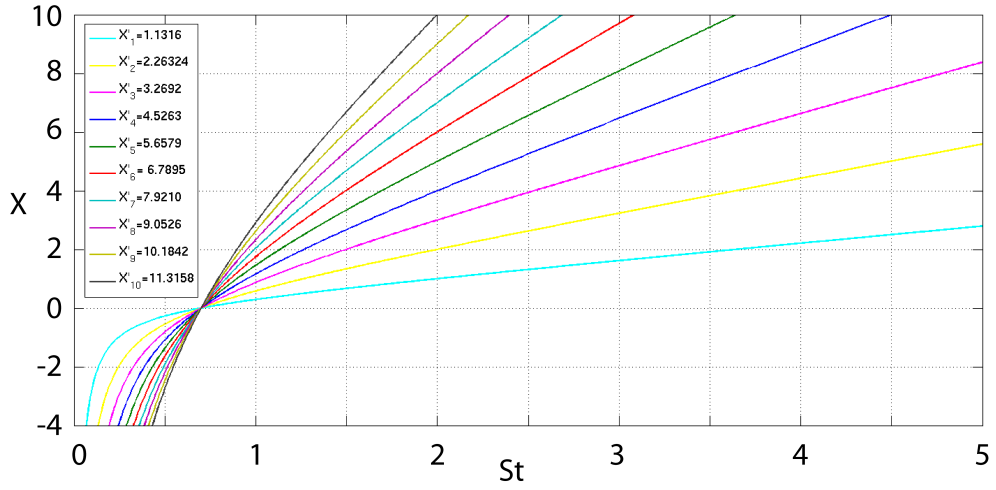


Figure 3.24: *A number of liners with different reactance slope at the resonance frequency,* $X' = (dX/dSt)_{St_{res}}$.

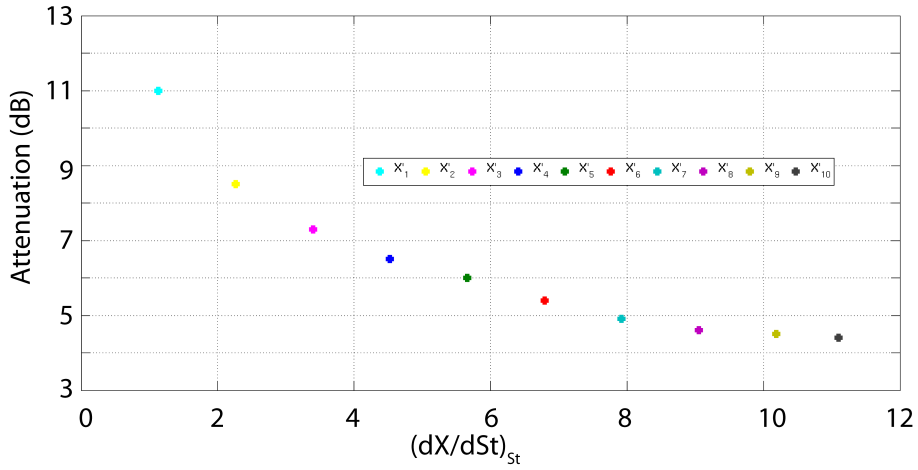


Figure 3.25: *Over all sound pressure attenuation over* $X' = (dX/dSt)_{St_{res}}$.

### 3.6.4 Validation of turbulent statistics.

In order to verify that the flow field maintains its characteristics from a statistical point of view when a liner is present, the Reynolds stress components are computed and compared to the results by Wu & Moin [66] who provide statistical characteristics for a similar hard-walled turbulent pipe flow. Figure 3.26 shows the root mean squared of the stress components $< u'u' >$, $< v'v' >$, $< w'w' >$ and $< u'v' >$ for a lined wall case with $R = 4$ and $St_{resonance} = 0.41$. The dashed line are the benchmark results from Wu & Moin [66], the squared symbols are the lined case and the solid line is the hard wall case obtained with the current code. Three zones are highlighted: zone 1 is included in the subviscous layer, whereas zone 2 and zone 3 are included in the buffer layer and logarithmic layers respectively. As we can see from Figure 3.26 there is a good match between the lined (squares) and wall (solid) cases from DNS simulation. The agreement between the DNS results and the reference case (dashed line) is also

good.

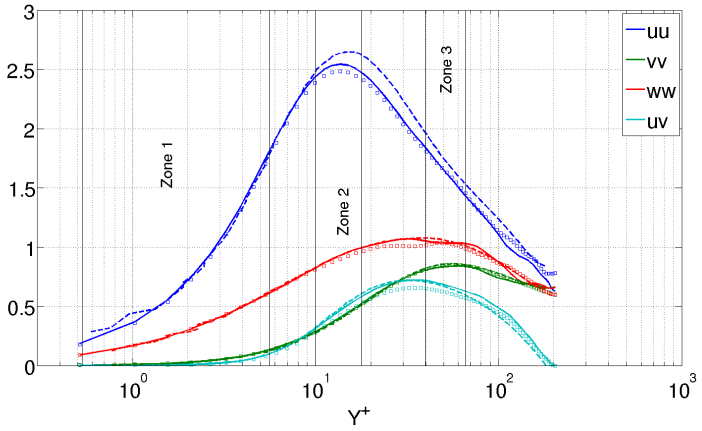


Figure 3.26: *Reynolds stress components in wall units,* $St_{res} = 0.41$. *Dashed lines denote reference solution from Wu & Moin [66]; solid lines hard-wall case; dots lined wall case.*

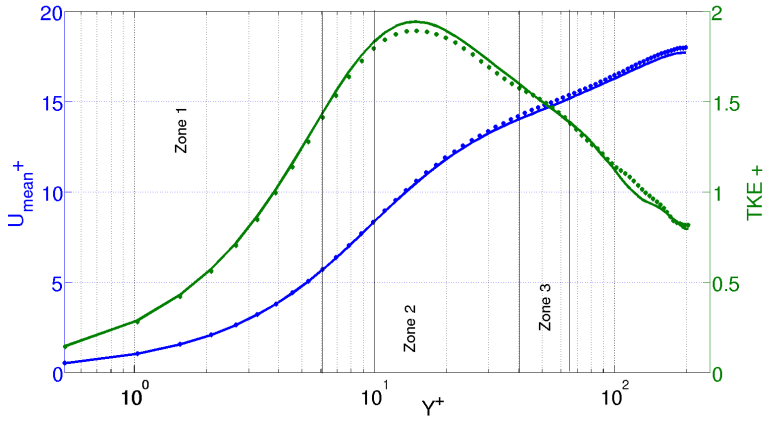


Figure 3.27: *Blue:* $U^+_{mean}$. *Green:* $TKE^+$. *Solid lines hard wall case; dots lined wall case.* $St_{res} = 0.41$.

If we look carefully at the comparison between the DNS results and the reference results in Figure 3.26, both the lined and hard wall case show lower values for $< u'u' >$ in the range $Y^+ > 10$. This is due to a small increase in $u_\tau$ at the wall. Since the DNS hard-wall and lined-wall cases show the same discrepancy in comparison to the reference data, we can assume that the discrepancy does not depend on the presence of the liner model but rather on the overall setup of the simulations, in particular the inflow turbulence generation. Furthermore, the $uv$ Reynolds stress component from the lined-case around $Y^+ = 30$ is reduced by 10 % in comparison to the hard-wall case. Figure 3.27 shows the turbulent kinetic energy ($TKE$) and the mean velocity profile ($U_m$) for the lined and hard-wall case in wall coordinates. The comparison shows a good agreement. Other researchers such as Scalo *et al.* [67] performed computational simulations for compressible turbulent channel flows with impedance boundary conditions, and they observed alterations in the turbulent flow structure near the wall. However, it is worth mentioning that they tuned the resonant frequency to the characteristic time scale of the outer layer eddies, taken as the ratio of the bulk velocity over the boundary layer thickness. As a result the Reynolds stress component $< u'v' >$ increased by 70 % [67]. Scalo *et al.* [67] also suggest that the turbulent flow structure alteration cannot only be attributed to inviscid Kelvin-Helmhotz instability mechanisms, and further stability analysis should be carried out in future work. In the present work no such great alterations of the turbulent structures are observed as different liner parameters were chosen. Although differences are observed between the lined and hard-wall cases, they are considered to be sufficiently small to claim that the flow field itself is not affected substantially by the presence of the liner. Figures 3.28 and 3.29 show the same comparison as previously but this time with a different liner setting, namely

$R = 1$ and $X_{resonance} = 0.7$. Again the comparison shows good agreement. This is an important result since it means that the turbulent flow is statistically independent of acoustic liner parameters if these are not consciously tuned to affect the flow [67]. More comparisons with different liner setting have been computed confirming the independence of the turbulent statistics from the presence of the liner. These results are not shown here for brevity. It is important to notice that the turbulent statistics are not affected substantially by the presence of the liner model only when no real cavities are present on the wall. In the present work the liner model implemented simulates only the acoustic effect on the flow field as the lined wall is still a smooth surface. When real cavities are present on the wall, such as in the case with honeycomb liners, vorticity is injected into the cavities. Therefore a hydrodynamic interaction between the flow field and the cavities exists. Tam *et al.* [25] observed that the shed vortices generated on a resonating cavity tend to evolve into rings and align themselves into two regularly spaced vortex trains moving away from the resonator opening in opposite directions. These results show that the presence of the liner affects the flow on the wall. Therefore, statistically the turbulent field might have different values in the presence of a real acoustic liner. The purpose of the present work is to study only the acoustic effect of the Tam and Aurialt model [19] on a turbulent pipe flow.

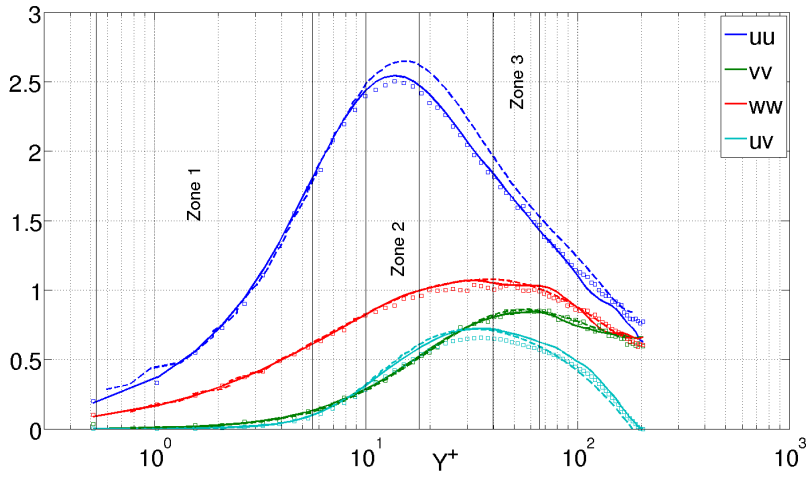


Figure 3.28: *Reynolds stress components in wall units,* $St_{res} = 0.7$. *Dashed lines denote reference solution from Wu & Moin [66]; solid lines hard-wall case; dots lined wall case.*

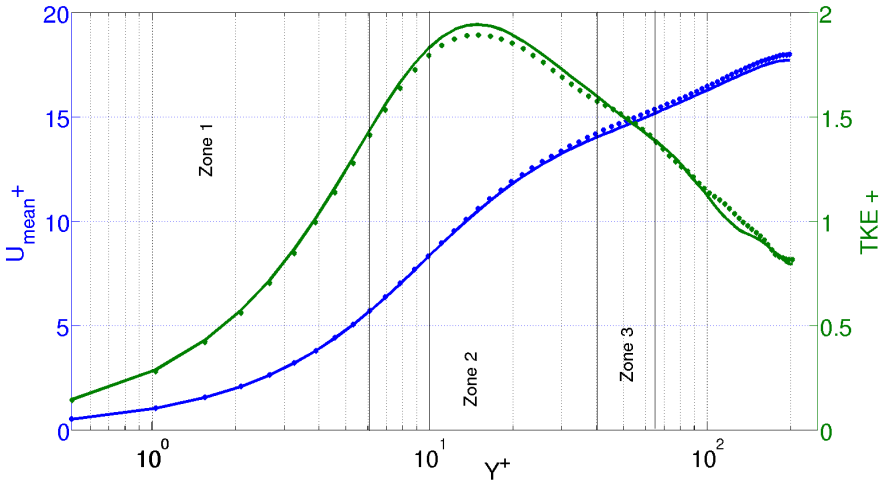


Figure 3.29: *Blue:* $U^+_{mean}$. *Green:* $TKE^+$. *Solid lines hard wall case; dots lined wall case.* $St_{res} = 0.7$.

## 3.7 Conclusions

In this chapter the implementation of the Tam and Auriault model into a DNS code and its validation has been described. The validation has shown good agreement with expected results. The acoustic attenuation capability has also been tested using different liner parameters. The results meet the expectations in terms of bandwidth attenuation. Furthermore, the presence of the liner model has shown no significant effect on the statistics of the flow. This encourages us to continue our investigation into the acoustic capabilities of the liner model implemented.

# Chapter 4

# Liner model attenuation capability

In this chapter the acoustic attenuation of 3D pipe test cases with different Mach numbers will be studied. Furthermore, a manipulation of the pipe inlet conditions will be attempted to reduce the noise internally generated. In the second part of this chapter a wavenumber-frequency analysis will be carried out to obtain a better understanding of the liner attenuation mechanisms and how the liner model interacts with the pipe flow.

## 4.1 Effect of Mach number on the liner performance

In this section two fully turbulent pipe flows with different Mach number are compared. The first case is characterized with $M = 0.46$ denoted by $M046$, and the second case with $M = 0.84$, $M084$. The numerical set up is the same as the previous pipe test cases, see Section 3.5. The target of this application is to achieve the highest attenuation possible. A number of liners have been tested to obtain the highest attenuation possible

for the current test cases at the resonance frequency $St_{resonance} = 1$. The reactance of the best liner configuration is shown Figure 4.1. The reactance coefficients are $X_1 = 0.16$ with $X_2 = -6.28$ for $M = 0.46$ and $X_1 = 0.85$, $X_2 = -33.49$ for $M = 0.84$. The resistance is $R = 4$ for both cases.

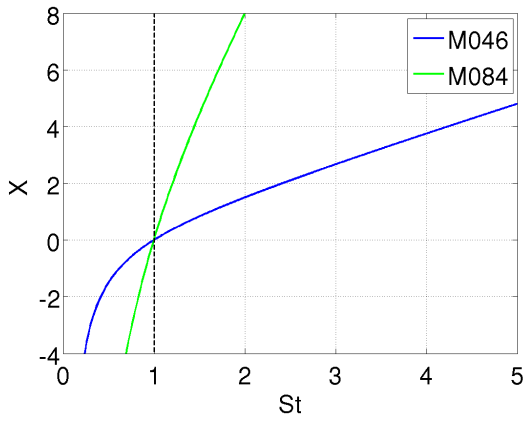


Figure 4.1: *Reactance of liner impedance configuration for the test case* $M046$ *and* $M084$*; Resonance frequency* $St_{resonance} = 1$.

Figure 4.2 shows the $PSD$ of pressure attenuation for the $M046$ test case. The attenuation of the first four modes is displayed for four different axial positions. The attenuation for mode zero, Figure 4.2a, shows a peak at $St = 1$ which corresponds to the resonance frequency at which the liner has been set. The attenuation appears to increase up to $10dB$ over the axial positions. As for the higher modes the attenuation reaches $10dB$ as well above the cut-on frequency. Figure 4.3 shows the $PSD$ of pressure attenuation for the $M084$ test case. Figure 4.3a shows a correct peak position at $St_{resonance} = 1$. In this case the attenuation reaches $15dB$. The higher modes show the same attenuation magnitude above the cut-on frequency. The difference in attenuation

performance between the test cases might be due to the different acoustic content. In other words, in the $M084$ case the flow is more noisy than the flow in the $M046$ case, therefore, the liner model is capable of attenuating a higher noise level.

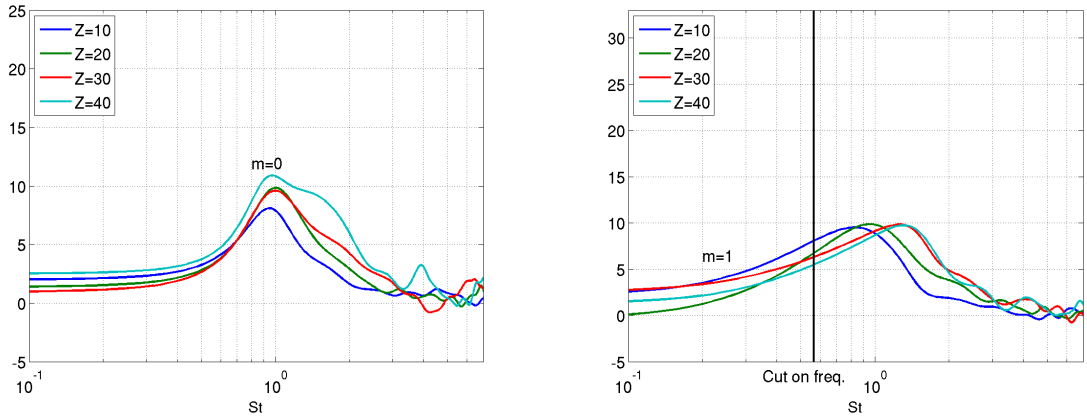


$(a)$




$(b)$

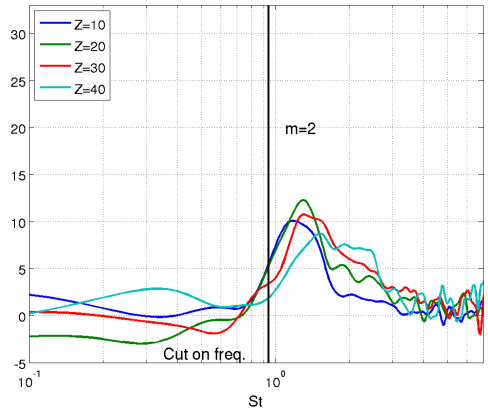


$(c)$

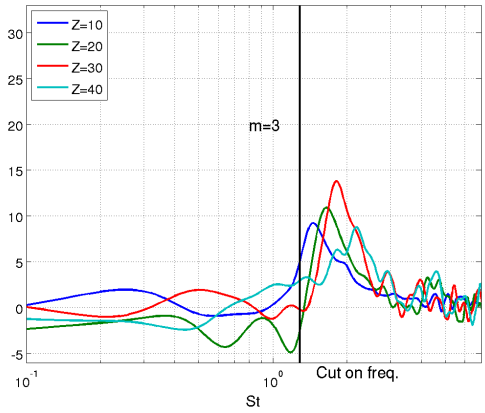


$(d)$

Figure 4.2: *PSD of pressure attenuation for* $M046$ *test case. a) Azimuthal mode zero. b) Azimuthal mode 1. c) Azimuthal mode 2. d) Azimuthal mode 3.*

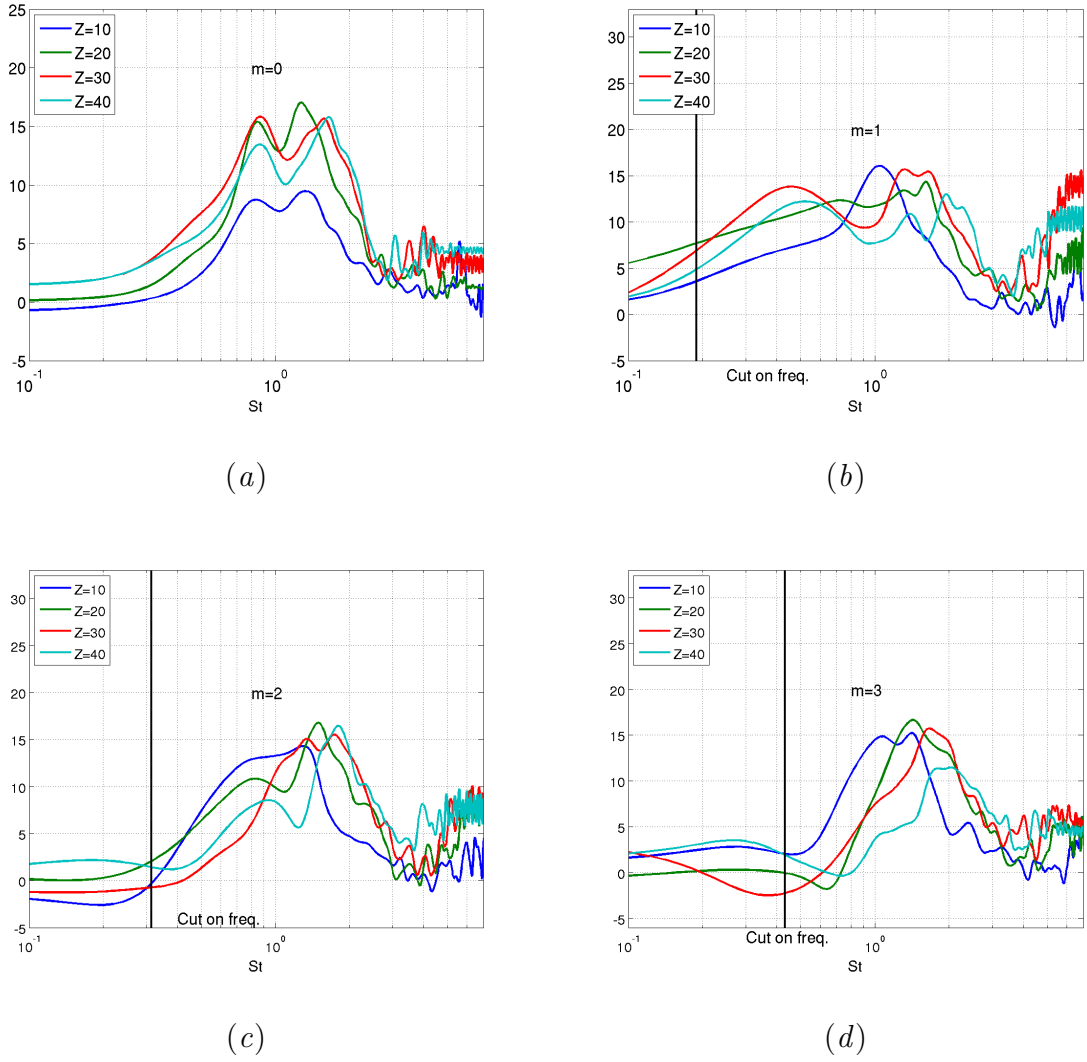


Figure 4.3: *PSD of pressure attenuation for M084 test case. a) Azimuthal mode zero. b) Azimuthal mode 1. c) Azimuthal mode 2. d) Azimuthal mode 3.*

## 4.2 Noise reduction by manipulating turbulent inlet condition

Observing Figures 3.17 and 3.22 it is clear that a possible source of sound is located at the pipe inlet since the highest attenuation rate is in the first half of the pipe. Figures 3.17 and 3.22 show a linear attenuation from the inlet up to 25-30 radii after which the attenuation saturates. In the DNS code the turbulence is generated using a digital filter technique [60]. This suggests that the artificial turbulent conditions applied at the inlet in terms of velocity are characterized by an acoustic component. As a result, acoustic energy is injected into the pipe flow. In order to reduce the magnitude of the sound source at the pipe inlet a manipulation of the inlet condition is attempted. The fluctuating part of the velocity components, $u', v'$ and $w'$, are set to zero for the azimuthal mode zero. The components $u', v'$ and $w'$ are left untouched for higher azimuthal modes. New turbulent pipe cases are computed with the new inlet conditions and compared to the previous test case with the original inflow conditions. The first test case to be analysed is for $M = 0.46$ ($M046$). The pressure energy reduction caused by the inlet flow manipulation is studied in terms of $PSD$. Figure 4.4 shows the attenuation between the old and new pipe case for different modes, $\Delta PSD = PSD_{Old}$ - $PSD_{New}$. Figure 4.4a shows $\Delta PSD$ for mode zero at different wall locations (z=10, z=20, z=30, z=40).

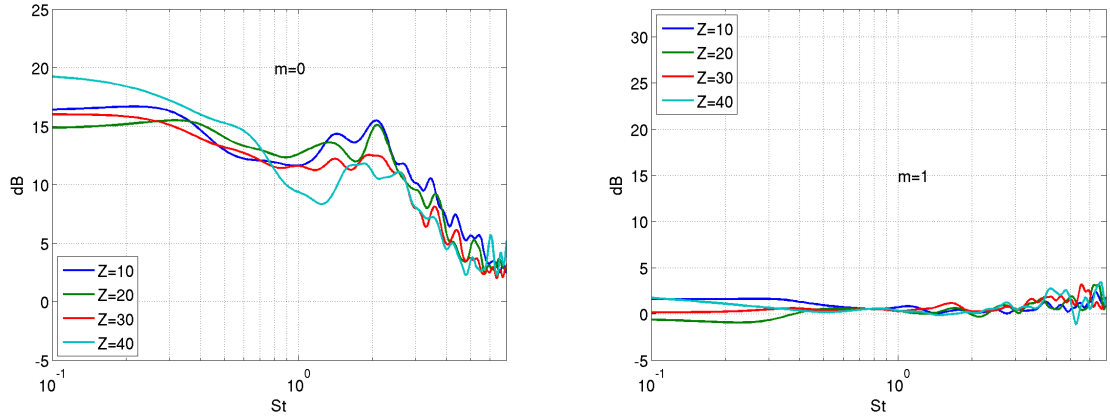


(a)




(b)

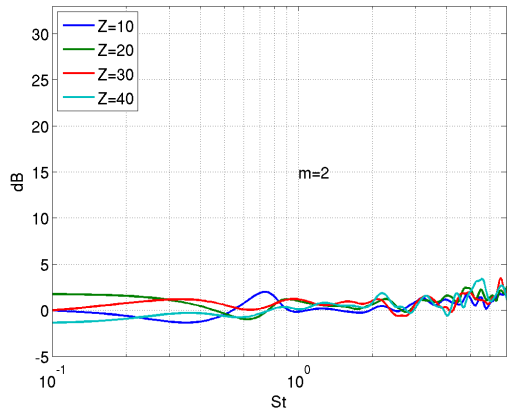


(c)

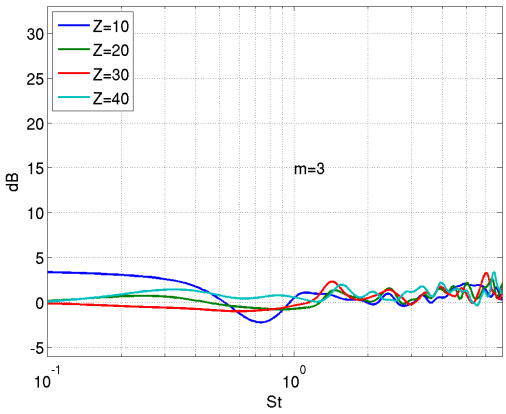


(d)

Figure 4.4: *M*046 *test case. Comparison between the previous pipe case and the new pipe case where the fluctuating part of the velocity components at the inlet boundary are set to zero for the azimuthal mode zero,* $\Delta PSD$*. a) Azimuthal mode zero. b) Azimuthal mode 1. c) Azimuthal mode 2. d) Azimuthal mode 3.*

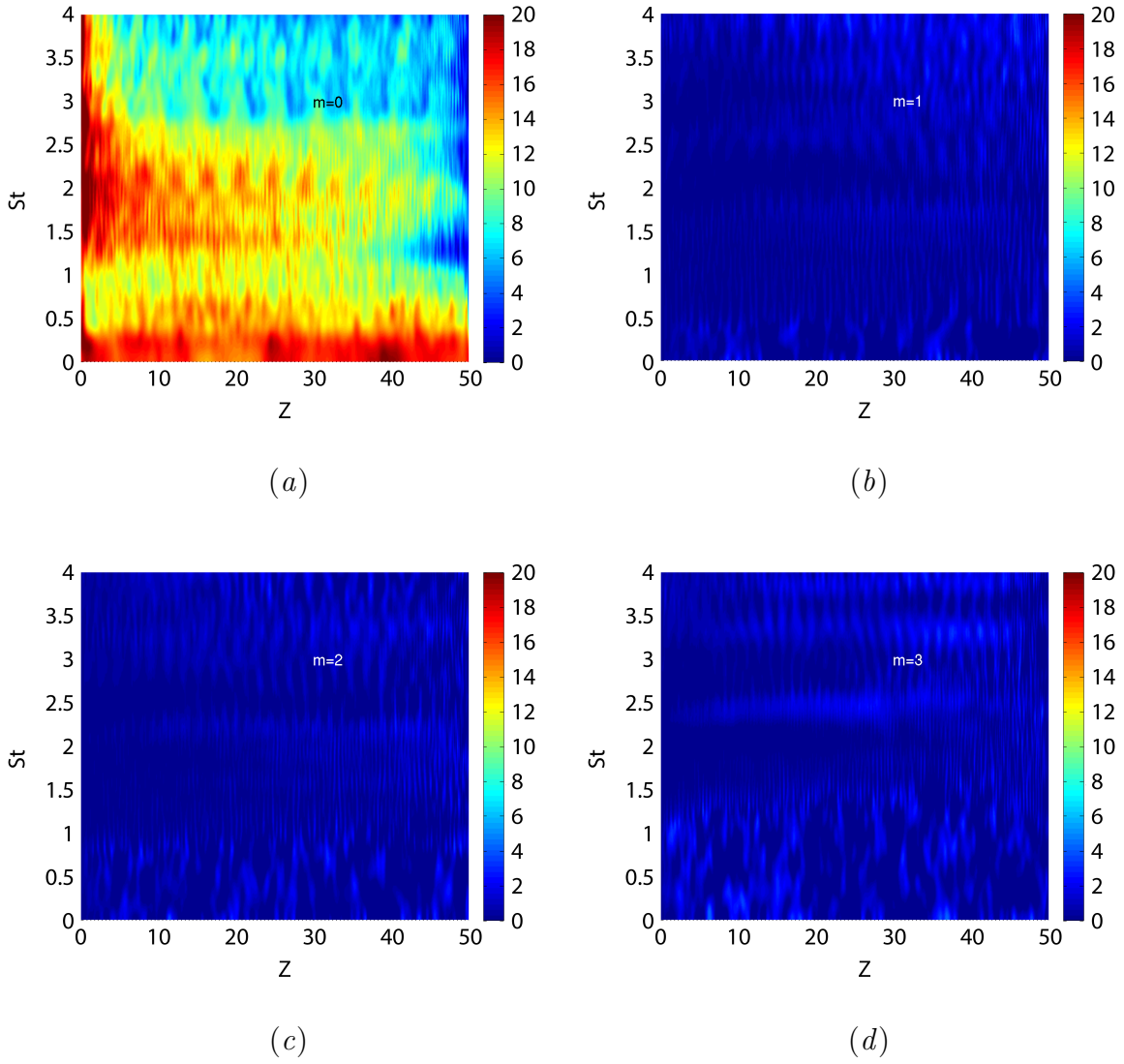


Figure 4.5: *M*046 *test case. Frequency domain over axial position. Comparison between the previous pipe case and the new pipe case where the fluctuating part of the velocity components are set to zero for the azimuthal mode zero at the inlet,* $\Delta PSD(dB)$.

As expected the $\Delta PSD$ at azimuthal mode zero is remarkably high, it reaches peak of about $20dB$ at the outlet, z=40. As for the higher modes, shown in Figures 4.4b, 4.4c and 4.4d, $\Delta PSD$ is close to zero since no manipulation is applied. Figure 4.5 shows the difference between the old case and new test case for different modes along the pipe wall. This gives a wider view on the difference between the two cases compared to Figure 4.4, which shows a cut through Figure 4.5 at certain $z$ location. Figure 4.5a shows a relevant difference for the low frequencies, say $St = 0.1 \sim 1$. The flow in the first part of the pipe ($z = 0 \sim 20$) should not be considered physical since the new inlet conditions cause a slightly longer transient before fully developed turbulence is obtained. Figures 4.5b, 4.5c and 4.5d show no variation in the $PSD$. Therefore, an acoustic liner would still play an important role in the internal noise attenuation for higher modes as shown in the next paragraph.

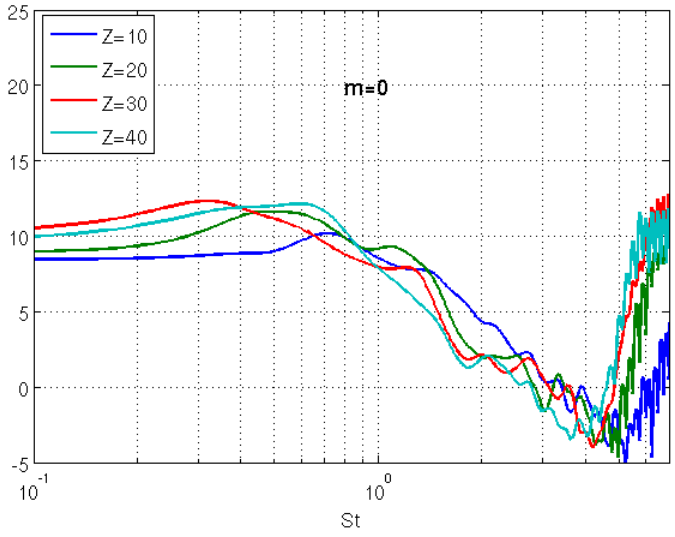


Figure 4.6: *M*084 *test case. Pressure attenuation of mode zero, PSD dB.*

The same manipulation is applied to the second test case with $M = 0.84$ ($M084$). Figure 4.6 shows the $PSD$ of pressure attenuation of mode zero for four different axial positions. The attenuation reaches $13dB$ in the frequency range $0.2 < St < 0.8$ and is therefore well below the attenuation level for the $M046$ case, see Figure 4.4a. As in the previous test case ($M046$) the higher modes remain unchanged.

### 4.2.1 Acoustic liner applied to new test cases

It is now useful to study the liner attenuation capability with the new inflow conditions for the test cases $M046$ and $M084$. The liner parameters are the same as those used in the previous Paragraph 4.1. The first test case to be studied is $M046$. Figure 4.7 shows the pressure $PSD$ attenuation at the wall for the axisymmetric and the first azimuthal Fourier mode in the frequency domain. The axisymmetric mode shows a modest attenuation at high frequencies, $St > 2.5$, while higher modes show a broader attenuation above the cut on frequency. In Figure 4.7b, an attenuation up to $30dB$ can be observed. The liner attenuation is increasingly more effective with distance downstream. Figure 4.7a shows no attenuation around $St = 1$, from which we deduce that here the acoustic field is dominated by the turbulent pressure field. This is due to the absence of noise in the low frequency range for mode zero. In contrast mode 1, Figure 4.7b, shows a modest attenuation around $St_{resonance} = 1$ where the cut-on broad band noise is more significant. Figures 4.7c and 4.7d show a similar trend. In the higher modes, $m = 1, 2, 3$, the peak of the attenuation appears to shift towards high frequencies as we move downstream. This may be due to additional noise being generated by the turbulent pipe flow. As expected the attenuation occurs above the

cut on frequency. Towards the outlet, $z > 45$, the attenuation seems to disappear altogether. This is due to the effect of the characteristic boundary condition (CBC) applied in this region, which is characterized by non-physical flow.

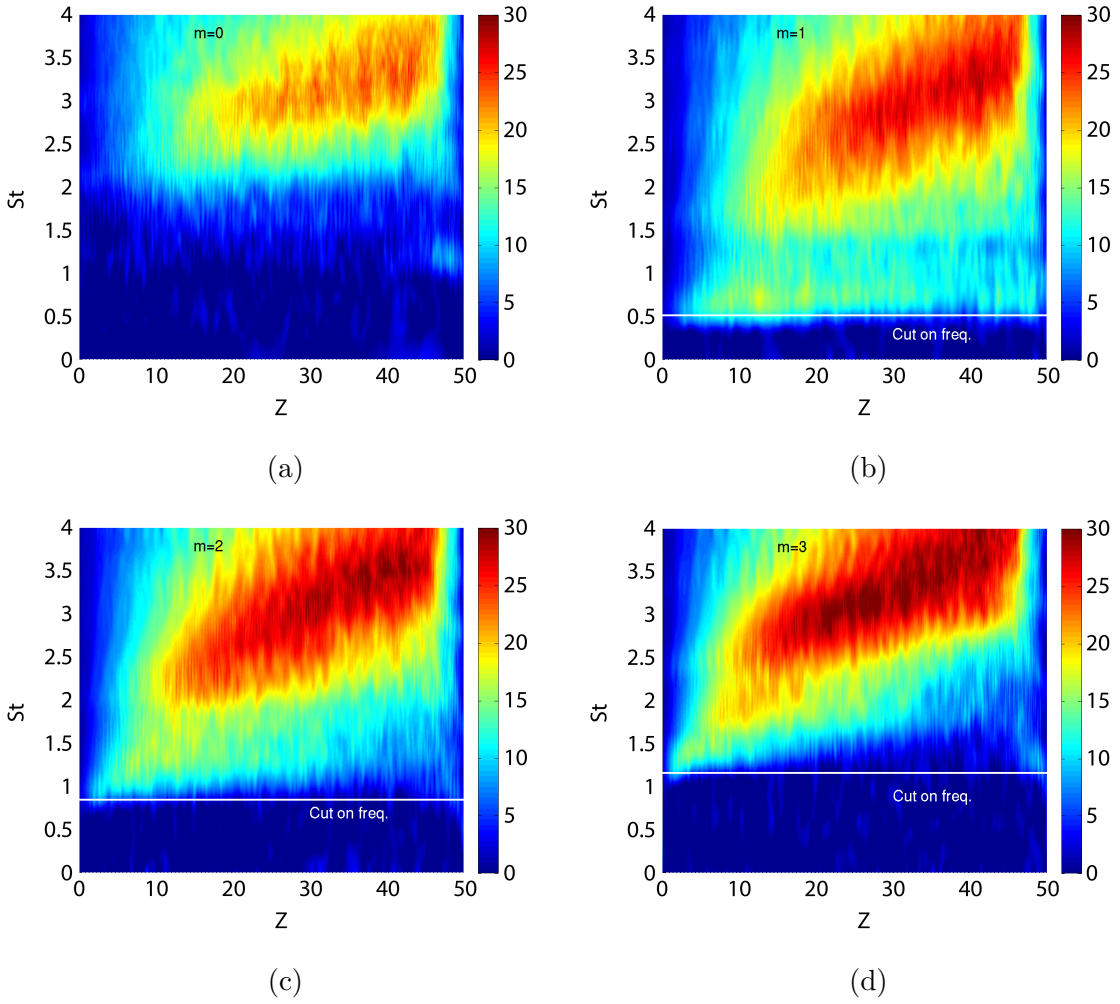


Figure 4.7: *M*046 *test case with new inflow boundary conditions. Wall attenuation (dB) for four azimuthal modes; white line denotes cut on frequency. a) Azimuthal mode 0. b) Azimuthal mode 1. c) Azimuthal mode 2. b) Azimuthal mode 3.*

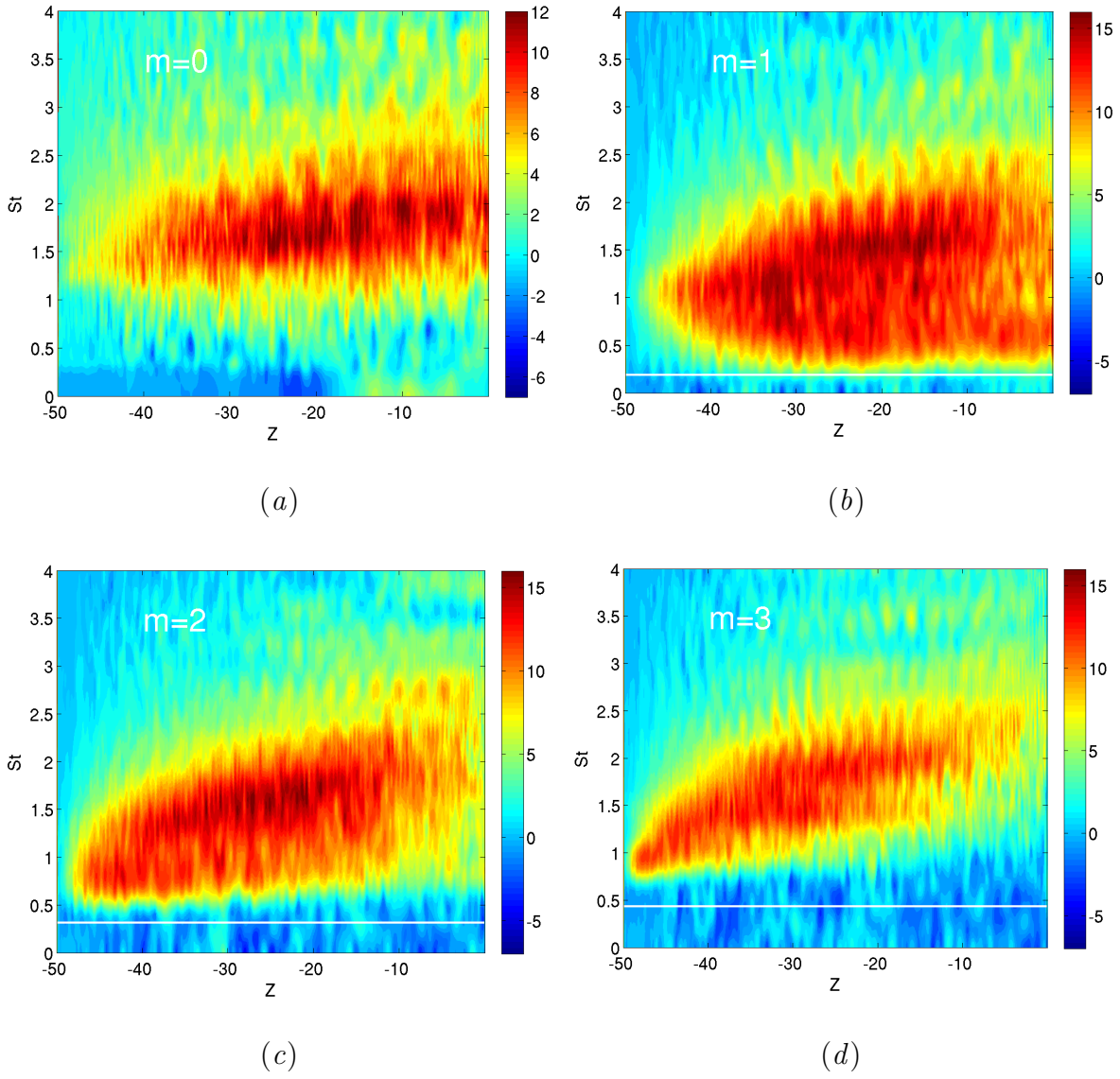


Figure 4.8: *M084 a) Azimuthal mode zero. b) Azimuthal mode 1. c) Azimuthal mode 2. d) Azimuthal mode 3.*

Figure 4.8 shows the pressure attenuation of the first fours modes for the $M084$ case. Figure 4.8a shows an attenuation about $St = 1.5$ which reaches 12dB for mode

zero. As in the previous case, $M046$, there is hardly any attenuation performed by the liner around the resonance frequency, $St_{resonance} = 1$ when the inlet flow conditions are modified. Once again this may be due to the absence of noise at low frequencies. In Figure 4.8b shows the attenuation for the first mode. In this case the attenuation clearly peaks around $St_{resonance} = 1$ above the cut-on frequency, reaching 15 dB. As for the higher modes Figures 4.8c and 4.8d, the attenuation reaches 15 dB. As observed in the previous case, $M046$, the peak of the attenuation shifts towards high frequencies as we move downstream. This may be due to additional noise generated by the turbulent pipe flow. The attenuation in the $M084$ occurs at lower frequencies than in the $M046$ case, see Figures 4.8 and 4.7. This is due to the fact that increasing the Mach number lowers the cut on frequency, therefore the attenuation peak lowers as well.

## 4.3 Wavenumber analysis

One way to separate acoustic and aerodynamic pressure in the wall pressure fluctuations is to represent them in the wavenumber domain. Indeed, in the aeronautical case, typically the acoustic and turbulent wavenumbers are different from each other by a factor between 1.25 and 2.5 , since the Mach number of interest for aerodynamic noise can be between 0.4 and 0.8. In other applications such as ventilation systems or automotive this factor could be 10 since the Mach number is about 0.1. Previously researchers proposed different method for wavenumber-frequency analysis. Bull [29] recently wrote a review of the different wavenumber spectra measurement methods. A possible approach consists of a direct measurement of the wavenumber spectral density, by spatial discrete Fourier transform of the cross-power spectral densities. This

requires a low-pass wavenumber filtering and a great number of microphones according to Shannon's sampling theorem. That is why very few publications using this method are available (Ibars in 1990 [30], Manoha in 1993 [31], or Abraham in 1998 [32]). Another possible way is to use arrays of pressure. Maidanik [33] describes the wave-vector filtering action of pressure arrays. Maidanik and Jorgensen [34] propose also enhancements to such arrays. The principle consists in obtaining, through linear combinations of signals, a wavenumber spectrum for discrete values of the wavenumber, depending on the spacing between microphones. Many authors [35] [36] have put this method into practice. Using Corcos' [37] hypothesis that longitudinal and transversal fluctuations are independent, they only measured one-dimensional spectra in both directions. This kind of approach is often called the Beam Former Method (BFM). The BFM response is formulated by applying the complex pressure at each monitor point by a complex weighting coefficient $w_l(k_l)$, and summing such that the signals at each microphone due to a wave propagating at the beam-steer angle, $\phi$, add in phase

$$\hat{b}(\phi) = \frac{1}{N} \sum_{l=0}^{N-1} p(\bar{z}_l, \omega) w_l(\phi), \tag{4.1}$$

where $z_l = l\Delta z/\beta^2$, $\beta$ is the Doppler factor. The weighting coefficient is given by

$$w_l(\phi) = exp\left[i\left(-M + cos(\theta)\right) k z_l\right]. \tag{4.2}$$

In what follows the beam steer angle is now referred to the directivity angle and denoted by $\theta$ so Eq. 4.3 now reads

$$w_l(\theta) = exp\left[i\left(-M + cos(\theta)\right)kz_l\right], \tag{4.3}$$

and the BF pressure response is denoted as $\hat{P}(\theta)$ so Eq. 4.3 now reads

$$\hat{P}(k_z) = \frac{1}{N}\sum_{l=0}^{N-1} p(\bar{z}_l, \omega) w_l(k_l). \tag{4.4}$$

The directivity angle varies from zero to 90° for waves propagating in the downstream direction and from 90° to 180° wave propagating in the upstream direction. The weighting coefficient can also be written in terms of the axial wavenumber

$$w_l(k_l) = exp\left(ik_z z_l\right), \tag{4.5}$$

where

$$k_z/k = \left(-M \pm cos(\theta)/(1 - M^2)\right). \tag{4.6}$$

Thus the BF algorithm is identical to a simple axial wavenumber weighting or transform. Corresponding to the directivity angle limits of (180°, 0°) the axial wavenumber varies between the plane wave limits $-k/(1-M)$, $k/(1+M)$. Wavenumbers outside these limits have no associated physical angle.

In order to evaluate the liner attenuation along the pipe, we need to calculate the $PSD$ of the acoustic pressure excluding non-acoustic pressure due to hydrodynamic sources. In order to do so the following formulation was developed. The average mean square of Eq. 4.3 can be written as

$$< \hat{p}(\theta)\hat{p}^*(\theta) >= \frac{1}{N}\sum_{l=0}^{N-1}\sum_{m=0}^{N-1} w^*(\theta) < p(z_l, \omega)p(z_m, \omega) > w(\theta), \tag{4.7}$$

$$< \hat{p}(\theta)\hat{p}^*(\theta) >= \frac{1}{N}\sum_{l=0}^{N-1}\sum_{m=0}^{N-1} w^*(\theta)CSD(z_l, z_m)w(\theta), \tag{4.8}$$

where $PSD(\theta)$ is the spectral density of the BF pressure response and $CSD(z_l, z_m)$ is the cross-spectral density between each pair of monitor points at the axial position $(z_l, z_m)$.

In the previous chapter the inflow conditions have been manipulated in order to reduce the noise for mode zero, see Paragraph 4.2. Therefore it is useful to study the pressure field for higher azimuthal modes since their acoustic content is greater than for mode zero. An axial wavenumber analysis of pipe pressure is performed for different radial position in order to investigate acoustic liner performance along the radial direction. First of all it is necessary to define a longitudinal array to sample the pressure field. The pipe length is 50 radii but as explained in Paragraph 4.2 the first $20 \sim 25$ radii are necessary to develop a fully turbulent pipe statistically consistent with the benchmark results from Wu and Moin [66]. Furthermore, the region within 45-50 radii is affected by the presence of boundary conditions (CBC) at the outlet. Therefore, the array can be placed in the second half of the pipe to sample data physically reliable excluding the last 5 radii. Figure 4.9 shows the pipe bulk velocity profile for three different axial positions. It is clear that the flow statistically converges after 25 radii.

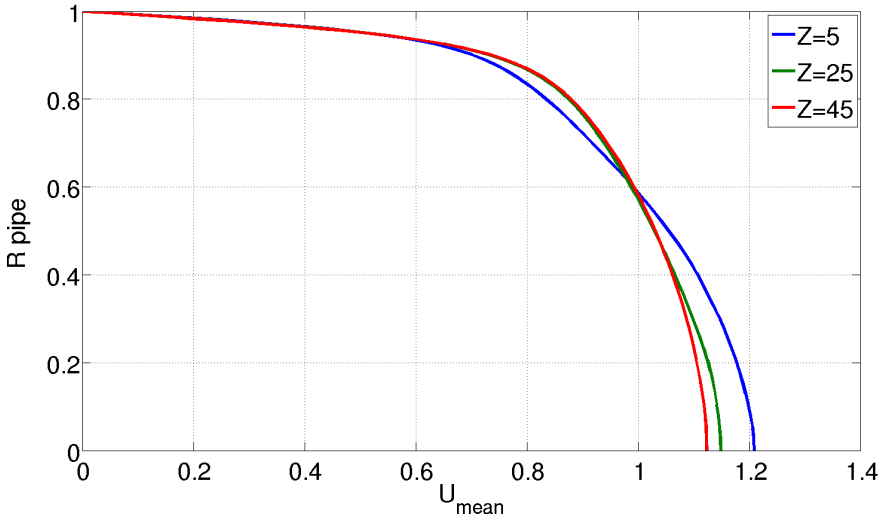


Figure 4.9: *Axial mean velocity profile for three different axial positions.*

The axial array consists of 130 grid points from the axial position $z = 25$ radii. Furthermore, 8 axial arrays are placed along the radial direction equally spaced, say, $\Delta r = 0.125$. Figure 4.10 shows a sketch of the array set up. In order to compute the $PSD$ of the pressure field $30,000$ time samples are considered.

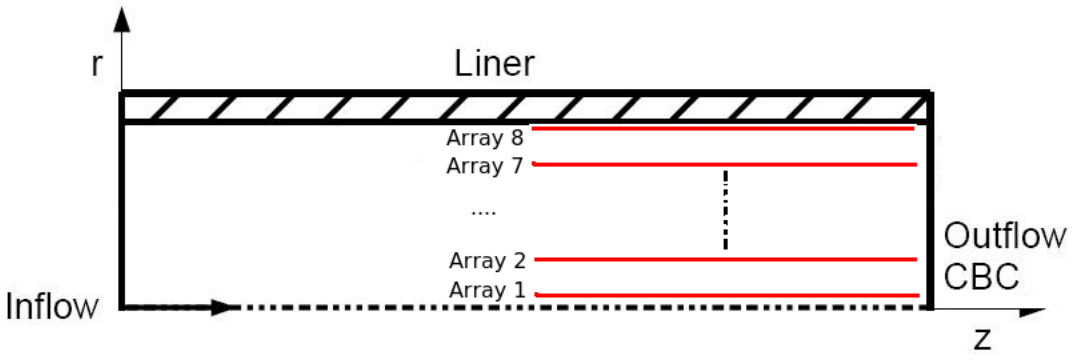


Figure 4.10: *Sketch of array distribution in the radial direction.*

Figure 4.11 shows the $PSD$ of the pressure field for the hard-wall case (left side) and lined case (right case) of the azimuthal mode zero. Four radial positions are displayed; $Y^+ = 0, Y^+ = 15, Y^+ = 66, Y^+ = 156$. The other four arrays are omitted on this occasion. The radial position is defined in terms of $Y^+$ according to the classical definition, $Y^+ = \frac{Ur}{\nu}$, where $r$ is the radial coordinate, $U$ is the bulk velocity and $\nu$ is the local kinematic viscosity. In Figure 4.11 the axial wavenumber range $-1 < k_z < 1$ represents the acoustic field while $k_z = 1/M \simeq 2$ is the axial wavenumber at which the $PSD$ related to the turbulent peaks according to Corcos' hypothesis [37]. As for the hard wall case in Figure 4.11a (left side), the acoustic range, $-1 < k_z < 1$, is characterized by the first three radial modes for each radial position, $Y^+$, above the second cut on frequency (white line). The presence of acoustic energy at $k_z = 1$ shows the presence of acoustic waves travelling downstream. Most of the acoustic energy carried by the acoustic waves travelling downstream is assumed to be produced by the inflow condition. Figure 4.11a (left side) also shows the presence of acoustic waves travelling upstream, $k_z = -1$. It is assumed that these waves are produced at the pipe outlet. Although a zonal non-reflecting characteristic boundary condition (CBC) is applied at the outlet to avoid reflections, the CBC seems not to be efficient in dissipating outgoing acoustic waves for this test case. As expected the whole attenuation takes place above the cut-on frequency, and it seems to be very effective over a wide rage of frequency, say, $\alpha_{mn}\sqrt{(1-M^2)/(2\pi M)} < St < 4$. Figure 4.11b (right side) shows the PSD wavenumber spectrum when the liner is applied. The acoustic field in the range $-1 < k_z < 1$ is significantly attenuated while the turbulent part, $k_z = 1/M$, remains practically unchanged.

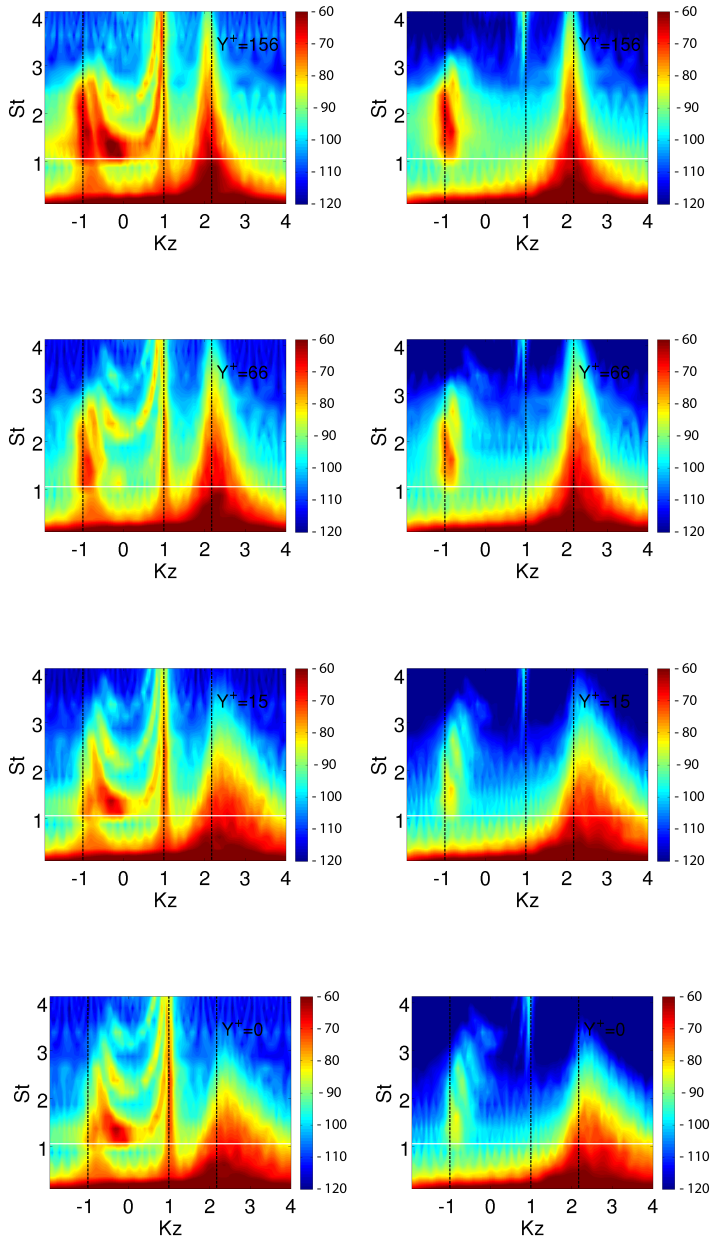


Figure 4.11: *Wavenumber-frequency domain, M*046*, mode 0. a) Hard-wall case. b) Lined-wall case.*

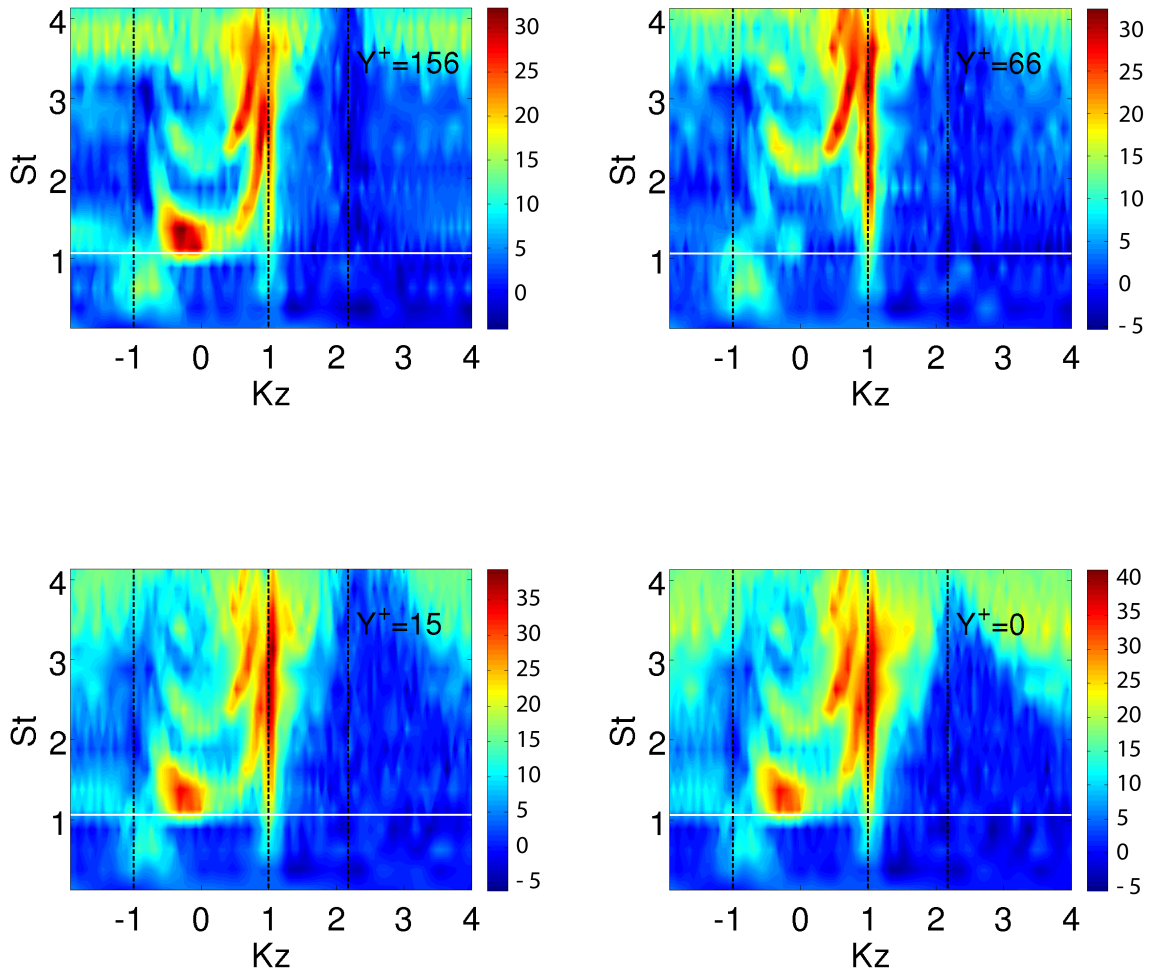


Figure 4.12: *Attenuation of mode 0 at four different radial positions,* $Y^+ = 156$, $Y^+ = 66$, $Y^+ = 15$, $Y^+ = 0$. *Test case* $M046$.

Apparently a part of the acoustic energy travelling upstream, $k_z = -1$ and $1.2 < St < 3$, does not disappear despite the presence of the liner. However, it seems to attenuate along the radial direction as we approach the wall. It is important to notice

that the BFM applied here has resolution limitations due to the finite array length. In principle the BFM requires an array with an infinite length in order to have a full resolution. In this application, since the domain size is finite, the array length is about 25 radii and the resolution in the wavenumber domain is limited. Figure 4.12 shows the acoustic attenuation for the four radial positions. As previously observed the acoustic waves travelling down stream are strongly attenuated. Figure 4.13a (left side) shows the $PSD$ of azimuthal mode 1 for the hard-wall case for four radial positions, $Y^+ = 0, Y^+ = 15, Y^+ = 66, Y^+ = 156$. In the acoustic range $-1 < k_z < 1$ the contour related to radial modes is visible as well as the peak related to the hydrodynamic energy at $1/M$. Figure 4.13b (right side) shows the $PSD$ when a liner is applied.

Similarly to mode zero, the liner model attenuates the acoustic field effectively. However, acoustic energy contained in upstream travelling waves remains, say, $k_z = -1$ and $1.5 < St < 2.5$ for every radial position in Figure 4.13b. Figure 4.14 shows the acoustic attenuation related to the mode 1 for each radial position. As expected, the radial modes are clearly attenuated. Waves travelling downstream are strongly attenuated in a wide range of frequency above the cut-on frequencies. As for the upward travelling wave attenuation, Figure 4.14 shows a modest attenuation in the wavenumber range $-1 < k_z < 1$ and $\alpha_{mn}\sqrt{(1-M^2)/(2\pi M)} < St < 2$.

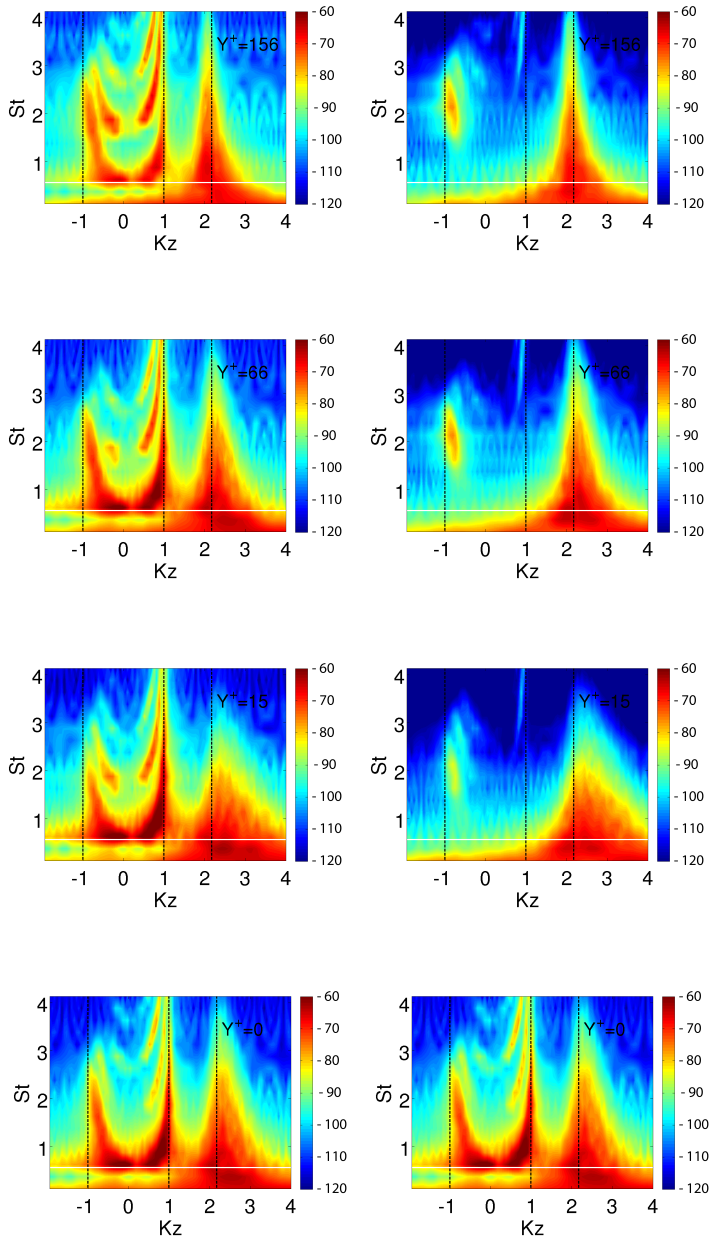


Figure 4.13: *Wavenumber-frequency domain, M*046*, azimuthal mode, m= 1. a) Hard-wall case. b) Lined-wall case.*

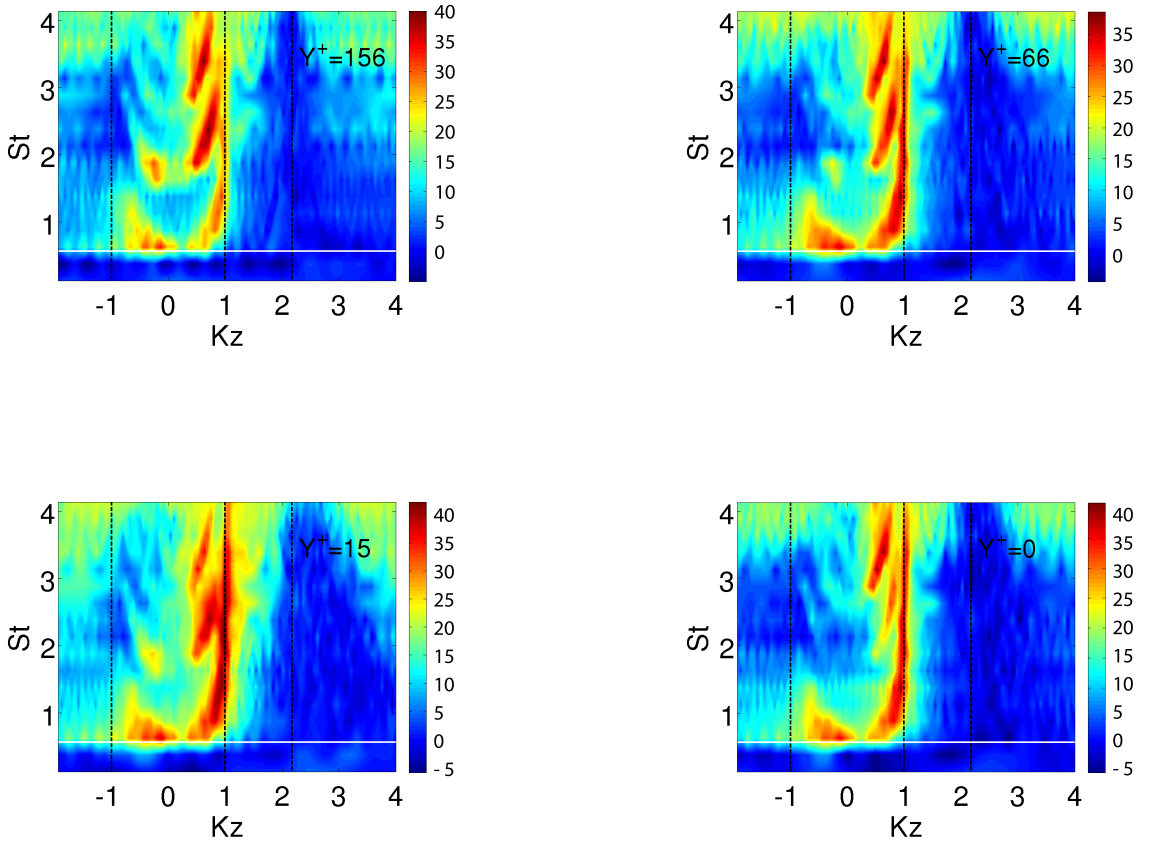


Figure 4.14: *Attenuation for mode 1 at four radial positions,* $Y^+ = 156$, $Y^+ = 66$, $Y^+ = 15$, $Y^+ = 0$. *Test case* $M046$.

As for higher azimuthal modes, Figure 4.15 shows the $PSD$ of azimuthal mode 2 at the wall position, $Y^+ = 0$. Figure 4.15a shows the azimuthal mode $m = 1$ for the hard-wall case. Acoustic waves travelling upstream are still present. The acoustic field is attenuated effectively above the cut on frequency when the liner is applied as shown in Figures 4.15b and 4.15c. Similar considerations can be carried out for the

wavenumber analysis of azimuthal mode 3 shown in the Figures 4.16.

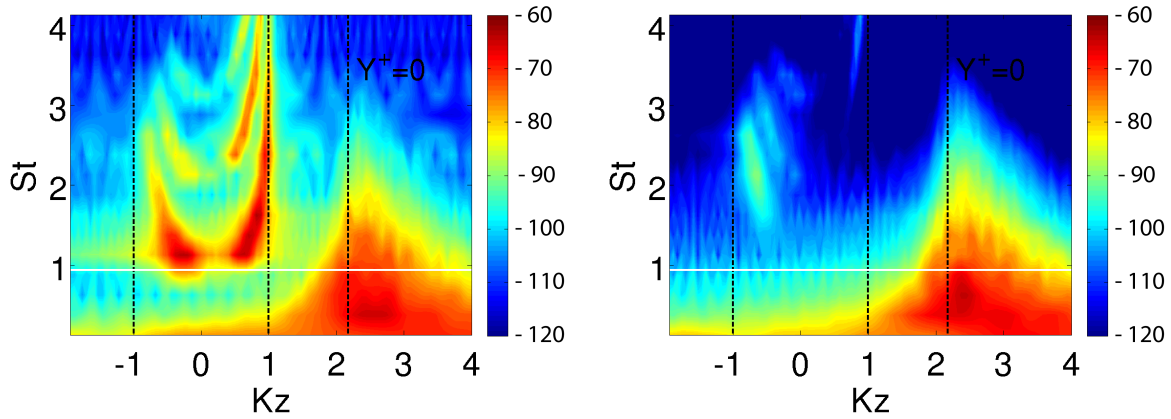


(a) (b)

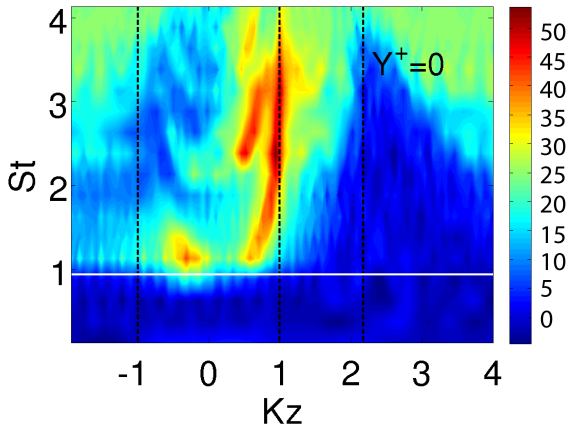


(c)

Figure 4.15: *Mode 2, test case M*046. *a) Hard-wall case. b) Lined case. c) Attenuation.*

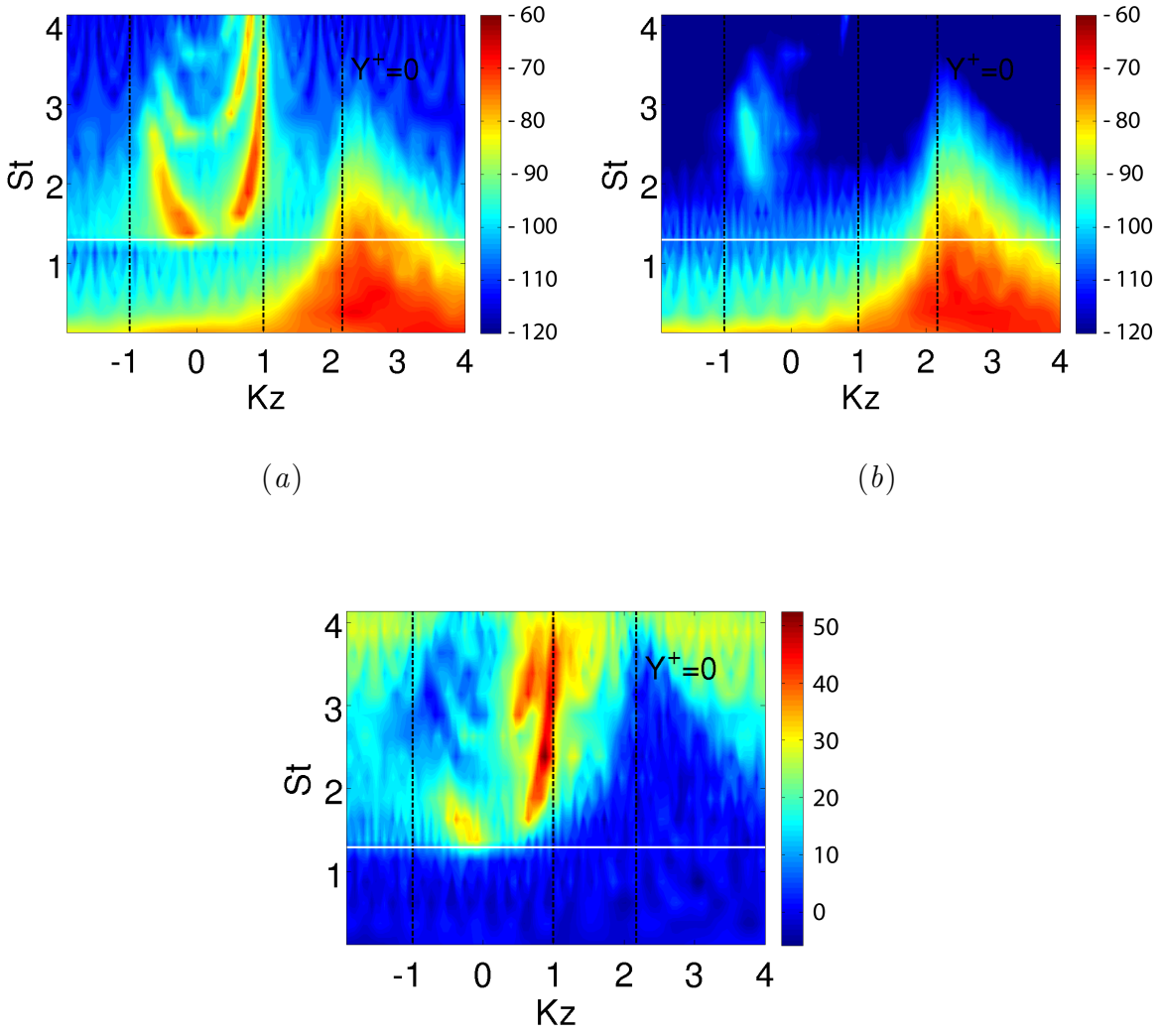


(a) (b)

(c)

Figure 4.16: *Mode 3, test case M*046. *a) Hard-wall case. b) Lined case. c) Attenuation.*

It is now possible to integrate the PSD of the pressure field in order to discriminate the acoustic field from the turbulent one for a certain frequency. In this case

$St_{resonance} = 1$ is chosen for the integration. Therefore, performing the integration of the PSD axial wavenumber spectrum over $-1 < k_z < 1$ and $k_z > 1/M$ it is possible to plot the trend of the acoustic and turbulent pressure spectrum over the wall distance $Y^+$, as shown in Figure 4.17. In Figure 4.17 the dashed and solid green lines represent the hydrodynamic components of the pressure field with and without the presence of the liner respectively. As expected, both hydrodynamic components match along the radial direction, $Y^+$. The dashed and solid blue lines represent the acoustic components of the pressure field with and without the presence of the liner respectively. When the liner is applied (dashed blue line) the acoustic field is reduced by $24dB$ along the radial direction. As observed previously the acoustic attenuation appears to be homogeneous.

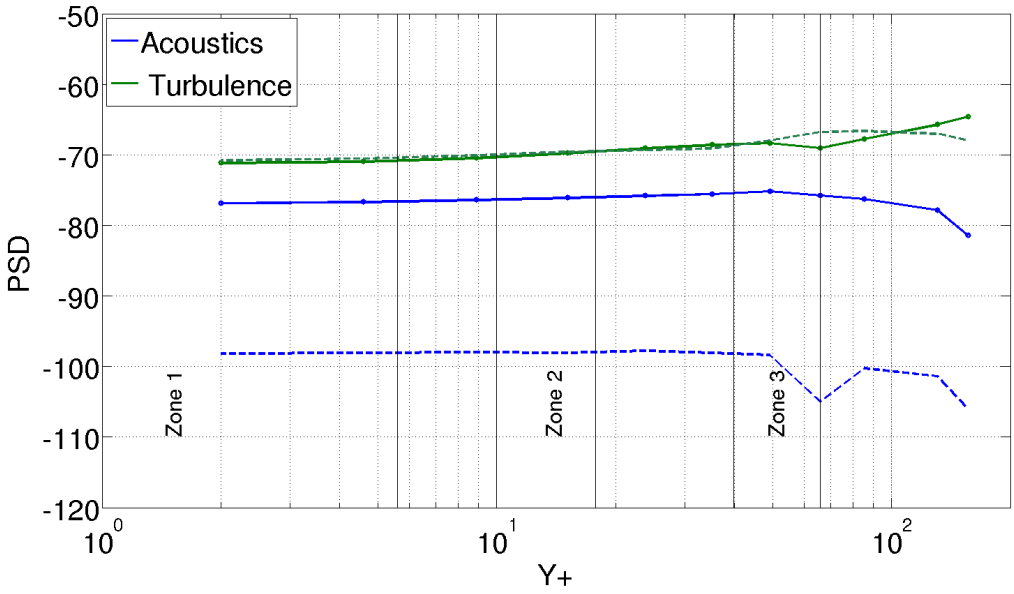


Figure 4.17: *PSD of hydrodynamic pressure versus PSD of acoustic pressure over radial coordinate, $Y^+$. Dashed lines lined case, solid lines hard-wall case.*

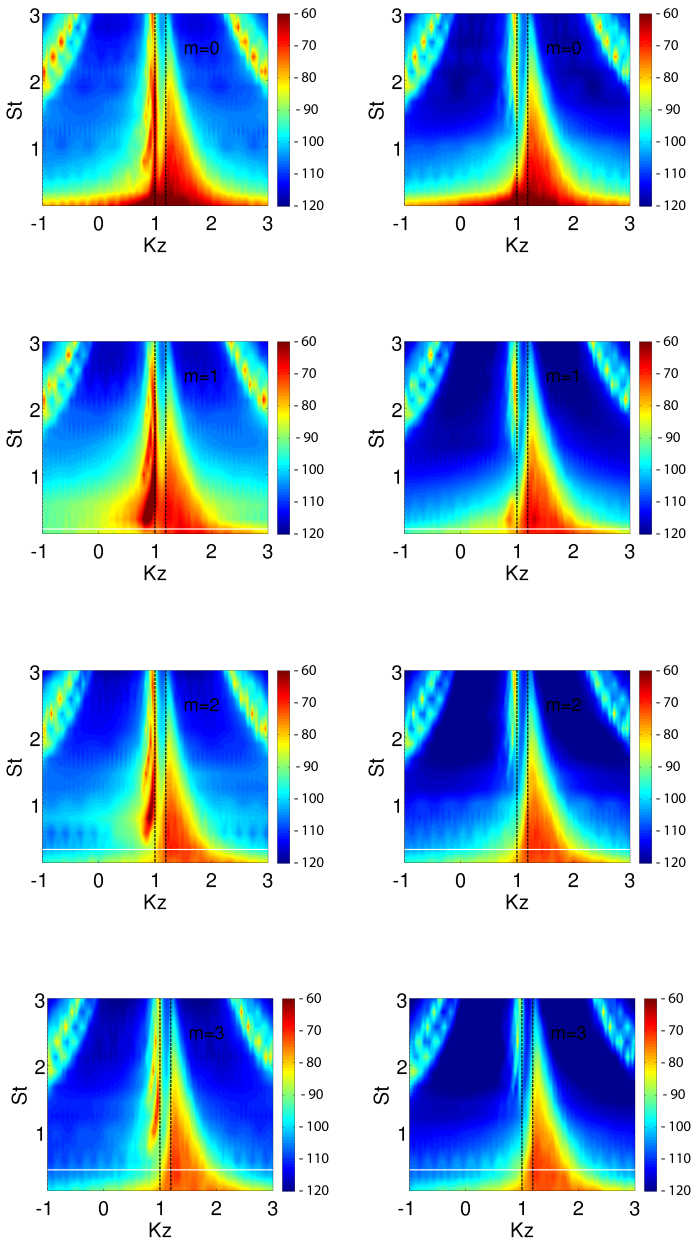


Figure 4.18: *M084 a) Azimuthal mode zero. b) Azimuthal mode 1. c) Azimuthal mode 2. d) Azimuthal mode 3.*

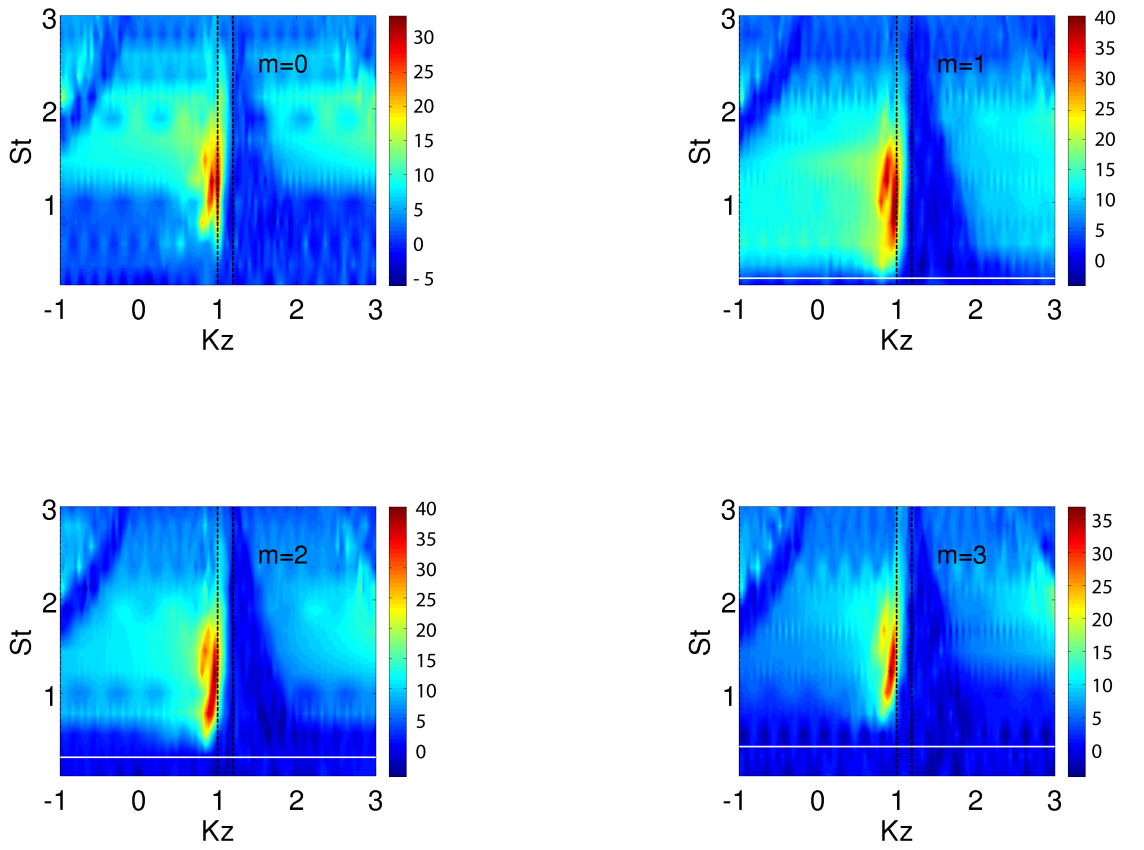


Figure 4.19: *Attenuation for modes m=0, 1, 2, 3 at the wall position,* $Y^+ = 0$. *Test case* $M084$.

A similar wavenumber analysis was carried out for the pipe case $M084$. Figure 4.18 shows the $PSD$ for the hard wall case (left side) and lined case (right side) for the modes m=0, 1, 2, 3 at the wall position, $Y^+ = 0$. In this test case only the downstream travelling waves appear in the acoustic range $-1 < k_z < 1$. The peak related to the hydrodynamic energy, $1/M$, tends to overlap with the downstream

travelling waves $k_z = 1$ due to the convection speed of $M = 0.84$ being close to the acoustic propagation speed. However, the liner attenuates the acoustic energy only. The contours that appear in the upper corners of Figure 4.19 are due to aliasing. As explained for the $M046$ test case, the BFM method has a limited resolution due to the finite length of the array used. The aliasing effect is more evident as the Mach number increases. Figure 4.19 shows the relative attenuation of each azimuthal mode. As expected the attenuation takes place above the cut on frequency. As explained previously, since the array with which the $PSD$ is calculated has a finite length and finite number of probes aliasing appears in the wavenumber-frequency plot. In the test case $M084$ aliasing is more evident because the Mach number is greater than in the $M046$ pipe case. Nevertheless, the attenuation of the acoustic component can still be reliably demonstrated.

## 4.4 Velocity field decomposition

As explained in Paragraph 2.9 the liner model interacts with the acoustic field through the normal-wall velocity component $v$. By applying the BFM to the $v$-velocity component field rather than pressure it is possible to decompose the acoustic part from the hydrodynamic part as previously computed for the pressure field. This will give us a better understanding on how the liner model interacts with the velocity field. Figure 4.20 shows the $PSD$ of the $v$ component field over the frequency-wavenumber domain for the hard-wall case (left-side) and lined case (right side) for four different radial positions. In the hard-wall case we can clearly see how the acoustic component, $-1 < k_z < 1$, tends to emerge as we approach the wall. Approaching the wall the

first three radial modes appear above the cut on frequency (white line) maintaining almost the same magnitude while the hydrodynamic energy magnitude tends to decrease. Integrating the $PSD$ of the acoustic and hydrodynamic component separately over $St_{resonanc} = 1$ it is possible to compare the trend between the two components over $Y^+$. Figure 4.21 shows the $PSD$ of the hydrodynamic component for the lined case (dashed green line) and the hard-wall case (solid green line). They both coincide over a wide range of $Y^+$. Approaching the wall the hydrodynamic component of the hard-wall case tends to $-\infty$ (zero in a linear case) while in the lined case the hydrodynamic component tends to a finite value. This is because of the liner model presence which allows the variation of $v$ component on the wall.

As we can see from Figure 4.21 in the lined case the acoustic component prevails over the hydrodynamic one in the vicinity of the wall $Y^+ < 11$. In theory also the hydrodynamic component in the lined case should tend to infinity when close to the wall. However, due to the fact that the array has a finite length the resolution over the wave domain is limited. This might cause a lack of accuracy in the results.

In conclusion, from the latest results we can learn that the acoustic component of the velocity field prevails over the hydrodynamic one in the vicinity of the wall when a liner is present. Therefore, the Tam and Auriault model affects the acoustic component only, leaving the hydrodynamic component unchanged.

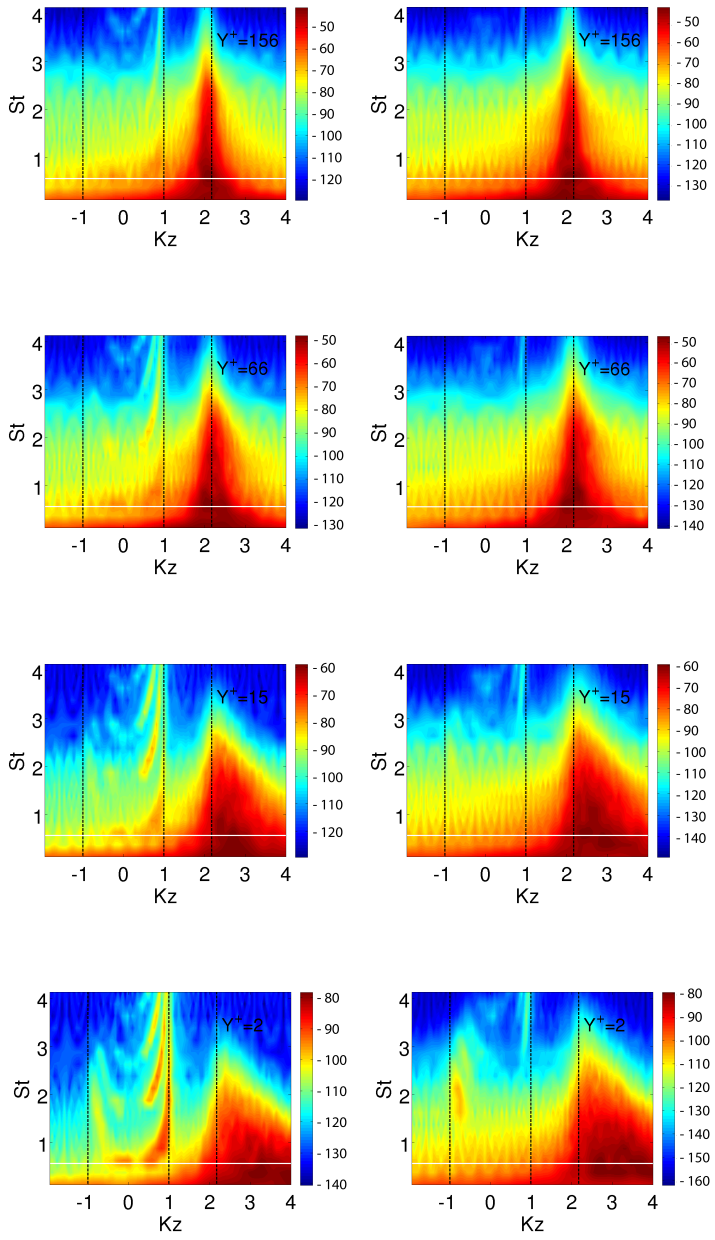


(a) (b)

Figure 4.20: *PSD of v component for different radial positions. Left side hard-wall case. Right side lined wall case.*

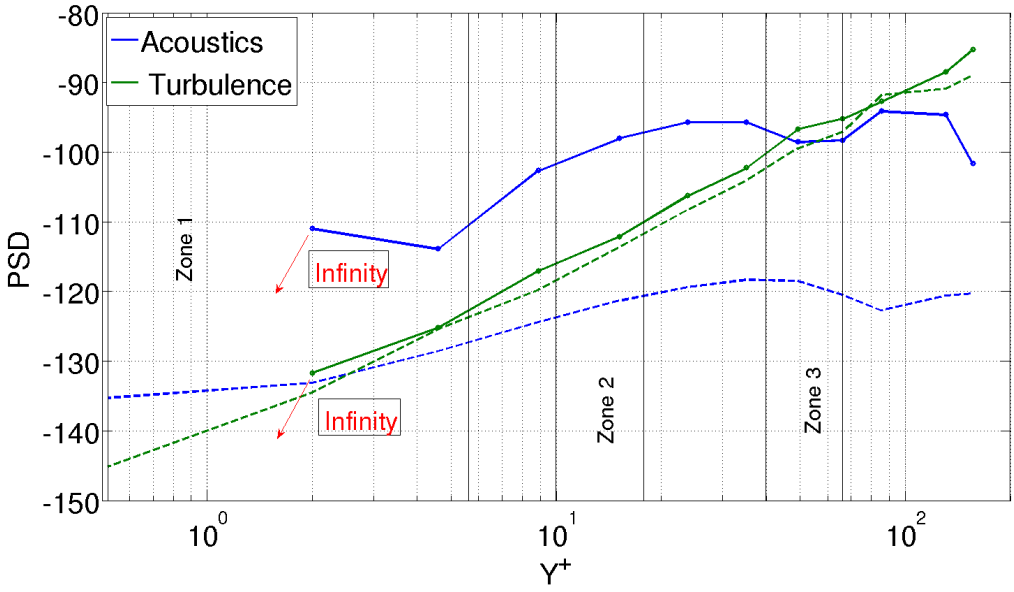


Figure 4.21: *PSD of v component over wall distance $Y^+$. Solid line: Hard-wall case. Dashed lined case. Blue colour: Hydrodynamic component. Green colour: acoustic component. The acoustic component prevails on the hydrodynamic component.*

# Chapter 5

# Jet noise prediction using the Ffowcs Williams-Hawkings method

In this chapter the Ffowcs Williams-Hawkings (FWH) method is presented. The FWH formulation will be studied as well as its numerical implementation for jet noise prediction. Furthermore, FWH method will be used to evaluate the effect of the acoustic liner model on the acoustic far field.

## 5.1 Acoustic analogies and hybrid approaches

The most popular methods to solve aeroacoustic problem are Direct Numerical Simulation (DNS) and hybrid approaches. In a DNS the Navier-Stokes equations are numerically solved without any turbulence model. This requires very high numerical resolution due to the large differences in the length scale present between the acoustic variables and the flow variables. It is computationally very demanding and unsuitable

for any commercial use. In the hybrid approach the computational domain is split into different regions, such that the governing acoustic or flow field can be solved with different equations and numerical techniques. This would involve using two different numerical solvers, first a dedicated Computational Fluid Dynamics (CFD) tool and secondly an acoustic solver. Typical CFD tools are DNS, explained above, and Large Eddy Simulation (LES)[82][88]. In an LES the smallest scales of the flow are removed through a filtering operation, and their effect modelled using subgrid scale models. This allows the largest and most important scales of the turbulence to be resolved, while greatly reducing the computational cost incurred by the smallest scales. This method is far cheaper than DNS. The flow field is then used to calculate the acoustic sources. These acoustic sources are provided to the second solver which calculates the acoustic propagation. Acoustic propagation can be calculated using integral methods which are multiple methods based on a known solution of the acoustic wave equation to compute the acoustic far field of a sound source. Because a general solution for wave propagation in free space can be written as an integral over all sources, these solutions are summarized as integral methods. The most common integral methods are the following

- Lighthill's analogy [70][71]
- Kirchhoff integral [74][75]
- Ffowcs Williams-Hawkings (FWH) [80]

When applying Lighthill's theory to the Navier-Stokes equations one obtains volumetric sources, whereas the other two analogies provide the far field information based on a

surface integral. The acoustic sources have to be known from some different source (*e.g.* a CFD simulation of the sources in a moving medium). The integral is taken over all sources at the retarded time (source time), which is the time at which the source sent out the signal, which arrives now at a given observer position. Common to all integral methods is that they cannot account for changes in the speed of sound or the average flow speed between source and observer position as they use a theoretical solution of the wave equation. Acoustic analogies can be very efficient and fast, as the known solution of the wave equation is used. The prediction of noise at a position far away from the source can be made as quickly as that for a position near the source. Common for the application of all analogies is the integration over a large number of contributions, which can lead to additional numerical problems (addition/subtraction of many large numbers with a result close to zero). Furthermore, when applying an integral method, usually the source domain is limited somehow. While in theory the sources outside have to be zero, the application can not always fulfil this condition. For some applications these errors even dominate the solution [89][90]. In the following sections more details concerning the integral methods mentioned above will be given. Particular emphasis will be given to Lighthill's analogy and the Ffowcs Williams-Hawkings method.

## 5.2 Lighthill's analogy

Lighthill [70][71] developed the acoustic analogy approach to calculate acoustic radiation from a relatively small region of turbulent flow embedded in an infinite homogeneous fluid in which the speed of sound $c_0$, the pressure $p_0$ and the density $\rho_0$ are constant. In the Lighthill formulation, the Navier-Stokes and continuity equations are

transformed to form an exact inhomogeneous wave equation whose source terms are important only within the turbulent region. Sound is imagined to be generated by a finite region of rotational flow in an unbounded fluid, see Figure 5.1. This avoids complications caused by the presence of the nozzle. Far away from the turbulent flow the formulation reduces to the homogeneous acoustic wave equation.

$$\frac{1}{c^2}\frac{\partial^2 \rho}{\partial t^2} - \nabla^2 \rho = 0 \tag{5.1}$$

Because the sound is a very small component of the whole motion its back-reaction on the mean flow can be usually ignored.

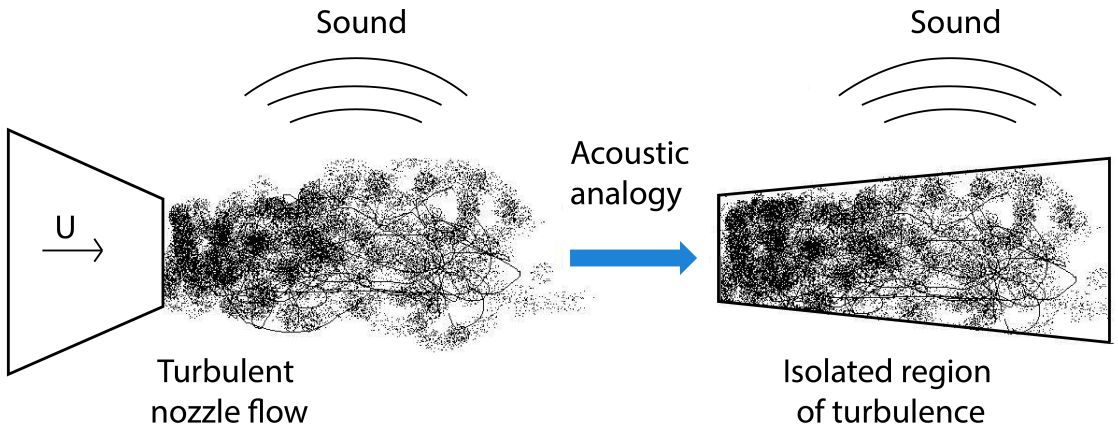


Figure 5.1: *The real flow field is modelled as a compact source region embedded in an infinite homogeneous fluid.*

In order to develop Lighthill's formulation we assume that the body forces are

negligible, therefore the momentum and continuity equations are

$$\rho\frac{\partial u_i}{\partial t} + \rho u_j\frac{\partial u_i}{\partial x_j} = -\frac{\partial}{\partial x_j}(p\delta_{ij} - \sigma_{ij}), \tag{5.2}$$

$$\frac{\partial \rho}{\partial t} + \frac{\partial(\rho u_j)}{\partial x_j} = 0, \tag{5.3}$$

where $u_i$ is the $i$th component of the velocity field, $\rho$ is the density, $p$ the pressure, $\delta_{ij}$ is the Kronecker delta and $\sigma_{ij}$ is the viscous stress tensor for a Stokesian fluid. Multiplying Eq. 5.3 by $u_i$, adding the results to Eq. 5.2 and combining terms yields

$$\frac{\partial \rho u_i}{\partial t} = -\frac{\partial}{\partial x_j}(\rho u_i v_j + p\delta_{ij} - \sigma_{ij}).$$

Adding and subtracting the term ${c_0}^2\partial\rho/\partial x_i$ results in

$$\frac{\partial \rho u_i}{\partial t} + {c_0}^2\frac{\partial \rho}{\partial x_j} = \frac{\partial T_{ij}}{\partial x_j}, \tag{5.4}$$

where

$$T_{ij} = \rho u_i u_j + \delta_{ij}[(p - p_0) - {c_0}^2(\rho - \rho_0)] - \sigma_{ij} \tag{5.5}$$

is the Lighthill turbulence stress tensor. We can now differentiate Eq. 5.3 with respect to $t$, take the divergence of Eq. 5.4 and subtract the results to obtain Lighthill's equation

$$\frac{1}{c^2}\frac{\partial^2 \rho}{\partial t^2} - \nabla^2\rho = \frac{\partial^2 T_{ij}}{\partial x_i \partial x_j}. \tag{5.6}$$

The quadrupole term $T_{ij}$ must be known in order to solve Eq. 5.6. In general $T_{ij}$ is defined using data from numerical simulation such as DNS. A knowledge of $T_{ij}$ is equivalent to solving the complete non-linear equations governing the flow, which is impossible for most flows.

Since no solid boundary is present in the flow, Eq. 5.6 can be solved in terms of the free-space Green's function, thus

$$\rho(\mathbf{x},t)-\rho_0=\int_\tau\int_v\frac{\partial^2}{\partial y_j\partial y_i}T_{ij}(\mathbf{y},\tau)G(\mathbf{x},t;\mathbf{y},\tau)dy\mathrm{d}\tau, \tag{5.7}$$

where

$$G(\mathbf{x},t;\mathbf{y},\tau)=\frac{\delta(t-\tau-\frac{|\mathbf{x}-\mathbf{y}|}{c})}{4\pi|\mathbf{x}-\mathbf{y}|}. \tag{5.8}$$

Thus Eq. 5.7 becomes

$$\rho(\mathbf{x},t)-\rho_0=\frac{1}{4\pi{c_0}^2}\frac{\partial^2}{\partial x_j\partial x_i}\int_v\frac{T_{ij}\left(\mathbf{y},t-\frac{|\mathbf{x}-\mathbf{v}|}{c}\right)}{|\mathbf{x}-\mathbf{y}|}dy, \tag{5.9}$$

where $\mathbf{x}$ is the position of the observer and $\mathbf{y}$ is the position of the source. If the distance between the observer point and any source point is large compared to the dimensions of the source region, a good approximation [70][73] of Eq. 5.7 is

$$\rho(\mathbf{x},t)-\rho_0\simeq\frac{1}{4\pi{c_0}^2}\frac{x_ix_j}{|\mathbf{x}|^3}\int_v\frac{\partial^2}{\partial\tau^2}T_{ij}\left(\mathbf{y},t-\frac{|\mathbf{x}-\mathbf{y}|}{c}\right)dy. \tag{5.10}$$

The advantage of this approximation is that the double spatial derivative is avoided. However, since a double time derivative appears in this formulation, the time resolution is important in order to obtain accurate results.

## 5.3 Kirchhoff integral

Kirchhoff [74][75] showed, that the radiation of sound from a limited source region can be described by enclosing this source region by a control surface called a Kirchhoff surface. The sound field inside or outside the surface, where no sources are allowed and

the wave operator on the left hand side applies, can be produced as a superposition of monopoles and dipoles on the surface. The theory follows directly from the wave equation. The source strength of monopoles and dipoles on the surface can be calculated if the normal velocity (for monopoles) and the pressure (for dipoles) on the surface are known. A modification of the method even allows calculation of the pressure on the surface based on the normal velocity only. The Kirchhoff integral method finds application in boundary element methods (BEM). A non-zero flow velocity is accounted for by considering a moving frame of reference with the outer flow speed, in which the acoustic wave propagation takes place.

## 5.4 Ffowcs Williams-Hawkings Method

Let $f(\mathbf{x}) = 0$ be a surface enclosing the turbulent region which is the noise generating region of the flow in this case. $f(\mathbf{x}) = 0$ will be called the control surface. We assume that the control surface has the following properties:

$$f(\mathbf{x}) > 0, \text{in the exterior of the control surface}$$

$$f(\mathbf{x}) < 0, \text{in the interior of the control surface}$$

Furthermore, we assume that $f(\mathbf{x}) = 0$ is defined such that $\nabla f = n$, where $n$ is the outward unit normal vector. Since the control surface is just a mathematical surface where data relative to the turbulent region are stored, we assume that the surface is permeable. This assumption allows us to obtain a convective wave equation in

unbounded space. In this way the solution of the wave equation is the simple Green's function in unbounded space.

An artificial discontinuity in all flow parameters across the control surface has now been introduced. Therefore, all parameters are considered as generalized functions and the conservation laws are defined in terms of generalized derivatives. The continuity and conservation of momentum equations are:

$$\frac{\partial \rho}{\partial t} + U_{0l}\frac{\partial \rho}{\partial x_l} + \frac{\partial}{\partial x_i}(\rho u_i) = 0, \tag{5.11}$$

$$\frac{\partial}{\partial t}(\rho u_i) + U_{0l}\frac{\partial}{\partial x_l}(\rho u_i) + \frac{\partial}{\partial x_j}(\rho u_i u_j + P_{ij}) = 0, \tag{5.12}$$

where $\rho$ is the fluid density, $\rho u_i$ is the component of fluid momentum and $P_{ij}$ is the compressive stress tensor as defined by Lighthill [70], and $U_{ol}$ is a generic velocity component of the coflow. Eq. 5.11 and 5.12 are written in the conservative form to avoid the problem of multiplication of generalized functions. The vector components $\rho u_i$ and $\rho u_i u_j$ are defined as unique generalized functions. Let us now apply the rules of generalized differentiation to the equations Eq. 5.11 and Eq. 5.12 to see how the artificial discontinuity across $f(\mathbf{x}) = 0$ changes the conservation laws. A bar over the symbol of derivative is use to indicate a generalized derivative. In the case of the continuity equation:

$$\begin{aligned}\frac{\bar{\partial}\rho}{\partial t} + U_{0l}\frac{\bar{\partial}}{\partial x_l}(\rho u_i) + \frac{\bar{\partial}}{\partial x_i}(\rho u_i) &= \frac{\partial \rho}{\partial t} + U_{0l}\frac{\partial \rho}{\partial x_l} + U_{0l}(\rho - \rho_0)\frac{\partial f}{\partial x_l}\delta(f) \\ &\quad + \frac{\partial}{\partial x_i}(\rho u_i) + [(\rho_0 U_{0i} + \rho u_i) - \rho_0 U_{0i}]\frac{\partial f}{\partial x_i}\delta(f) \\ &= [\rho(U_{0n} + u_n) - \rho_0 U_{0n}]\delta(f),\end{aligned} \tag{5.13}$$

where $u_n = u_i n_i$ is the local fluid velocity in the direction normal to the control surface, $n_i = \frac{\partial f}{\partial x_i}$ is the component of the unit outward normal to $f(\mathbf{x}) = 0$, $\rho_0 U_{i0}$ is the momentum of the fluid outside the control surface. Note, that the first, the second and the fourth term on the right hand side are zero because of Eq. 5.11. Similarly, we can derive the momentum equation in terms of generalized derivatives as

$$\begin{aligned}\frac{\bar{\partial}}{\partial t}(\rho u_i)+U_{0l}\frac{\bar{\partial}}{\partial x_l}(\rho u_i) + \frac{\bar{\partial}}{\partial x_j}(\rho u_i u_j + P_{ij}) = \frac{\partial}{\partial t}(\rho u_i) + U_{0l}\frac{\partial}{\partial x_l}(\rho u_i)+ \\ U_{0l}[(\rho_0 U_{i0} + \rho u_i) - \rho u_i]\frac{\partial f}{\partial x_l}\delta(f)+ \\ \frac{\partial}{\partial x_j}(u_i u_j + P_{ij}) + [\Delta P_{ij} + (\rho_0 u_i u_j + \rho_0 U_{i0} U_{j0}) - \rho_0 U_{i0} U_{j0}]\frac{\partial f}{\partial x_j}\delta(f) \\ = [\rho u_i (U_{0n} + u_n) + \Delta P_{ij} n_j].\end{aligned} \tag{5.14}$$

The next step follows exactly Lighthill's derivation of the jet noise equation, except that all new derivatives taken are generalized derivatives. First, take $\frac{\bar{\partial}}{\partial t}$ of both side of Eq. 5.11, then $\frac{\bar{\partial}}{\partial x_i}$ of both sides of Eq. 5.12. The last step is to subtract Eq. 5.14 from Eq. 5.13 and then $\nabla^2[c^2(\rho - \rho_0)]$ from both sides of the resulting equations. In this way we obtain the Ffowcs Williams-Hawkings equation for a permeable control surface. Using $p$ for $c^2(\rho - \rho_0)$, the equation is

$$\begin{aligned}\frac{D^2}{Dt^2}p(\mathbf{x},t) = \frac{D}{Dt}\{[\rho(U_{0n} + u_n) - \rho_0 U_{0n}]\delta(f)\} \\ - \frac{\partial}{\partial x_i}[\rho u_i (U_{0n} + u_n) + \Delta P_{ij} n_j]\delta(f) \\ + \frac{\bar{\partial}^2}{\partial x_i \partial x_j}[T_{ij} H(f)],\end{aligned} \tag{5.15}$$

where $T_{ij} = \rho u_i (u_n + U_{0n}) + \Delta P_{ij} - c^2 \rho \delta_{ij}$ is the Lighthill stress tensor. Since $T_{ij} = 0$ outside the control surface, the Heaviside function $H(f)$ in the last term on the right hand side is used. In general, the viscous term in $\Delta P_{ij}$ is a negligible source of sound

and we can assume that $\Delta P_{ij} = (p - p_0)\delta_{ij}$. In Eq. 5.15, the source terms on the right-hand side are defined respectively as monopole, dipole and quadrupole.

### 5.4.1 Observations

In Eq. 5.15, we can see that the artificial discontinuity at $f(\mathbf{x}) = 0$ has introduced a source term on the right-hand side of the continuity equation that is proportional to the local rate of mass injection into the exterior domain. The quadrupole term $\frac{\bar{\partial}^2}{\partial x_i \partial x_j}[T_{ij}H(f)]$ in Eq. 5.15 models the non-linearities in the turbulent field enclosed inside the control surface.

The FWH equation we have obtained is the governing equation for computation of noise outside the control surface. The parameters such as $\rho$, $\rho u_i$ and $p$ on the control surface and $T_{ij}$ must be known. These parameters are obtained from a CFD computation.

The Ffowcs Williams-Hawkings method was originally developed considering a solid surface embedded in a turbulent flow. When both the solid surface and the turbulence are compact relative to the radiated length scales, the turbulence is acoustically equivalent to a volume distribution of quadrupoles and a surface distribution of dipoles and monopoles. In air frame noise applications, the above mentioned distributions are known as turbulence noise source, loading noise source and thickness noise source respectively; however this interpretation is meaningful only when the FWH surface corresponds to a solid surface which represents a discontinuity in the flow field.

In order to simplify the integration of the Ffowcs Williams-Hawkings equation, the surface is considered permeable. In this way the FWH equation is valid in the entire

three-dimensional space so that the simple Green's function of the wave equation in unbounded space can be used. The assumption that the surface is permeable, makes the FWH method applicable to a jet case because it is possible to define a permeable surface embedding the turbulent field. Unlike the case of airframe noise, in a jet case the FWH surface does not correspond to a surface of discontinuity because the entire flow field is considered continuous. Therefore the dipole and monopole distributions cannot be considered as physical sources of sound. These distributions have the form of a monopole and dipole only from a mathematical point of view but they do not have a physical meaning.

## 5.5 Integral formulation

The FWH equation we have obtained is an inhomogeneous wave equation in a three-dimensional unbounded space. Hence, an integral representation can be found using the free-space Green's function defined as

$$G(\mathbf{x},t;\mathbf{y},\tau) = \frac{\delta(t-\tau-\frac{|\mathbf{x}-\mathbf{y}|}{c})}{4\pi|\mathbf{x}-\mathbf{y}|}, \tag{5.16}$$

where $\mathbf{x}$ is the position of the observer, $\mathbf{y}$ is the position of a general source inside and on the control surface, and $c$ is the speed of sound away from the control surface. In order to make the formulation more compact, let us define $g = \delta(t-\tau-\frac{|\mathbf{x}-\mathbf{y}|}{c})$ and $r = |\mathbf{x}-\mathbf{y}|$. As for the source terms, we define $Q(\mathbf{x},t) = \rho(u_n - U_{0n}) - \rho_0 U_{0n}+]\delta(f)$ and $L_i(\mathbf{x},t) = [\Delta P_{ij} n_j + \rho u_i(u_n + U_{0n})]\delta(f)$. The integral representation of the FWH equation is

$$
\begin{aligned}
4\pi p(\mathbf{x},t) = & \int_{\tau}\int_{s} \frac{D}{D\tau}\left[Q(\mathbf{y},\tau)\delta(f)\right] G(\mathbf{x},t;\mathbf{y},\tau)dy\mathrm{d}\tau \\
& - \int_{\tau}\int_{s} \frac{\partial}{\partial y_i}\left[L_i(\mathbf{y},\tau)\delta(f)\right] G(\mathbf{x},t;\mathbf{y},\tau)dy\mathrm{d}\tau \\
& + \int_{\tau}\int_{v} \frac{\partial^2}{\partial y_j \partial y_i}\left[T_{ij}(\mathbf{y},\tau)H(f)\right] G(\mathbf{x},t;\mathbf{y},\tau)dy\mathrm{d}\tau.
\end{aligned} \tag{5.17}
$$

Applying the integration by part rule to the three terms on the right-hand side and considering that $\partial G(\mathbf{x},t;\mathbf{y},\tau)/\partial\tau = -\partial G(\mathbf{x},t;\mathbf{y},\tau)/\partial t$ and $\partial G(\mathbf{x},t;\mathbf{y},\tau)/\partial y_i = -\partial G(\mathbf{x},t;\mathbf{y},\tau)/\partial x_i$ Eq. 5.17 becomes

$$
\begin{aligned}
4\pi p(\mathbf{x},t) = & \frac{D}{Dt}\int_{\tau}\int_{s} Q(\mathbf{y},\tau)\delta(f)G(\mathbf{x},t;\mathbf{y},\tau)dy\mathrm{d}\tau \\
& - \frac{\partial}{\partial x_i}\int_{\tau}\int_{s} L_i(\mathbf{y},\tau)\delta(f)G(\mathbf{x},t;\mathbf{y},\tau)dy\mathrm{d}\tau \\
& + \frac{\partial^2}{\partial x_j \partial x_i}\int_{\tau}\int_{v} T_{ij}(\mathbf{y},\tau)H(f)G(\mathbf{x},t;\mathbf{y},\tau)dy\mathrm{d}\tau
\end{aligned} \tag{5.18}
$$

As shown previously in other research works on cold turbulent jets [40] [77], the quadrupole term in Eq. 5.18 can be omitted in the computation when all the turbulent field is located inside the control surface. In other words, when the control surface is located where the acoustic equations are satisfied the omission of the volume term in Eq. 5.18 does not alter substantially the accuracy of the noise prediction [77]. This assumption results in a significant reduction of computational costs. In the present work the FWH formulation is implemented without the quadrupole term. It should be clarified here that neglecting the quadrupole term in Eq. 5.18 does not

imply that the (most significant) quadrupole term of jet noise mixing is not accounted for. If the FWH surface is placed outside of the hydrodynamic source region, then all contribution of the jet noise source terms inside the volume are represented by the dipole and monopole terms on the surface.

In Eq. 5.18 a spatial derivative appears in the second term, but we can manipulate the terms on the right-hand side in order to obtain an equation without the spatial derivative. In this way we can have a formulation less computationally demanding. If we consider the following relationships

$$\frac{\partial}{\partial x_i}\left(\frac{\delta(g)}{r}\right) = -\frac{\delta'(g)}{cr}\hat{r}_i - \frac{\delta(g)}{r^2}\hat{r}_i,$$
$$\frac{\partial}{\partial t}\left(\frac{\delta(g)}{r}\right) = \frac{\delta'(g)}{r}\hat{r}_i,$$

we obtain the relationship

$$\frac{\partial}{\partial x_i}\left(\frac{\delta(g)}{r}\right) = -\left[\frac{1}{c}\frac{\partial}{\partial t}\left(\frac{\delta(g)}{r}\right) + \frac{\delta(g)}{r^2}\right]\hat{r}_i. \tag{5.19}$$

Applying Eq.5.18 to Eq. 5.19 we have

$$\begin{aligned} 4\pi p(\mathbf{x},t) \simeq & \frac{D}{Dt}\int_\tau\int_s Q(\mathbf{y},\tau)\delta(f)\frac{\delta(g)}{r}dy\mathrm{d}\tau \\ & + \int_\tau\int_s L_i(\mathbf{y},\tau)\delta(f)\left[\frac{1}{c}\frac{D}{Dt}\left(\frac{\delta(g)}{r}\right) + \frac{\delta(g)}{r^2}\right]\hat{r}_i dy\mathrm{d}\tau \\ & = \frac{1}{c}\frac{D}{Dt}\int_\tau\int_s \frac{\left[Q(\mathbf{y},\tau) + L_i(\mathbf{y},\tau)\hat{r}_i\right]\delta(f)\delta(g)}{r}dy\mathrm{d}\tau \\ & + \int_\tau\int_s \frac{L_i(\mathbf{y},\tau)\hat{r}_i\delta(f)\delta(g)}{r^2}dy\mathrm{d}\tau. \end{aligned} \tag{5.20}$$

Now we have to consider the sampling property of the delta function on the variable $f$ and the scaling property of the delta function on the variable $g$. The last property,

given any function $h(t)$ and $g(t)$, is defined as follows

$$\int_{-\infty}^{+\infty} h(\tau)\delta(g(\tau))d\tau = \sum_n \left[\frac{h(\tau)}{|\partial g/\partial\tau|}\right]_{\tau=\tau_n{}^*},$$

where $\tau_n{}^*$ is the nth root of $g$, *i.e.* $g(\tau_n{}^*) = 0$. This relationship may be proved in a straightforward way by changing the integration variable in $\int_{-\infty}^{+\infty} h(\tau)\delta(g(\tau))d\tau$. In our case $g = \delta(t - \tau - \frac{|\mathbf{x}-\mathbf{y}|}{c})$, hence

$$\frac{dg}{d\tau} = \frac{(x_i - y_i)}{|\mathbf{x}-\mathbf{y}|\, c}\frac{dy}{d\tau} - 1,$$

where $\frac{dy}{d\tau}$ is the velocity at which the source travels through the source field, and $\frac{(x_i-y_i)}{|\mathbf{x}-\mathbf{y}|c}\frac{dy}{d\tau}$ is the component of this source velocity in the direction of the observer divided by the speed of sound c. We will name it relative Mach number, $M_r$. Hence,

$$\frac{dg}{d\tau} = |1 - M_r|\,,$$

where $|1 - M_r|$ is defined as Doppler factor. This factor will appear in the formulation because sources move with a relative velocity $cM_r$ with respect to the observer. Applying the properties of the delta function mentioned above to Eq. 5.20 we obtain

$$\begin{aligned} 4\pi p(\mathbf{x},t) \simeq \frac{1}{c}\frac{D}{Dt}\int_{f=0}\left[\frac{Q + L_i\hat{r}_i}{r\,|1-M_r|}\right]_{\tau=\tau^*} dy \\ + \int_{f=0}\left[\frac{L_i\hat{r}_i}{r^2\,|1-M_r|}\right]_{\tau=\tau^*} dy, \end{aligned} \tag{5.21}$$

where the subscript $\tau^*$ implies that the integral is evaluated at the retarded time (time when the sound is emitted) that can be found as the root of the equation $t - \tau - |\mathbf{x}-\mathbf{y}|/c = 0$. In our case $\mathbf{y}$ is a function of the retarded time, $y = y(\tau)$, because the sources are moving with respect to the position of the observer. Thus, $t - \tau - |\mathbf{x} - \mathbf{y}(\tau)|/c = 0$. The integration is performed over the control surface $f = 0$.

## 5.6 On the advanced time approach

Unlike the retarded time approach, in an advanced time approach the computational time is considered as the emission time [69]. Therefore, at a given time the contributions from the integration domain are computed. At each computational time and for each element of the control surface, the time at which the corresponding acoustic signal will reach the observer is considered as advanced time. In other words, the advanced time is the time at which the observer begins to "record" the signal from the sources on the control surface. The total acoustic signal is finally built up in the observer time domain through a summation over all the computed contributions. The observer location at the advanced time is used to calculate the relative position between the observer and an element of the control surface. We can define the general advanced time equation as

$$t_{adv} = \tau + \left|\mathbf{x}(\tau) - \mathbf{y}(\tau)\right| / c, \tag{5.22}$$

where, $t_{adv}$ is the advanced time, $\tau$ is the source time and $c$ is the speed of sound. In a general case we can assume that the observer moves at the constant velocity $c\bar{M}_{ob}$. In this case Eq. (5.22) can be solved in $t_{adv}$ as

$$\begin{aligned} t_{adv} &= \tau + \frac{r_i M_{ob} \pm \sqrt{(r_i M_{obi})^2 + r^2(1 - M_{ob}^2)}}{c(1 - M_{ob}^2)} \\ &= \tau + \frac{r(t)}{c}\left(\frac{M_{obr} \pm \sqrt{M_{obr}^2 + 1 - M_{ob}^2}}{1 - M_{ob}^2}\right), \end{aligned} \tag{5.23}$$

where $r_i = x_i(t) - y_i(\tau)$ is the distance between the observer and the source location and $M_{obr} = \hat{r}_i M_{obi}$ is the observer Mach number in the radiation direction. According to the magnitude of $\bar{M}_{ob}$ Eq. 5.23 can have different forms as explained in detail by Casalino [83].

In our case the observer is fixed with respect to the control surface, $\bar{M}_{ob} = \bar{0}$, thus the advanced time equation is

$$t_{adv} = \tau + |\mathbf{x} - \mathbf{y}| / c = \tau + |\mathbf{r}| / c. \tag{5.24}$$

The distance between the observer and the source location $\mathbf{r}$ does not depend on the time, therefore, no Doppler effects appear in the formulation. This means that an equally spaced discretization of the source time domain corresponds to an equally spaced discretization of the observer time domain. This yields obvious simplifications in the advanced time approach [85]. The implementation of the advanced time approach dose not required a modification of the integrals in Eq. 5.21.

The advantage of using the advanced time approach is that only the pressure from the integration domain is shifted forward in time, while in the retarded time approach every variable such as density, velocity, and pressure is shifted backward in time. Therefore, the advanced time approach reduces the computational coasts.

## 5.7 Non-dimensional formulation

In order to generalize the FWH formulation Eq. 5.21 is made non-dimensional. The non-dimensional variables of Eq. 5.21 are defined as follows

$$\begin{aligned} t' &= t\frac{U_0}{R}, \qquad p' = \frac{p}{\rho_0 U_0^2}, \qquad r' = \frac{r}{R}, \qquad x' = \frac{x}{R}, \\ y' &= \frac{y}{R}, \qquad Q' = \frac{Q}{\rho_0 U_0}, \quad L' = \frac{L}{\rho_0 U_0}. \end{aligned} \tag{5.25}$$

In our case, we define $U_0$ and $\rho_0$ as the bulk velocity and density, respectively, at the outlet of the nozzle and $R$ as the radius of the outlet section of the nozzle. Substituting

the relationships Eq. 5.25 into Eq. 5.21 we have

$$\begin{aligned} 4\pi p'(\mathbf{x},t) \simeq M_j \frac{D}{Dt'} \int_{f=0} \left[ \frac{Q' + L'_i \hat{r_i}}{r' \left|1 - M_r\right|} \right]_{\tau=\tau^*} ds' \\ + \int_{f=0} \left[ \frac{L'_i \hat{r_i}}{r'^2 \left|1 - M_r\right|} \right]_{\tau=\tau^*} ds', \end{aligned} \tag{5.26}$$

where

$$\begin{aligned} Q' &= \frac{\rho'}{M_j} \left( \frac{M_{on}}{M_j} - u'_n \right) - \frac{M_{on}}{M_j^2}, \\ L'_i &= \rho' u'_i \left( \frac{M_{on}}{M_j} - u'_n \right) + \Delta P'_{ij} n_j. \end{aligned} \tag{5.27}$$

$M_j$ is the jet Mach number and $M_{on}$ is the ratio between the normal component of the coflow $U_{on}$ to the speed of sound $c$ in the exterior of the control surface. Now the retarded time is found from the non-dimensional equation $t - \tau - |\mathbf{x} - \mathbf{y}(\tau)| = 0$. From now on every equation is shown non-dimensional, but for simplicity the symbol " $'$ " will be omitted.

## 5.8 Numerical scheme: Mid-panel quadrature

If we apply the mid-panel quadrature to 5.27 we have

$$\begin{aligned} 4\pi p(x,t) \simeq M_j \frac{D}{Dt} \sum_{j=1}^{n} \left[ \frac{Q(y_j, t - r_j) + L_i(y_j, t - r_j) \hat{r_i}}{r_j \left|1 - M_r\right|_j} \right]_{\tau=\tau^*} \Delta s_j \\ + \sum_{j=1}^{n} \left[ \frac{L_i(y_j, t - r_j) \hat{r_i}}{{r_j}^2 \left|1 - M_r\right|_j} \right]_{\tau=\tau^*} \Delta s_j, \end{aligned} \tag{5.28}$$

with the surface $S$ divided into $N$ panels. The argument of the sum is evaluated at the center of each panel ($\mathbf{y_j}$). In this numerical scheme we assume that the integrands of Eq. 5.28 are constant in the center of the $j$th panel where the integrals are evaluated.

Note that the subscript $j$ used in this section is an index that refers to the $j$th panel. The subscript $\tau^*$ implies that integral is evaluated at the retarded time which is found as the root of the equation $t - \tau - |\mathbf{x} - \mathbf{y}(\tau)| = 0$. Because the strength of the sources $L_i$ and $Q$ is evaluated at the retarded time, temporal interpolation of the input data is required.

## 5.9 Control surface geometry assessment

Since the input data is available in cylindrical coordinates, the control surface of our analysis is cylindrical as well. A conical surface may be chosen but it would require a spatial interpolation of the data. More aspects concerning the choice of the control surface will be explained later. The control surface is shown in Figure 5.2 and Figure 5.3.

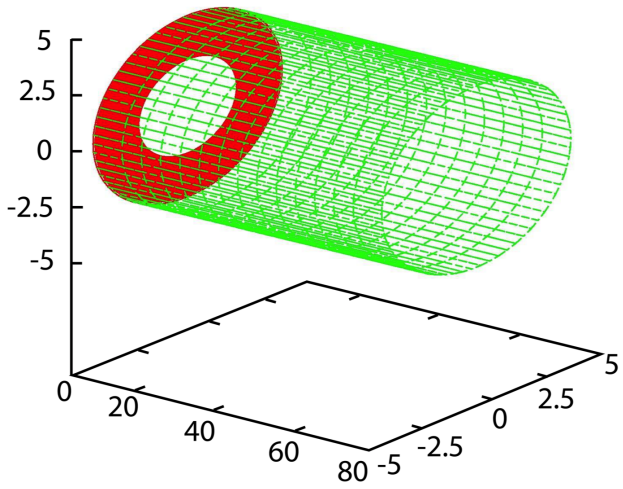


Figure 5.2: *Control surface for FWH integration.*

In the numerical scheme the control surface is not exactly a circular cylinder because its surface is divided into a number of flat panels. Therefore, the resulting geometric object is a cylinder with a polygonal base. Increasing the number of panels the surface of the cylinder with a polygonal base converges to the surface of a circular cylinder.

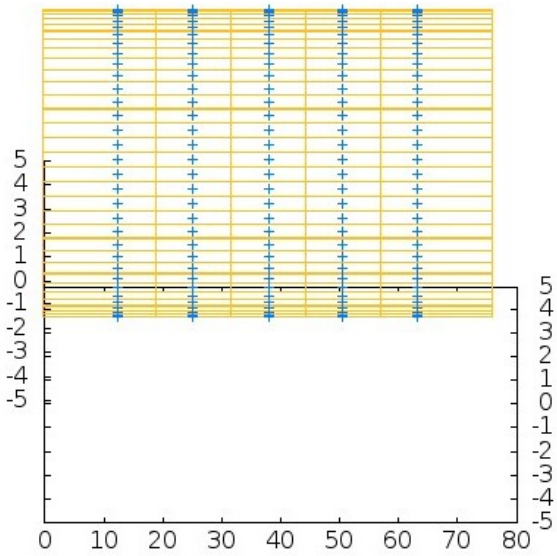


Figure 5.3: *Lateral surface; it is divided into a number of rectangular elements in the axial direction. The blue crosses are the control points.*

This is the problem of squaring the circle, therefore, the convergence is affected by the number of elements in the azimuthal direction only. If we define the percentage error related to the area of the surface of the cylinder with a polygonal base as

$$Error\% = 100 \cdot (S_{circular\ base} - S_{polygonal\ base})/S_{circular\ base}, \tag{5.29}$$

we can study its convergence as the number of elements in the azimuthal direction increases, see Figure 5.4. In other words we can study geometric errors related to the

control surface.

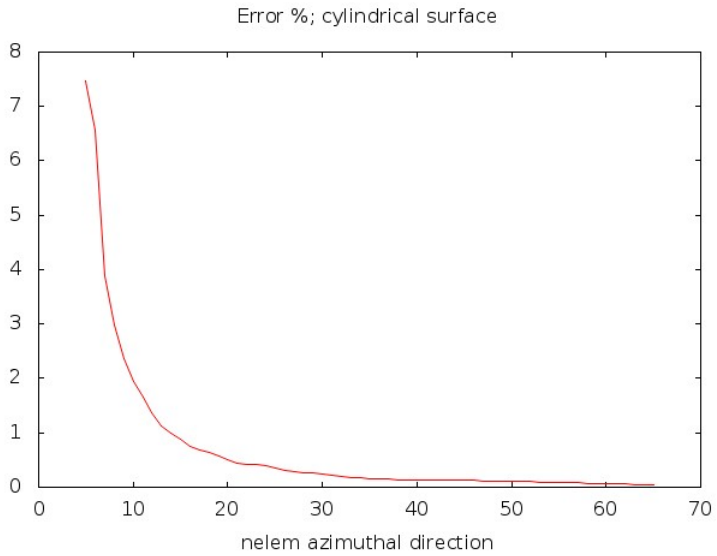


Figure 5.4: *Percentage error convergence; the geometric percentage error tends to zero as the number of elements (nelem) in the azimuthal direction increases.*

In Figure 5.4 the percentage error tends to zero quickly; after 35 elements we can assume that it is converged, whereas 66 elements in the azimuthal direction is the maximum amount available from DNS data. If we plot the convergence of the same function keeping the number of azimuthal elements fixed and increasing the number of elements in the longitudinal and radial direction we can see that it does not vary as the number of elements increases, see Figure 5.5. In Figure 5.5 the oscillations are due to numerical approximations. If we consider the percentage error convergence related to the volume of the cylinder we have a similar behaviour.

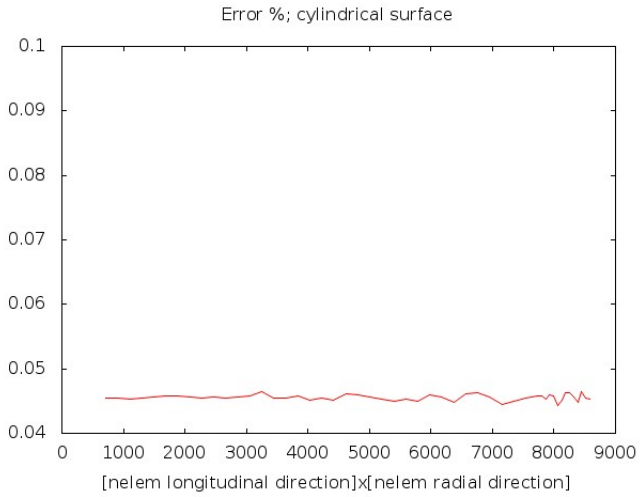


Figure 5.5: *Percentage error convergence; the geometric percentage error does not change as the number of elements in the longitudinal and radial direction increases.*

## 5.10 Verification of FWH code

In order to validate the FWH code a simple surface with four panels is used. Furthermore, the input variables are defined in term of trigonometric functions such that $\rho = A_1 \sin(\omega t)$, $u = A_2 \sin(\omega t)$, $v = A_3 \sin(\omega t)$,$w = A_4 \sin(\omega t)$. The acoustic pressure is calculated analytically using

$$4\pi p(t) = \sum_{j=1}^{4} \frac{\partial}{\partial x_i} \frac{L_{ij}}{|\mathbf{x}|} \Delta s_j + \sum_{j=1}^{4} \frac{D}{Dt} \frac{Q_j}{|\mathbf{x}|} \Delta s_j, \tag{5.30}$$

where $Q_i$ and $L_i$ are defined from Eq. 5.27. Setting $\omega = 0.2$, $r_{ob} = 3$, $\theta_{ob} = 90^\circ$ and the coflow $M_c = 0.2$ we can compare the analytical results with the results from the

FWH code as sketched in Figure 5.6. In Figure 5.7 another comparison is displayed. In this case $\theta_{ob} = 40°$ and a random component has been added in the input variable. The agreement between the FWH implementation and the analytical solution is very good.

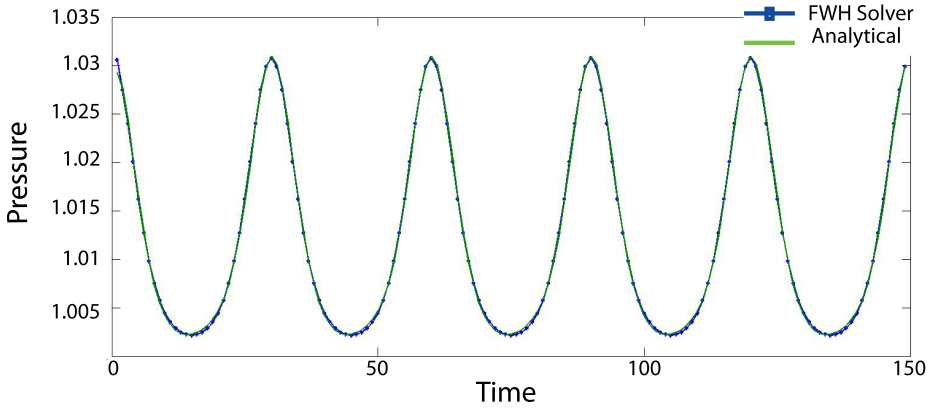


Figure 5.6: *Comparison between the analytical and numerical solution solution.*

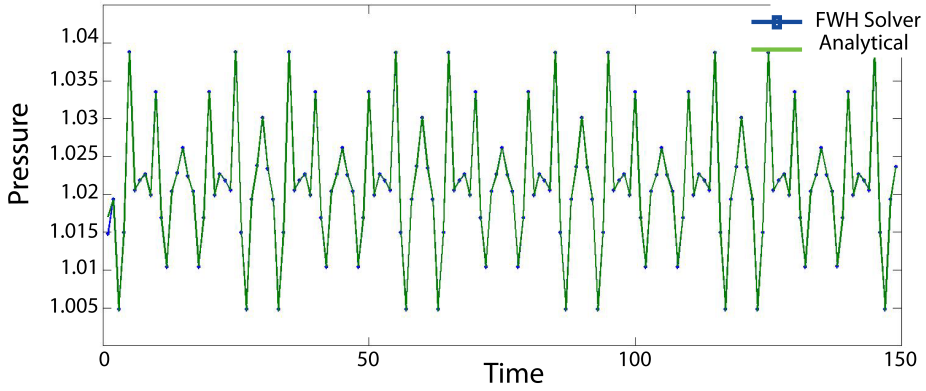


Figure 5.7: *Comparison between the analytical and numerical solution solution with a random component.*

## 5.11 Numerical implementation of the advanced time approach

In this section more details concerning the numerical implementation are presented. Let us consider a distribution of three point sources and an observation point as sketched in Figure 5.8. Each source emits an acoustic signal at the same time (source time) with the same wave length. The observer will record the acoustic signals from the point sources at the time $t_1 = r_1/c$, $t_2 = r_2/c$, $t_3 = r_3/c$ respectively, where $c$ is the speed of sound, $r_1$, $r_2$ and $r_3$ are the distances between the observer and each source. In order to obtain the total signal at the observer point each signal is shifted forward on the observer time scale by the advanced time $t_1$, $t_2$ and $t_3$ respectively. After this, each signal is linearly interpolated on the observer time scale and then summed, see Figure 5.9. Obviously as the observer location changes the advanced times $t_1$, $t_2$ and $t_3$ change as well, see Figure 5.10. This aspect is considered when Eq. 5.24 is implemented to make the numerical scheme as flexible as possible.

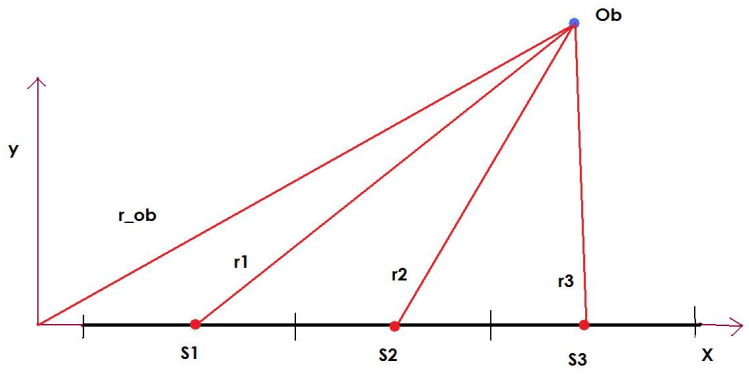


Figure 5.8: *Sketch of 3 point sources. The observation point (Ob) is in the far field.*

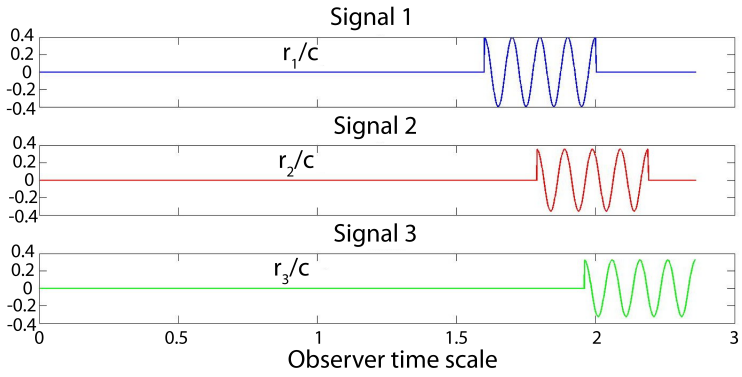


Figure 5.9: *Three signals recorded by the observer.*

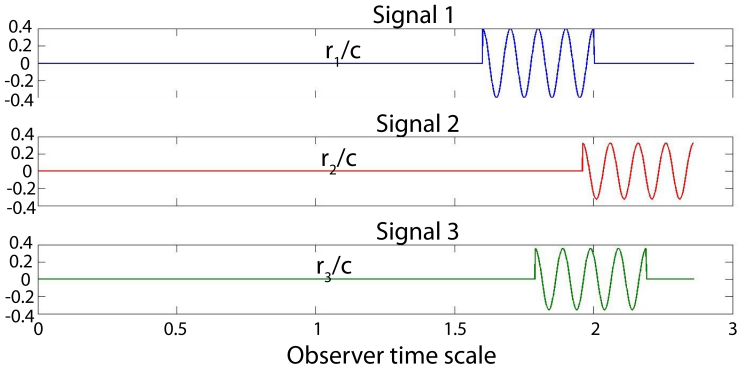


Figure 5.10: *Three signals recorded by the observer in a different position.*

## 5.12 Far field approximation applied to the advanced time approach

When the observation point is far way from the control surface, approximations in the numerical scheme might be applied. Let us consider just two point sources. If we move away the observation point extending the position vector $r_{ob}$, we can see that

the distances between the sources and the observation point $r_1$, $r_2$ converge to $r_{ob}$. Formally we can write

$$\lim_{r_{ob}\to\infty} r_1 = \lim_{r_{ob}\to\infty} r_2 = r_{ob},$$

thus

$$\lim_{r_{ob}\to\infty} r_1 - r_2 = 0. \tag{5.31}$$

It is important to notice that $r_{ob}$ is made non dimensional using a characteristic dimension of the control surface. The acoustic signals from each source tend to be shifted by the same advanced time as we extend the position vector $r_{ob}$. In other words, the acoustic signals align on the observer time scale as the observer point is moved away, as we can see in Figures 5.11 and 5.12.

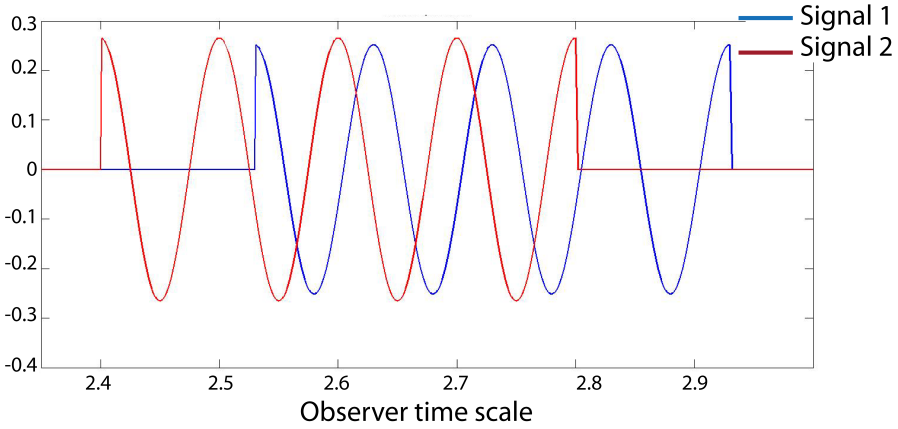


Figure 5.11: *Signals for* $r_{ob} = 3$.

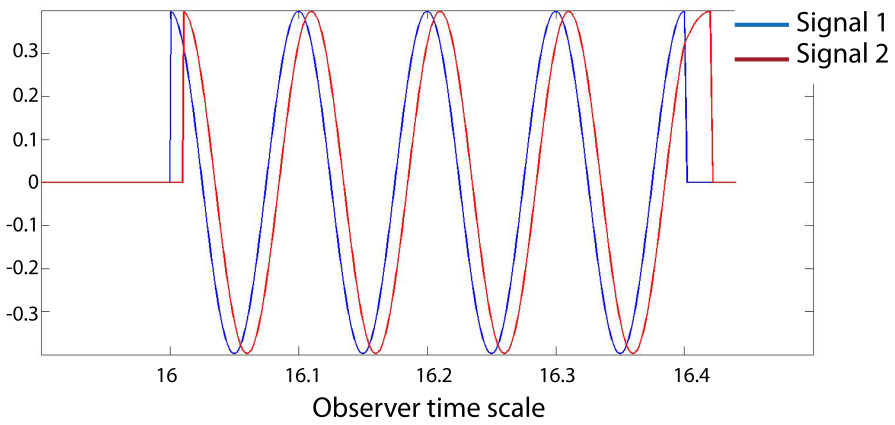


Figure 5.12: *Signals for $r_{ob} > 10$; The signals tend to align.*

From Eq. 5.31 we can define the function $r_1 - r_2 = f(r_{ob})$ with which we can quantify the tendency of the acoustic signals to align on the observer time scale. In the Figure 5.13 the function defined above is plotted. We can see that $r_1 - r_2 = f(r_{ob})$ tends to zero sharply. Therefore, when $r_{ob}$ is 10 times the length of the control surface, $r_1 - r_2$ has an order of magnitude of $O(10^{-2})$, which can be considered very small in this case. This is an important result because it allows us to avoid the linear interpolation when the observation point is sufficiently far away from the source field with a relevant reduction in the computational costs. In the following sections this approximation will be applied to the FWH method using DNS data to analyse its effect on the acoustic spectrum prediction.

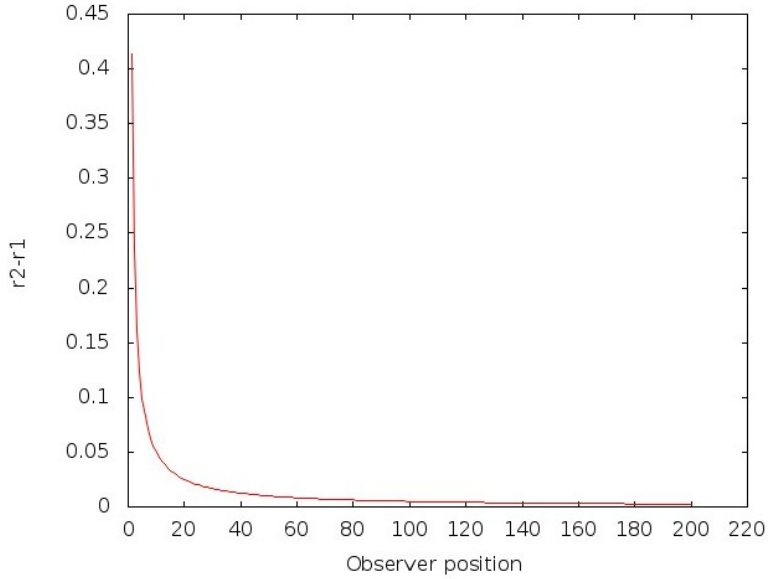


Figure 5.13: $r_1 - r_2 = f(r_{ob})$. *This function is plotted over the observer position* $r_{ob}$. *As the observer moves away from the control surface the difference* $r_1 - r_2$ *tends to zero.*

## 5.13 Jet test case; numerical set up and grid design

The computational domain comprises five blocks, as shown in Figure 5.14, which can be defined as: flow inside the pipe (block 1), jet development downstream of the pipe exit (blocks 2, 3 and 4), and co-flow and acoustic field upstream of the pipe exit (block 5). The sizes of each block, with the corresponding number of grid points and number of subdomains in the streamwise (z) and radial (r) directions, are given in Table 5.1. The numerical method for time and spatial discretization used to solve the compressible Navier-Stokes equations are the same as for the pipe test case, see Paragraph 3.2.

Downstream of the pipe exit, the physically useful part of the computational domain extended to $z = 79R_{pipe}$ followed by an outflow zone [56] with 180 grid points which extended up to $z = 110R_{pipe}$. In the streamwise direction the grid spacing is stretched from the minimum of $\Delta z = 0.009R_{pipe}$ at the pipe exit to $\Delta z = 0.01475R_{pipe}$ at $z = 10R_{pipe}$, and then further to $\Delta z = 0.0248R_{pipe}$ at $z = 20R_{pipe}$; the maximum grid spacing at $z = 79R_{pipe}$ is $\Delta z = 0.029R_{pipe}$. In the radial direction the grid spacing is kept equidistant across block 3 (thickness of the wall) with $\Delta r = 0.0026R_{pipe}$ and then was stretched to $\Delta r = 0.1421R_{pipe}$ at $r = 12.5R_{pipe}$; from $r = 12.5R_{pipe}$ to $r = 80.5R_{pipe}$ the grid spacing is again kept uniform. Finally in the upstream direction (block 5) the grid spacing is refined from $\Delta z = 0.1$ at the inflow boundary $z = 0$ to $\Delta z = 0.009R_{pipe}$ at the pipe exit ($z = 0$). In the azimuthal direction 64 Fourier modes are used resulting in $408 \times 10^6$ grid points.

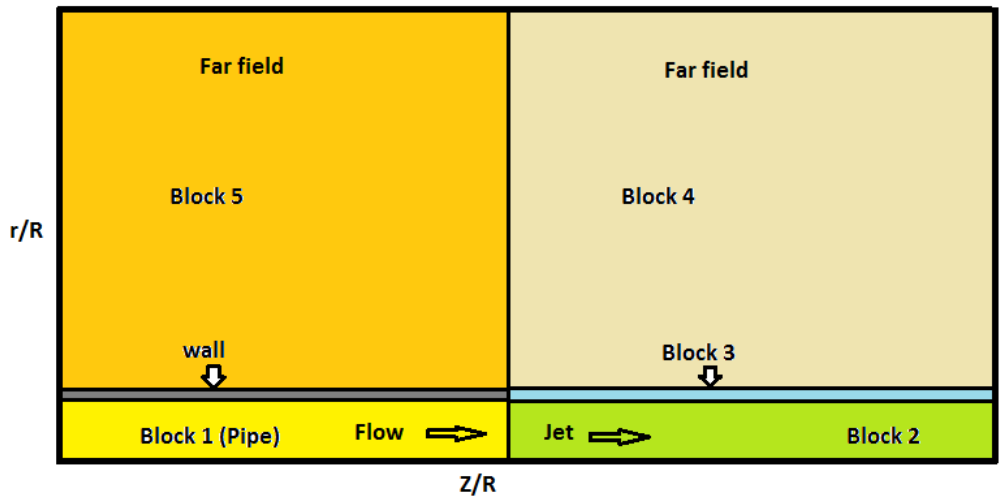


Figure 5.14: *Sketch of the computational flow domain.*

| Block No. | Block 1 | Block 2 | Block 3 | Block 4 | Block 5 |
|---|---|---|---|---|---|
| $L_z \times L_r$ | $50.0 \times 1.0$ | $110.0 \times 1.0$ | $110.0 \times 0.0416$ | $110.0 \times 79.5$ | $50.5 \times 79.5$ |
| $N_z \times N_r$ | $624 \times 68$ | $2808 \times 68$ | $2808 \times 17$ | $2808 \times 833$ | $624 \times 833$ |
| $N_{p_z} \times N_{p_r}$ | $48 \times 4$ | $216 \times 4$ | $216 \times 1$ | $216 \times 49$ | $48 \times 49$ |

Table 5.1: *Size (L), number of grid points (N) and the number of processors (Np) ) in the axial (z) and radial (r) directions. All dimensions are normalized with* $R_{pipe}$.

The design of the grid for the blocks 2, 3, 4, 5 is based on jet flow simulations by Sandberg et al. [27]. In order to confirm that all time scales of turbulence were fully resolved, the pressure power spectral density (PSD) was computed for locations within the hydrodynamic field. Sandberg et al. [27] showed that the PSD of pressure decays correctly over high frequencies. This suggests that the grid design is appropriate for the jet flows under examination. The maximum grid spacing away from the jet exit (in both streamwise and radial directions) is chosen to resolve acoustic waves up to Strouhal number $St_D = 2$ (based on the jet centreline velocity and diameter) with at least 10 grid points. The grid design for the pipe (block 1) has been already described in Section 3.5.

## 5.14 Monopole and dipole field assessment

In this section we will see how the input data are stored on the control surface. The jet flow is characterized by a jet Mach number, based on nozzle bulk velocity, $M_j = 0.84$ and a co-flow $M_{co} = 0.2$, with $R_e = 3500$. The $R_e$ is based on the bulk velocity at the

pipe exit and the pipe diameter. The simulation is run up to 1000 time units to achieve fully converged flow [27] with $\Delta t = 0.01$. In Figure 5.15, an example of the pressure field at the first available time-step is shown. Time is made non-dimensional using the bulk velocity and pipe radius. The FHW method requires the three components of the velocity $u$, $v$, $w$, the density and the pressure field to be known on the control surface.

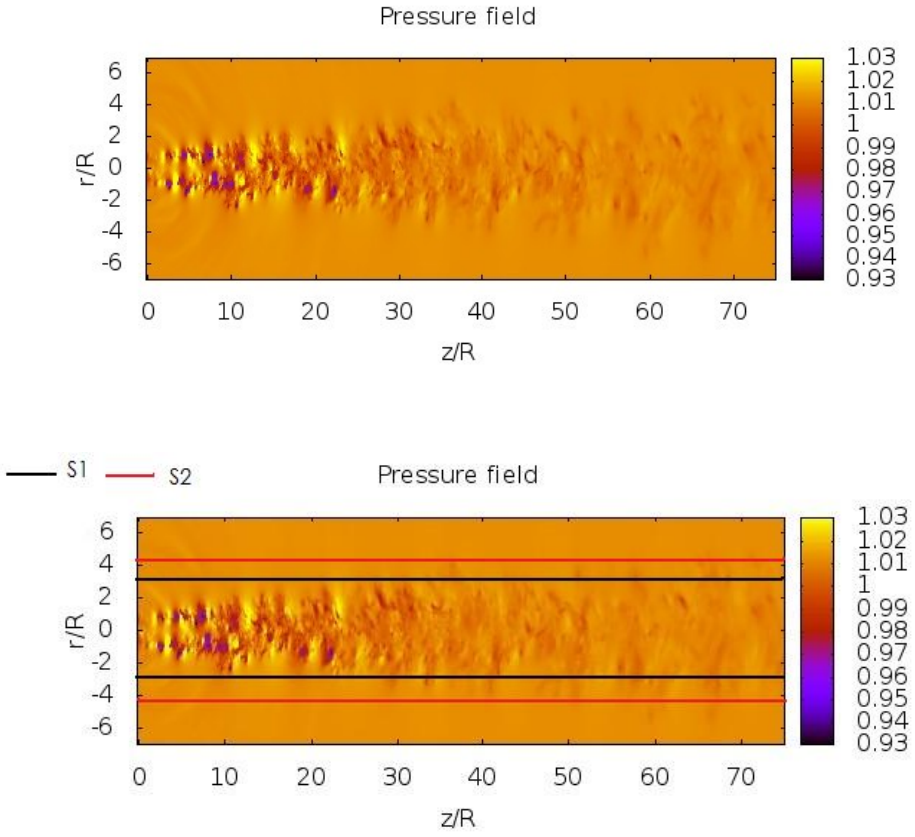


Figure 5.15: *Snapshot of the pressure field at the first time-step, $\phi = 0, 180°$. Two control surface, S1 with radius=3, S2 with radius= 4.5 (bottom).*

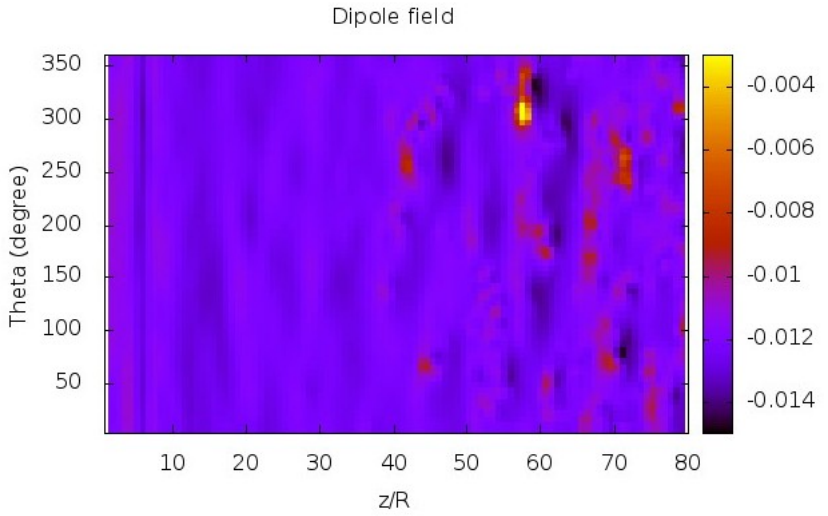


Figure 5.16: *Snapshot of the dipole field computed from Eq. 5.27 at the first time-step on the lateral surface; Radius=4.5.*

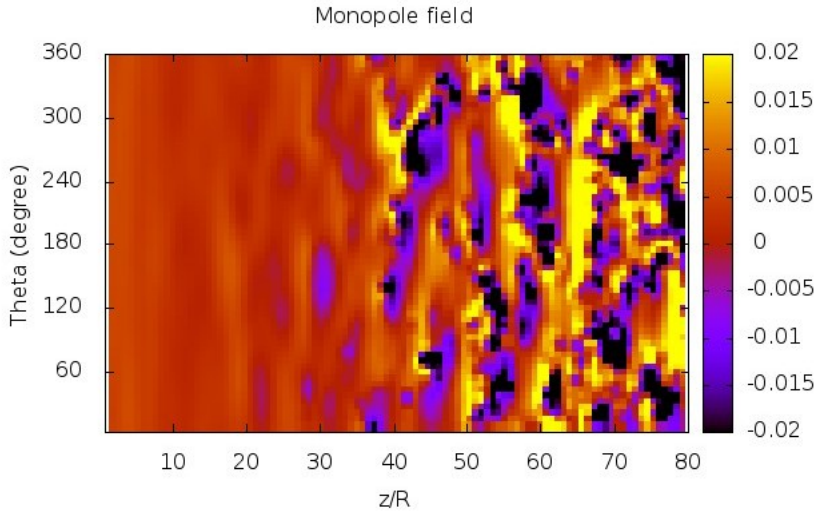


Figure 5.17: *Snapshot of the monopole field computed from Eq. 5.27 at the first time-step on the lateral surface; Radius=4.5.*

Once the radius and the length of the control surface is defined the data from the DNS simulation are stored at every time-step. In the following pictures, input data at the first time step are shown. With this data it is possible to calculate the dipole and monopole distribution using Eq. 5.27. If we divide the control surface into 8000 elements we obtain the monopole and dipole fields as shown in Figure 5.16 and 5.17.

## 5.15 Numerical scheme assessment

The main focus of this section is to show the behaviour of the convergence of the numerical scheme over parameters such as control surface dimensions and number of elements. In particular, the convergence of the first and second integrals in Eq. 5.28 will be studied.

Before proceeding further, it is important to make sure that the numerical scheme converges as the number of elements on the control surface increases. Once the length and the radius of the cylinder are fixed at the first time-step, the convergence of the first and second integrals in Eq. 5.28 is shown in Figures 5.18 and 5.19. Both integrals can be considered converged at 8000 elements. This is the number of elements that will be used on the control surface for far field noise prediction presented in the following paragraphs.

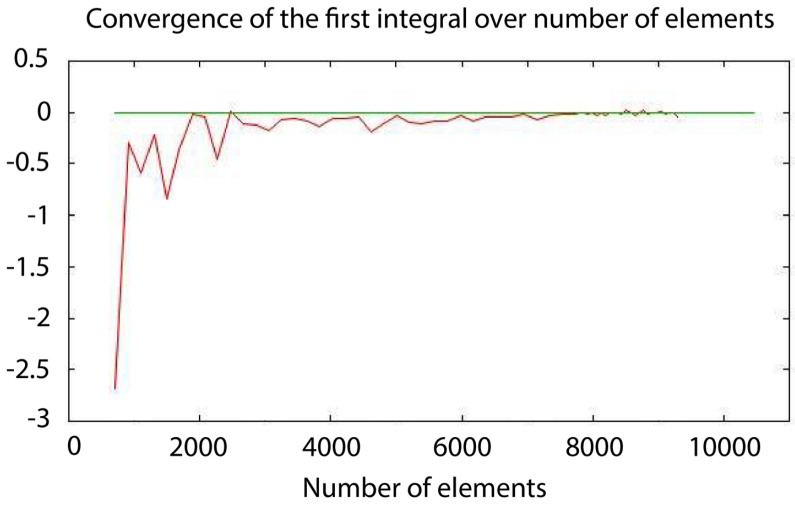


Figure 5.18: *Convergence of the first integral; Radius=4.5, length=75.*

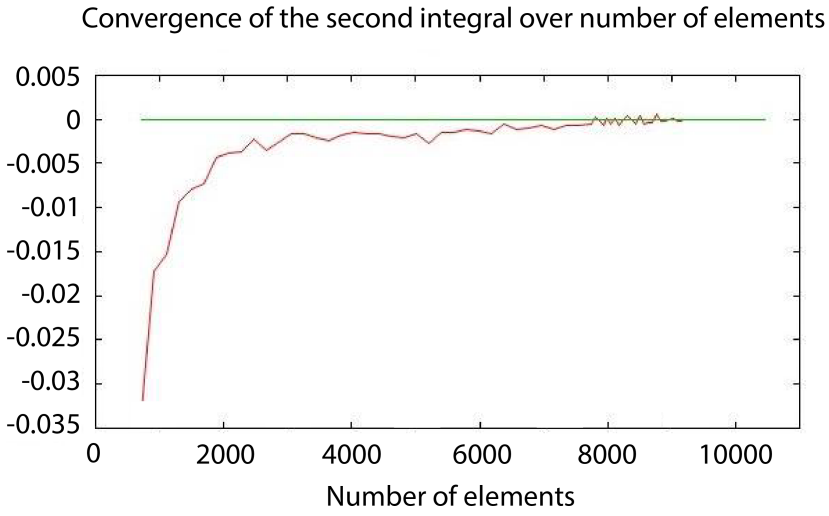


Figure 5.19: *Convergence of the second integral; Radius=4.5, length=75.*

## 5.16 New grid development

A new grid with a reduced number of points is developed for a new jet case in order to reduce computational costs. Since the acoustic pressure prediction is carried out by the FWH method the number of grid points is reduced in the blocks 4 and 5, see Figure 5.14. The number of grid points is reduced in the radial (r) direction in the block 4 and 5 and in the axial (z) direction in blocks 2 , 3, 4 and 5 respectively, see Figure 5.14. In the $r$ direction the original grid remains untouched up to $r = 12$, see Figure 5.20. From this point on a new grid is generated using polynomial functions such as $r(x) = ax^{e_1} + bx^{e_2}$ where $a$ and $b$ are coefficients determined by a joint condition between the new and old grids. The exponents $e_1$ and $e_2$ determine the stretching of the grid, and in this case they are defined as $e_1 = 10$ and $e_2 = 1$. In this simulation the acoustic field will be computed by the FWH solver, therefore there is no need to keep the slope of the grid constant in the far field. In Figure 5.21 a comparison between the old and the new grids is shown. The slope of the new grid increases from the joint point onwards in order to have a coarser grid in the far field. In a similar way the grid in the $z$ direction has been modified. The original grid remains unchanged up to $z = 60$, see Figure 5.22. From this point onwards a new grid is generated using the same polynomial function as in the $r$ direction. In the block 5 the number of grid points in the $z$ direction is reduced since also in this sector the acoustic field is computed by FWH solver, see Figure 5.23. The resulting grid contains $149 \times 10^6$ points while the old grid contained $408 \times 10^6$ points using 130 collocation points in the azimuthal direction. This reduction in the number of grid points implies obvious advantages in the computational costs.

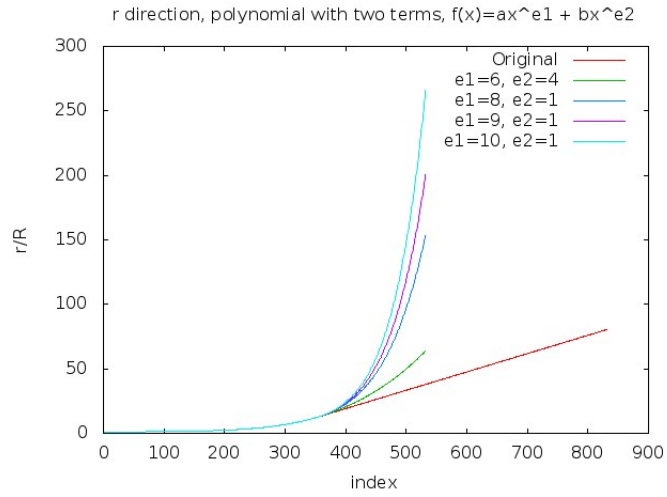


Figure 5.20: *Grid in r direction over the number of grid points.*

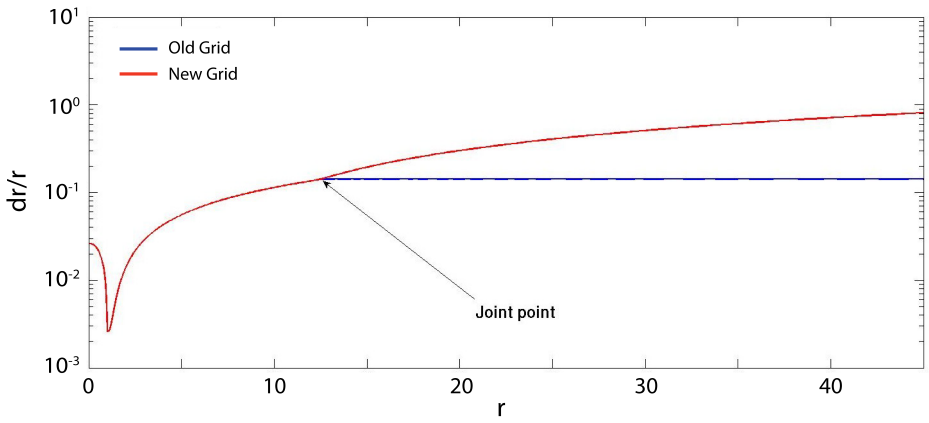


Figure 5.21: *Comparison between the new and old grid in r direction. The $dr/r$ of the old grid is constant in the acoustic field while the new grid is stretched.*

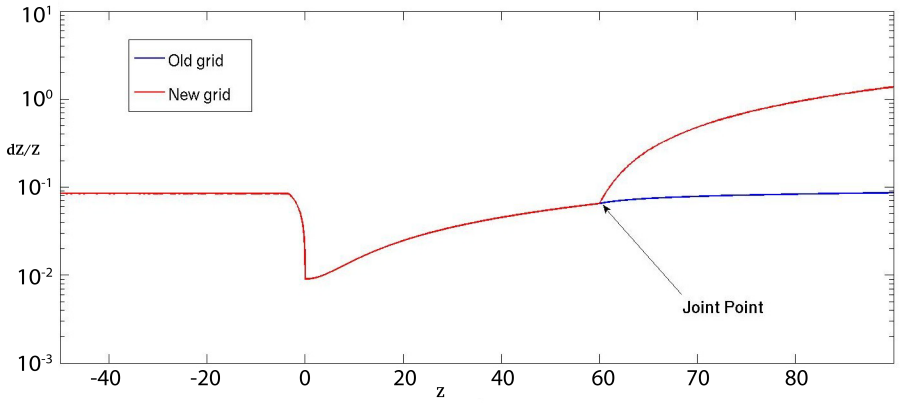


Figure 5.22: *Comparison between the new and old grid in the z direction.*

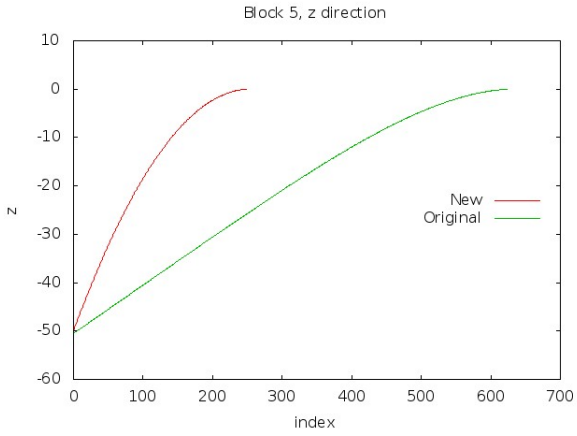


Figure 5.23: *Block 5: Comparison between the new and old grid in the z direction over the number of points.*

## 5.17 New jet simulation

In this section a new DNS simulation for a jet case is presented, with 64 azimuthal modes. Tables 5.2 and 5.3 summarize the numerical set up for this case. In Figure

5.24 the dilatation field $\nabla \cdot \bar{u}$ is shown. Reflected waves from the upper boundary are clearly visible. Apparently the characteristic boundary conditions, that are set on the boundaries, reflect the outgoing waves. In order to overcome this inconvenience a dissipative sponge [93] is set on the axial-radial plane with $\phi = 0°, 180°$ and tested in a 2D case, see Figure 5.25. Apparently the sponge dissipates the incoming waves. In order to verify that the flow field has not been altered, the flow parameters are compared with the flow parameters of the case without sponge. Two sections are selected in the flow field and the time-averaged $u$ component is displayed in Figure 5.26. It is evident that the flow field statistically is no longer the same. Therefore, the sponge is excluded as a solution to eliminate the reflected waves.

| Block | $Dz \times Dr$ | $Nz \times Nr$ |
|---|---|---|
| 1 | $50 \times 1$ | $624 \times 68$ |
| 2 | $70 \times 1$ | $2398 \times 68$ |
| 3 | $70 \times 0.0416$ | $2398 \times 16$ |
| 4 | $70 \times 30$ | $2398 \times 415$ |
| 5 | $75 \times 30$ | $250 \times 415$ |

Table 5.2: *Size, number of grid points.*

| Case | $M_j$ | $M_{co}$ |
|---|---|---|
| 1 | 0.84 | 0.2 |

Table 5.3: *Simulation parameters.*

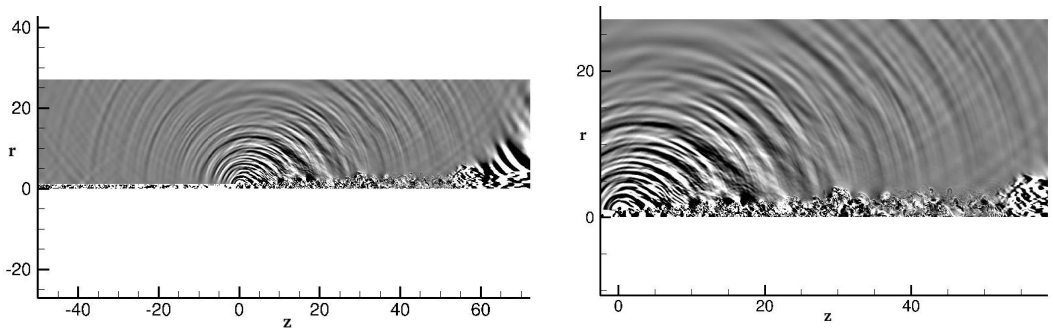


Figure 5.24: *Dilatation field: the contour plot level is [-0.001,0.001]; the reflective waves are well visible.*

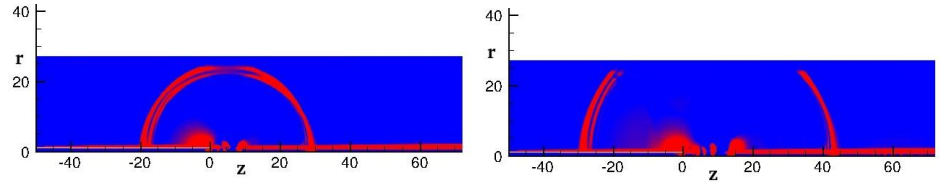


Figure 5.25: *Density field; upper picture: incoming wave, time=20; lower pictures: incoming wave partially absorbed by the sponge, time=30. The contour plot level is [0.9999,1].*

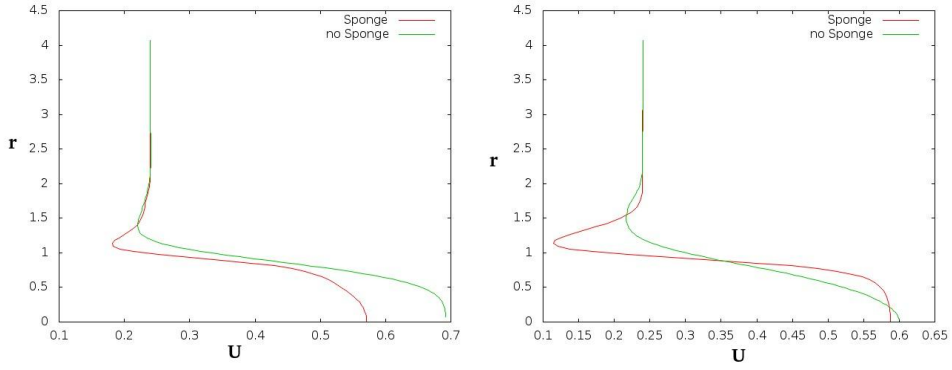


Figure 5.26: *Left picture: u components at z=20; right picture: u component at z=40.*

Since the grid is coarse away from the flow field, see Figure 5.21 a possible solution to eliminate the reflective waves is to extend the grid in the $r$ direction. In this way the waves near the upper and lower boundary would be damped "naturally". Therefore, 34 grid points are added in r direction and a new DNS simulation is computed 290400 time steps. The flow parameters are the same as in Table 5.3. The result is successful since no reflected waves appear to be present, as Figure 5.27 shows.

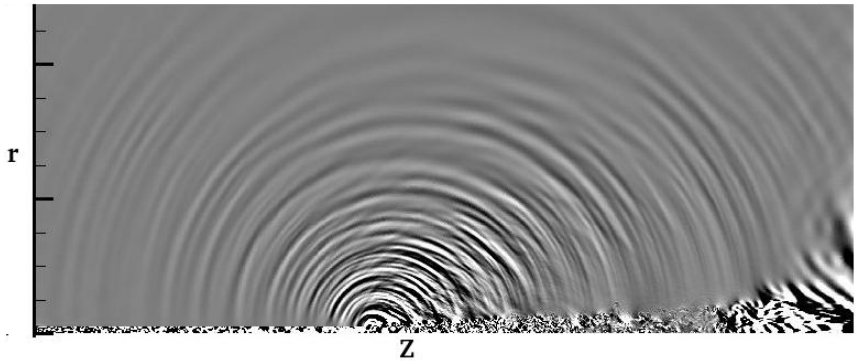


Figure 5.27: *Dilatation field; contour level [-0.001,0.001].*

### 5.17.1 New spectrum prediction using FWH solver

In this section the spectrum prediction using the FWH solver is presented. The DNS data are available from the previous simulation, see Section 5.17. In this case the time step has been reduced to $\Delta t = 0.0125$, the number of time samples is 4000. In Table 5.4 the dimensions of the FWH surfaces are displayed.

Figure 5.28 shows the spectrum prediction at $\theta = 45°$. As the radius of the control surface increases only the spectrum at the high frequencies decreases. This is a behaviour we expected increasing the grid resolution. In Figure 5.28 the spectrum prediction at $\theta = 90°$ shows a lower accuracy in the agreement between the DNS data

| FWH surface | Radius | Length |
|---|---|---|
| $S1$ | 2 | 50 |
| $S2$ | 3 | 50 |

Table 5.4: *FWH surface dimensions.*

and the FWH prediction. The reason for this disagreement is not clear. Figure 5.30 shows a good agreement of the spectrum prediction at $\theta = 140°$.

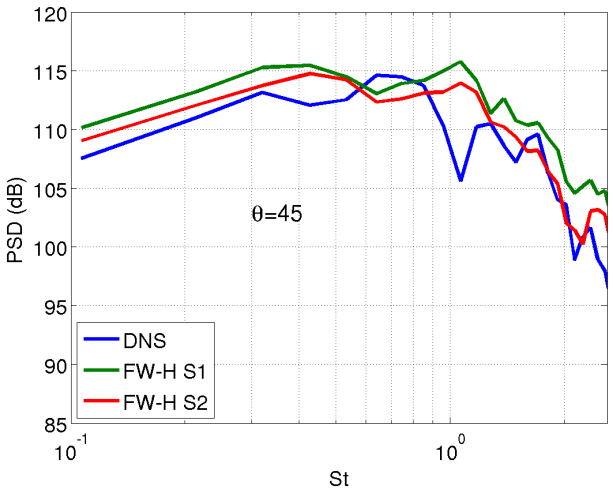


Figure 5.28: *New jet case* $M084_{c2}$. *Observer position* $r_{ob} = 60, \theta = 45°$.

The acoustic spectrum shows small sensitivity to the FWH surface position. In order to make the acoustic spectrum less sensitive to the FWH surface position the grid resolution in the $r$ direction should be improved.

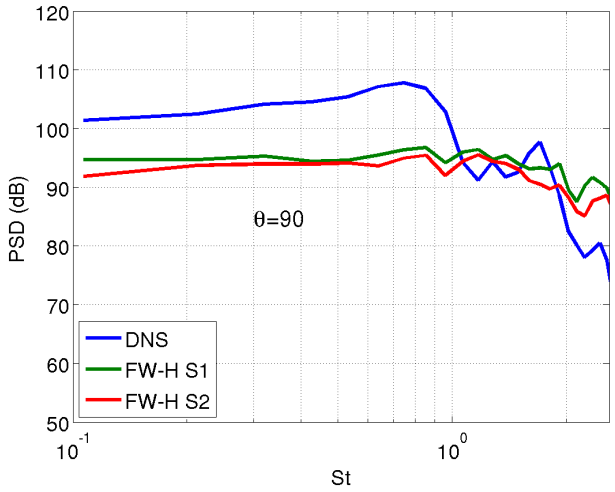


Figure 5.29: *New jet case $M084_{c2}$. Observer position $r_{ob} = 60, \theta = 90°$.*

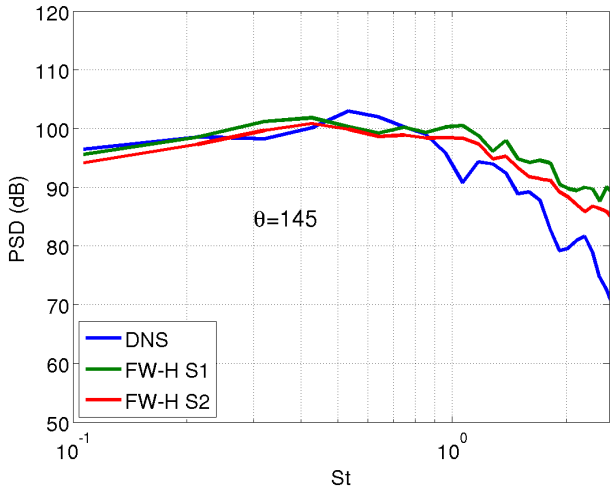


Figure 5.30: *New jet case $M084_{c2}$. Observer position $r_{ob} = 60, \theta = 145°$.*

### 5.17.2 Observation on the FWH surface

The position of the FWH surface should slightly affect the accuracy of the sound prediction in the far field, but in general the sound should not be strongly dependent on the position of the surface. In the acoustic spectrum, only the values at the high frequencies should drop as the surface is moved away from the flow field. This is due to the fact that the grid spacing increases. As for the shape of the control surface, a cylindrical surface forces the upstream part of the sleeve further from the strongest sound production, especially at high frequencies. In other words, the first part of the cylinder is in a region were the grid tends to enlarge sharply. For this reason the shape of the FWH surface is usually conical, and in this way it is possible to embed the flow field tightly. Since the grid for the jet cases has been developed in cylindrical coordinates, extracting a conical FWH surface would require a grid-point interpolation. Therefore, a conical FWH surface is not convenient in this case due to the extra computational effort required.

## 5.18 Investigation on the acoustic liner effect on the acoustic far-field

In this section the FWH method is used to calculate the PSD of acoustic signals in the far-field with and without the presence of the acoustic liner in the pipe. The FWH surfaces are obtained from DNS of compressible isothermal jet/pipe simulations. The jet/pipe simulations are characterized by a subsonic jet flow and a laminar co-flow. Table 5.5 shows the general characteristics of the current test cases. Further details

regarding the numerical set-up can be found in Sandberg & Tester [94].

| Case | Liner | $M_{jet}$ | $M_{co}$ | $Re_{jet}$ |
|---|---|---|---|---|
| $M84c2L$ | *yes* | 0.84 | 0.2 | 8.522 |
| $M84c2nL$ | *no* | 0.84 | 0.2 | 8.529 |

Table 5.5: *Simulation parameters; $M_{jet}$, $M_{co}$, based on bulk velocity in pipe at pipe exit. $Re_{jet}$ based on bulk velocity at the pipe exit and pipe diameter.*

In order to avoid mass flow fluctuations in the pipe that cause strong acoustic radiation, the inflow perturbation velocities for the axisymmetric mode $m = 0$ are set to zero, as explained in Paragraph 4.2. This inflow condition treatment has been applied to both cases $M84c2L$ and $M84c2nL$. Impedance parameters are set to obtain a resonance frequency at $St_{res} = 1$, $R = 4$, $X_1 = 1.177$ and $X_2 = -33.49$. The FWH surface is characterized by the parameters shown in Table 5.6

| Length | Radius | Grid points z direction | Grid points $\theta$ directions |
|---|---|---|---|
| 50 $R_{pipe}$ | $2R_{pipe}$ | 2050 | 130 |

Table 5.6: *FWH surface parameters.*

The record length of the FWH surface data is 4000 samples, with a sampling interval $\Delta t = 0.02$. The acoustic $PSDs$ are calculated at two monitor points in polar coordinates $\theta = 45°$, $r_{ob} = 60$ and $\theta = 90°$, $r_{ob} = 60$ with $r_{ob} = \sqrt{(z/R_{pipe})^2 + (r/R_{pipe})^2}$. In order to evaluate the contribution of individual azimuthal modes to the overall noise the FWH surface data are Fourier transformed to extract the single azimuthal modes.

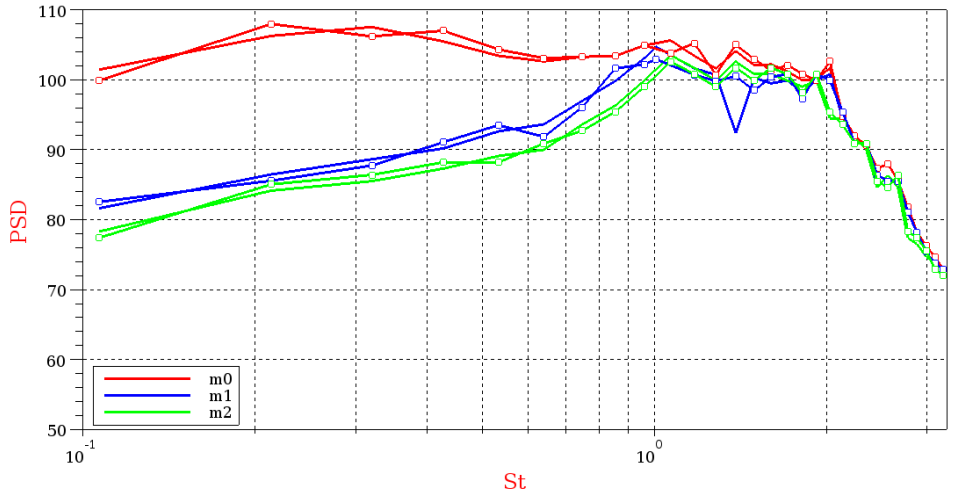


Figure 5.31: *PSD of azimithal modes m at* $\theta = 45°$, $r_{ob} = 60$. *Solid line with circle M84c2L, solid line M84c2nL.*

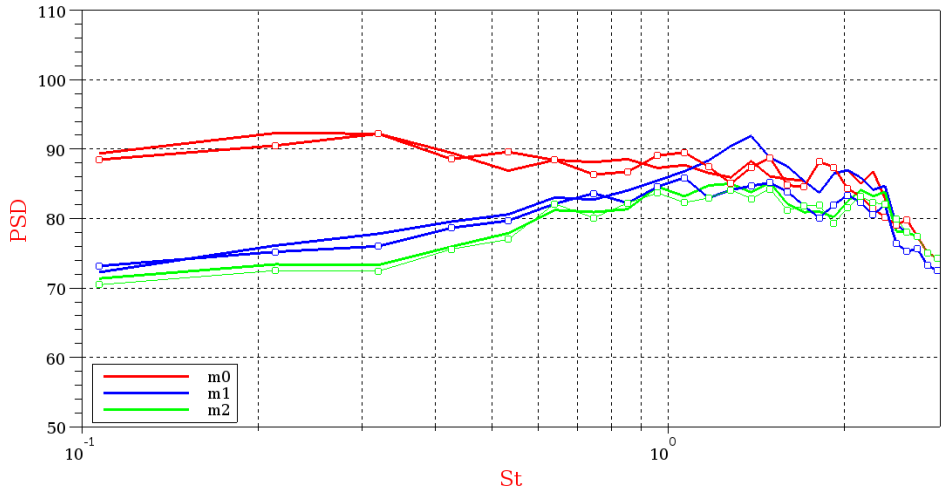


Figure 5.32: *PSD of azimithal modes m at* $\theta = 90°$, $r_D = 60$. *Solid line with circle M84c2L, solid line M84c2nL.*

Figure 5.31 shows the PSD of azimuthal modes at $\theta = 45°$, $r_D = 60$ with and without the presence of the liner. The comparison shows no relevant difference between the $M84c2nL$ and $M84c2L$ cases for every azimuthal mode. This suggests that at $\theta = 45°$ the liner has no effect on the far field and all the noise is related to the jet-mixing. Figure 5.32 shows the same comparison at $\theta = 90°$. In this case a relevant discrepancy is observed for $m = 1$ between $St = 1$ and $St = 2$. This reduction is caused by the presence of the liner which is set for $St_{res} = 1$. This implies that the internally generated noise affects the far field noise at $\theta = 90°$ and the acoustic liner is capable of attenuating it. Therefore, the noise detected in the far field is not contaminated by the internally generated noise when the liner is present.

### 5.18.1 Acoustic prediction using far field approximation

As introduced in Section 5.12, we can also compute the noise applying a far field approximation. The sound pressure level (SPL) is computed varying the position of the observer $r_{ob}$ in the direction $\theta = 40°$. The SPL is computed for two cases, one with the advanced time scheme and the other without the advanced time scheme. The percentage difference, dSPL%, between the two SPL is plotted in Figure 5.33 as a function of the observer position $r_{ob}$. In this case the observer position is made non-dimensional using the length of the FWH surface. In the previous noise predictions the observer was located at $r_{ob} = 60$ which is 1.2 times the length of the FWH surface. If we look at Figure 5.33, for $r_{ob} = 1.2$ dSPL is more than 2.8 %. In the case of jet noise mapping for the landing and take off, where $r_{ob}$ can be more than 10 times the length of the FWH surface, this field approximation can be applied since the dSPL is smaller

than 0.5 %. This would bring a great advantage in terms of computational costs.

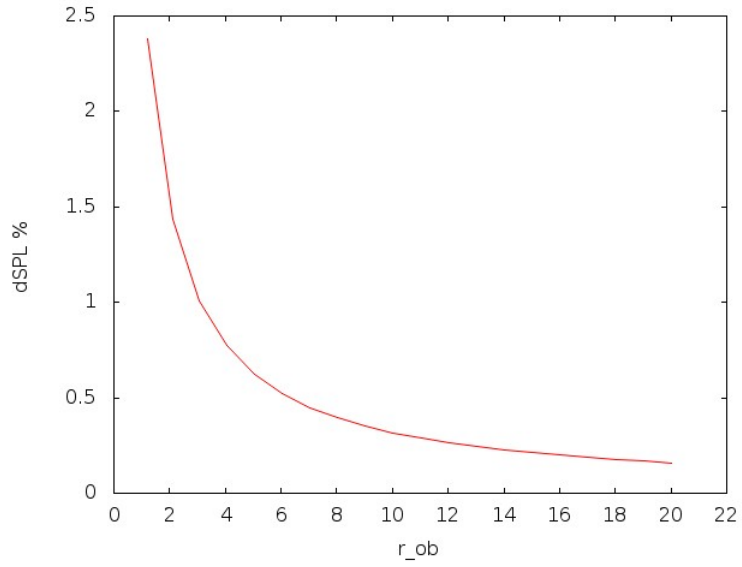


Figure 5.33: *dSPL tends to zero as the observer move away from the control surface.*

## 5.19 Conclusion

In this section a Ffowcs Williams-Hawkings formulation has been implemented and tested for noise prediction using DNS data available from the previous simulations. The noise spectrum has been computed and the results show satisfactory accuracy. Furthermore, when the far field approximation is applied the error in the noise prediction in term of sound pressure level is less than 2.8% for observer locations more than 1.2 times the FWH surface length. This approximation is particularly useful when noise prediction needs to be computed in many points in the far field, e.g. jet noise mapping.

# Chapter 6

# Conclusions and future work

In the present work DNS solutions for a pipe configuration have been computed to investigate suppression of previously identified internal noise sources with an acoustic liner, using a time domain acoustic liner model developed by Tam and Auriault. The Tam and Auriault model has been implemented in an existing DNS code. The Tam and Auriault model was originally defined for inviscid 1D models, while in the present work it has been applied to a fully viscous 3D flow. In the original formulation the pressure time derivative was replaced by the normal gradient of the normal velocity using the linearized energy equation. This has also been possible in the current case because in the viscous flow simulations a no-slip condition on the wall has been applied. Therefore, only the wall-normal component, $v$, is allowed to vary unlike the other components $u$ and $w$, which are set to zero. This encouraged us to implement the liner model using the same numerical scheme as employed in the DNS code available in our research group. The boundary layer on the acoustic liner was then solved by the DNS solver itself. It has been shown that applying the no-slip condition to the impedance model

does not results in any numerical instability. Therefore, the Tam and Auriault model provides a well-posed boundary condition for Navier-Stokes equations. Furthermore, it has been shown that a fully resolved boundary layer removes the instability previously observed by other researchers [23, 20, 15].

The model implementation has been validated for several basic pipe test cases together with verification results obtained from eigenvalue solutions of the linear wave equation. The results from the DNS code were in good agreement with the theoretical results. Furthermore, the liner model has been tested using different sets of parameters to study the attenuation capability for fully turbulent pipe flows. The liner has been shown to provide a strong attenuation in the first half of the pipe, while the attenuation saturates in the second half of the pipe. The liner attenuation has also shown great sensitivity to the reactance slope. Acoustic attenuation has been analysed for higher azimuthal modes, showing the capability of the liner to generate a broad band attenuation for azimuthal modes 1, 2, 3.

Inlet flow conditions have been modified to improve the noise attenuation. As a result the acoustic liner, combined with the new inflow condition, provided a high level of attenuation. In order to understand the effect of the liner on the acoustic and turbulent components of the unsteady wall pressure, an azimuthal/axial Fourier transform has been applied and the acoustic and turbulent wavenumber regimes clearly identified. It has been found that the spectral component occupying the turbulent wavenumber range is unaffected by the liner, whereas the acoustic wavenumber components are strongly attenuated, with individual radial modes evident as each cuts on with increasing Strouhal number. By separating the acoustic pressure component from the turbulent pressure component, it has been shown that the acoustic component prevails

over the turbulent one. This explains why the acoustic liner attenuates the acoustic energy only, leaving the turbulent component statistically unchanged. Since in the literature there is no previous attempt to study the effects of an acoustic liner model on fully turbulent flows, the present work provides a new reference for noise reduction analysis. Relevant results related to the acoustic liner model study have been published in the *Journal of Sound and Vibration* (Olivetti, Sandberg & Tester [5]).

Furthermore, the FWH method has been implemented and tested in order to compute far field noise based on jet flow simulations. A number of tests have been carried out with different FWH surfaces to achieve the best accuracy. Jet flow simulations have been computed using the above-mentioned DNS code, with and without the presence of the acoustic liner. Noise predictions based on the FWH method have shown that the acoustic liner model is capable of reducing the noise in the far field. This allows us to remove the internally generated noise and study the far field noise due to the jet-mixing without contaminations from other sources.

As for future work, the Tam and Auriault model can be used for further investigations on jet noise analysis and internally generated noise. Following the results in the present work an open question may arise in relation to the attenuation contour shown in Figure 3.23. The attenuation contour seems to shift towards higher frequencies as the azimuthal mode number increases. This has been justified considering additional noise being generated by the turbulent pipe flow. However, further investigations are required to better understand this attenuation trend.

The attenuation capabilities of the acoustic liner model could be investigated by carrying out more parametric studies. In the present work the acoustic attenuation has been investigated for two different Mach numbers and one Reynolds number, however

more turbulent pipe flows with different conditions can be analysed.

In Paragraph 3.6.4 it has been shown that the presence of the acoustic liner model does not alter the turbulent structure substantially. However, other studies [67] showed that, when the resonance frequency of the liner is tuned to the characteristic time scale of the outer layer eddies, instability and alterations of the turbulent structures near the wall are observed. Future work could investigate how the liner can affect the hydrodynamic field under specific conditions.

Another possible application for the future could involve more complex geometries. The liner model has been implemented in generalized curvilinear coordinates, therefore test cases with a more complex surface can be computed using the Tam and Auriault model. This allows the study of the acoustic attenuation in turbulent flows with more realistic configurations.

# Bibliography

[1] Takao, S., *Aviation and the Environment: Noise, Hearing before the Subcommittee on Aviation of the Committee on Transportation and Infrastructure.* Pennsylvania, U.S. Government Printing Office, 2007, pp. 149–153.

[2] Suzuki, T., *A review of diagnostic studies on jet-noise sources and generation mechanisms of subsonically convecting jets.* Fluid Dynamic Research, Vol. 42 014001.

[3] NASA report, *Making Future Commercial Aircraft Quieter.* NASA, 1999, Glenn Research Center Cleveland, FS–1999–07–003–GRC.

[4] Kempton, A., *Acoustic liners for modern aero-engines.* Rolls-Royce report, 2011, University of Southampton, UK.

[5] Olivetti, S., Sandberg, R. D. and Tester, B. J., *Direct Numerical Simulation of Turbulent Flow with an Impedance Condition.* Journal of Sound and Vibration, 2015, Volume 344, Pages 28-37.

[6] Lansing, DoL., & Zorumski, W.E., *Effects of Wall Admittance Changes on Duct*

*Transmission and Radiation of Sound.* Journal of Sound and Vibration, Vol. 27, No. 1, pp. 85-100, March 1973.

[7] Myers, M. K., *On the acoustic boundary condition in the presence of flow.* Journal of Sound and Vibration, 71(8), 429434, 1980.

[8] Ingard, U., *Influence of fluid motion past a plane boundary on sound reflection, absorption, and transmission.* Journal of the Acoustical Society of America, 31(7), 1035–1036, 1959.

[9] Hubbard, H., H., *Aeroacoustics of Flight Vehicles: Theory and Practice.* NASA Langley Research Center Hampton, Virginia, 1991.

[10] Rschevkin, S. N., *A course of Lectures on the Theory of Sound.* MacMillan Co., 1963.

[11] Koch, W. & Mohring, W., *Eigensolutions for liners in uniform mean flow ducts.* AIAA Journal 21 (2), 200213, 1983.

[12] Brazier-Smith, P. R. & Scott, J. F., *Stability of fluid flow in the presence of a compliant surface.* Wave Motion 6, 547560, 1984.

[13] Crighton, D. G. & Oswell, J. E., *Fluid loading with mean flow. Response of an elastic plate to localized excitation.* Phil. Trans. R. Soc. Lond. A 335, 557592, 1991.

[14] Peake, N., *On the behaviour of a fluid-loaded cylindrical shell with mean flow.* J. Fluid Mech. 338, 387410, 1997.

[15] Abrahams, I. D. & Wickham, G. R., *On transient oscillations of plates in moving fluids.* Wave Motion 33, 723, 2001.

[16] Lucey, A. D., Sen, P. K. & Carpenter, P. W., *Excitation and evolution of waves on an inhomogeneous flexible wall in a mean flow.* J. Fluids Struct. 18, 251267, 2003.

[17] Eversman, W. & Beckemeyer, R. J., 1972. *Transmission of sound in ducts with thin shear layers Convergence to the uniform flow case.* J. Acoust. Soc. Am. 52, 216220.

[18] Tester, B. J., *Some aspects of sound attenuation in lined ducts containing inviscid mean flows with boundary layers.* J. Sound Vib. 28, 217-245, 1973.

[19] Tam, C. K. W. & Auriault, L., *Time-Domain Impedance Boundary Conditions for Computational Aeroacoustics.* AIAA Journal, 34(5), 917–923. 1996.

[20] Rienstra, S.W. & Vilenski, G. G., *Spatial Instability of Boundary Layer Along Impedance Wall.* AIAA Paper 2008-2932. 2008.

[21] Richter, C. & Thiele, F. H., *The stability of time explicit impedance models.* AIAA paper 2007-3538.

[22] Aurgan, Y., Starobinski, R. & Pagneux, V., *Influence of grazing flow and dissipation effects on the acoustic boundary conditions at a lined wall.* J. Acoust. Soc. Am., 2001, 109, 5964.

[23] Vilenski, G. G., & Rienstra, S. W., *On hydrodynamic and acoustic modes in a ducted shear flow with wall lining.* J. Fluid Mech. 583, 4570, 2007.

[24] Brambley, E. J., *Fundamental problems with the model of uniform flow over acoustic linings.* J. Sound Vib. 322, 1026-1037, 2009.

[25] Tam, C. K. W., Ju, H., Jones, M. G., Watson, W. R. & Parrott, T. L., *A computational and experimental study of resonators in three dimensions.* 15th AIAA/CEAS Aeroacoustics Conference (30th AIAA Aeroacoustics Conference), AIAA Paper 2009-3173, Miami, Florida, May 2009.

[26] Zhang, Q. & Bodony, D. J., *Numerical simulation of two-dimensional acoustic liners with high speed grazing flow.* AIAA Journal, 49(2):365382, February 2011.

[27] Sandberg, R. D., Sandham, N. D., & Suponitsky, V., *DNS of fully turbulent jet flows in flight conditions including a canonical nozzle.* 17th CEAS/AIAA Aeroacoustics Conference, June 6-8, 2011, Portland, Oregon, AIAA Paper 2011-2918.

[28] White, F. M., *Viscous fluid flow.* McGraw-Hill International Editions, Mechanical Engineering Series, 1991.

[29] Bull, W. K., *Wall-pressure fluctuations beneath turbulent boundary layers : some reflections on forty years of research.* Journal of Sound and vibration, No.190, Vol.3, pp.299-315, 1996.

[30] Ibars, F., *Contribution des petits nombres donde au champ parietal de pression dans une couche limite turbulente bidimensionnelle. Comparaison de differentes techniques experimentales.* These de doctorat, Ecole Centrale de Lyon, No. 90-15, 1990.

[31] Manoha, T. C., *Mesure du spectre en frequences et nombres dondes du champ des fluctuations de pression parietale sous une couche limite turbulente.* These Universite Paris VI, No. 93PA06673, 1993.

[32] Abraham, M. & Keith, W. L., *Direct measurements of turbulent boundary layer wall pressure wavenumber frequency spectra.* Journal of Fluid Engineering, Vol.120, pp.29-39, 1998.

[33] Maidanik, G., *Flush-mounted pressure transducer systems as spatial and spectral filters.* Journal of the Acoustical Society of America, Vol.42, No.5, pp.1017-1024, 1967.

[34] Maidanik, G. & Jorgensen, D.W., *Boundary wave-vector filters for the study of the pressure field in a turbulent boundary layer.* Journal of the Acoustical Society of America, Vol.42, No.2, pp.494-501, 1964.

[35] Bally, P. Olivero, P. Hocquet, P. & Forestier, B.E., *Spectre nombre donde-frequence des fluctuations de pression sous couche limite turbulente en gradient de pression nul et positif.* Journal d'Acoustique, Vol.3, pp.125-136, 1990.

[36] Blake, K. & Chase, D. M., *Wavenumber-frequency spectra of turbulent boundary-layer pressure measured by microphone arrays.* Journal of the Acoustical Society of America, Vol.49, No.3, Part 2, pp. 862-877, 1971.

[37] Corcos, M., *Resolution of pressure in turbulence.* Journal of the Acoustical Society of America, Vol.35, No.2, pp.192-199, 1963.

[38] Zheng, S. & Zhuang, M., *Verification and Validation of Time-Domain Impedance Boundary Condition in Lined Ducts.* AIAA Journal, 43, 306–313, 2005.

[39] Gaeta, R., Mendoza, J. & Jones, M., *Implementation of In-Situ Impedance Techniques on a Full Scale Aero-Engine System.* AIAA Paper 2007–3319, 2007.

[40] Parrot, L., Watson, R. & Jones, G., *Experimental Validation of a Two-Dimensional Shear-Flow Model for Determining Acoustic Impedance.* NASA Technical Paper 2979, 1987.

[41] Reymen, Y., Baelmans, M. & Desmet, W., *Time-Domain Impedance Formulation suited for Broadband Simulations.* AIAA Paper 2007–3519, 2007.

[42] Burak, M. O., Billson, M., Eriksson, L. E. & Baralon, S., *Validation of a Time and Frequency Domain Grazing Flow Acoustic Liner Model.* AIAA Journal, 47(8), 1841–1848, 2008.

[43] Ju, H. & Fung, K.Y., *Time-domain impedance boundary conditions with mean flow effects.* AIAA Journal, 39(9), 1683–1690, 2001.

[44] Özyörük, Y., Long, L. N., & Jones, M. G., *Time-domain numerical simulation of a flow-impedance tube.* Journal of Computational Physics, 146(1), 29–57, 1998.

[45] Tester, B. J., *The propagation and attenuation of sound in lined ducts containing uniform or plug flow.* Journal of Sound and Vibration, 28(2), 151–203. 1973.

[46] De Metz, F. C. & Farabee, T. M., *Laminar and Turbulent Shear Flow Induced Cavity Resonances.* AIAA Paper 1977–1293, 1977.

[47] Aurégan, Y. & Leroux, M.,, *Experimental evidence of an instability over an impedance wall in a duct with flow.* J. Sound Vib. 317, 432–439, 2008.

[48] Hesthaven, J., Gottlieb, S., & Gottlieb, D., *Spectral Methods for Time-Dependent Problems.* Cambridge Monographs on Applied and Computational Mathematics, 2007.

[49] Matteo F. & Johnson, S., *The Design and Implementation of FFTW3.* Proceedings of the IEEE, Vol. 93, Issue 2, pages 216-231, 2005.

[50] Butcher, J. C., *A stability property of implicit Runge-Kutta methods*, BIT 15: 358–361. 1975.

[51] Canuto, C., Hussaini, M.Y., Quarteroni, A. & Zang T.A., *Spectral Methods in Fluid Dynamics.* Springer-Verlag, 1988.

[52] Carpenter, M. H., Nordstrom, J. & Gottlieb, D. A., *Stable and Conservative Interface Treatment of Arbitrary Spatial Accuracy.* J. Comp. Phys., Vol. 148, No 2, 1999, pp. 341-365.

[53] Visbal M., Gaitonde D., *Very high-order spatially implicit schemes for computational acoustics on curvilinear meshes.* J. Comput. Acoust., 2001, 9(4):1259–86.

[54] Sandberg, R. D., *An axial treatment for flow equations in cylindrical coordinates based on parity conditions.* Computer and fluids, Vol. 49, 2011, pp. 166-172.

[55] Kennedy, C., Carpernter, M. & Lewis, R.., *Low-storage, explicit Runge-Kutta scheme for compressible Navier-Stokes equations.* J. Comp. Phys. Applied Numerical Mathematics, Vol. 35, 2000, pp. 1676-1700.

[56] Sandberg, R. D. & Sandham, N. D., *Non-reacting zonal characteristic boundary condition for direct numerical simulation of aerodynamic sound.* AIAA Journal, Vol. 44, No. 2, February 2006, pp. 402-405.

[57] Bauer, A. B. & Chapkis, R. L., *Noise Generated by Boundary-Layer Interaction with Perforated Acoustic Liners.* Journal of Aircraft, 14(2), 157–160. 1977.

[58] Kennedy, C. & Gruber, A., *Reduced aliasing formulation of the convective terms within the Navire-Stokes equation for compressible fluid.* J. Comp. Phys., Vol 227, 2008, pp. 1447-1700.

[59] Bogey, C., de Cacqueray, N. & Bailly, C., *Shock-capturing methodology based on adaptive spatial filtering for high-order non-liner computations.* J. Comp. Phys., Vol. 228, No. 5, 2009, pp. 1447-1465.

[60] Touber, E. & Sandham, N. D., *Large-eddy simulation of low-frequency unsteadiness in a turbulent shock-induced separation bubble.* Theor. Comp. Fluid Dyn., Vol. 23, No. 2, 2009, pp. 79-107.

[61] Salikuddin, M., Sr. Engineer, GE Aircraft Engines. *Optimization of Acoustic Liner Design for Axiymmetric Mixer-Ejector Nozzles Under ESPR PROGRAM.* ICAS 2002 CONGRESS.

[62] Sandberg, R., Tester, B. *Application of a Phased Array Technique to DNS-Generated Turbulent Subsonic Jet Data.* AIAA-2012-2118.

[63] Ozyoruk, Y., *Sound Radiation From Ducted Fans Using Computational Aeroacoustics On Parallel Computers.* Ph.D thesis, The Pennsylvania State University, December 1995.

[64] Motsinger, R. E., & Kraft, R. E., *Design and performance of Duct Acoustic Treatment, Aeroacoustic of Flight Vehicles: Theory and Practice.* NASA RP-1258, Aug. 1991, Chap. 14.

[65] Zorumski, W.E., *Acoustic Theory of Axisymmetric Multisectioned Ducts.*, NASA TR R-419, 1974.

[66] Wu, X., & Moin, P., *A direct simulation study on the mean velocity characteristics in turbulent pipe flow.* J. Fluid Mech. 608, 81-112, 2008.

[67] Scalo, C., Bodart, J., Lele, S. K. & Joly, L., *Compressible turbulent channel flow with impedance boundary conditions.* Phys. Fluids 27 (035107), 2015.

[68] Sandberg, R., Tester, B., *Internal report.* University of Southampton, UK, 2014.

[69] Lyrintzism, A. S., *Surface integral methods in computational aeroacoustics. From the (CFD) near-field to the (Acoustic ) far-field.* Int. J. Aeroacoistics 2, 95-128, 2003.

[70] Lighthill M.J., *On sound generated aerodynamically I.* Proceedings of the Royal Society of London. Series A, Mathematical and Physical Science, Vol. 211, No 1107, 1952, pp. 564-587.

[71] Lighthill M.J., *On sound generated aerodynamically II.* Proceedings of the Royal Society of London. Series A, Mathematical and Physical Science, Vol. 222, No 1148, 1952, pp. 1-32.

[72] Crighton,D.G., Dowling, A.P., Ffowcs Williams, J.E., Heckl, M. & Leppington, F.G. *Modern Methods in Analytical Acoustic.* Springer-Verlag, 1992.

[73] Howe, M.S., *Theory of Vortex Sound.* Cambridge University Press, 2003.

[74] Lyrintzis, A. S., *The Use of Kirchhoff's Method in Jet Aeroacoustics.* Final Report NASA/NAG 1-1605, 1994.

[75] Freund, J. B., Sanjiva, K. L., Parviz M., *Calculation of the Radiated Sound Field Using An Open Kirchhoff Surface*. AIAA Journal, Vol. 34, No. 5, 1996, pp. 909-916.

[76] Tam, C. K. W., *Computational Aeroacoustics: An Overview*. Paper presented at the RTO AVT Symposium on "Ageing Mechanisms and Control: Part A-Developments in Computational Aero- and Hydro-Acoustics", held in Manchester, UK, 8-11 October, and published in RTO-MP-079(1).

[77] Shur, L., Spalart, R., Strelets, K., *Noise prediction for increasingly complex jets. Part 1: Methods and tests*. Aeroacoustics Vol. 4 No 4, pages 213-246.

[78] Dowling, A. P., & Ffowcs Williams, J. E., *Sound and Source of Sound*. Ellis Horwood Limited, 1989.

[79] Cristopher Tam, K. W., *Computational Aeroacoustics: Issue and Methods*. AIAA Journal Vol. 33, No 10, October 1995.

[80] Goldstein, M. E., *Aeroacoustics*. McGraw-Hill 1976.

[81] Colonius, T., Lele, S. K. & Moin, P., *Boundary Conditions for Direct Computation of Aerodynamic Sound Generation*. AIAA Journal Vol.31, Number 9, September 1993, Pages 1574-1582.

[82] Luo, K. & Lai, H., *A Hybrid LES-Acoustic Analogy Method for Computational Aeroacoustics.* Springer 2005.

[83] Casalino, D., *An advantage time approach for acoustic analogy predictions*. Journal of Sound and Vibration 216 (2003) 583-612.

[84] Brentner, K. S., Farassat, F., *Modelling aerodynamically generated sound of helicopter rotors.* Progress in Aerospace Science 39 (2003) 83-120.

[85] Di Francescantonio, P., *A new boundary integral formulation for the prediction of sound radiation.* Journal of Sound and Vibration, 202(4), 1997, 491–509.

[86] Gel'Fand, I. M., Shilov, G. E., *Generalized Function volume I Properties and Operations.* Academy of Science U.S.S.R..

[87] Farassat, F., Myers, M. K., *Extension of Kirchhoff's Formula to Radiation From Moving Surface.* Journal of sound and Vibration, 1988, 123(3), 451-460.

[88] Spalart, P. R., Shur, M. L. & Strelets, M. Kh., *Identification of Sound Source in Large-Eddy Simulation of Jets.* 13th AIAA/CEAS Aeroacoustic Conference (28th AIAA Aeroacoustic Conference), AIAA 2007-3616.

[89] Lyrintzins, A. S., *Surface integral methods in computational aeroacoustics.* International Journal of Aeroacoustics Vol. 2, number 22, 2003.

[90] Brentner, K. S., *Numerical Algorithms for Acoustic Integrals-the Devil is in the Details.* 2nd AIAA/CEAS Aeroacoustics Conference May 6-8, 1996/State Collage, PA.

[91] Brentner, K. S., *Numerical Algorithms for Acoustic Integral with Example for rotor Noise.* AIAA Journal Vol. 35, No 4, April 1997.

[92] Shur, M. L., Spalart P. R., *Towards the prediction of noise from jet engines.* International Journal of heat and fluid flow 24 (2003) 551-561.

[93] Freund, J. B., *Proposed Inflow/Outflow Boundary Condition for Direct Computation of Aerodynamic Sound.* AIAA J., 35(4), 740-742, 1997.

[94] Sandberg, R. D., & Tester, B. J., *DNS of a turbulent jet issuing from an acoustically lined pipe*. Conference paper submitted for IUTAM, 2015.